

A Microgravity Sounding-Rocket Experiment on Protoplanetary Dust Aggregation

Von der Fakultät für Elektrotechnik, Informationstechnik, Physik
der Technischen Universität Carolo-Wilhelmina
zu Braunschweig
zur Erlangung des Grades eines
Doktors der Naturwissenschaften
(Dr.rer.nat.)
genehmigte
Dissertation

von Julie Brisset
aus Rueil-Malmaison

1. Referentin oder Referent: Prof. Dr. Jürgen Blum
 2. Referentin oder Referent: Prof. Dr. Joshua Colwell
- eingereicht am: March 12, 2014
- mündliche Prüfung (Disputation) am: May 5, 2014
2014

Contents

Summary	7
1 Introduction	9
1.1 The planetesimal theory	9
1.2 Dust growth in protoplanetary disks	10
1.2.1 Sources of dust particle motion	11
1.2.2 Dust particle collision behavior	13
1.3 Dust growth challenges	13
1.4 The SPACE experiment	15
1.5 This work	16
2 Experiment Description	17
2.1 Experiment design requirements	17
2.1.1 Experiment objectives	17
2.1.2 Carrier requirements	17
2.2 Experiment set-up	21
2.2.1 The mechanical design	22
2.2.2 The vacuum system	28
2.2.3 The data acquisition and storage systems	28
2.2.4 Electronics	32
2.2.5 The software and experiment sequence	34
2.2.6 Fullfilling requirements	35
3 Experiment runs	37
3.1 Experiments at the drop tower Bremen	37
3.1.1 Drop tower experiment set-up	38
3.1.2 Drop tower shaking profile	38
3.1.3 Experiment performance	39
3.1.4 Scientific data	39
3.2 Experiment run on the REXUS 12 rocket	40
3.2.1 Rocket flight data	40
3.2.2 Flight shaking profile	40
3.2.3 Experiment flight performance	45
3.2.4 Recovery	47
3.2.5 Scientific data	48

4	Dust samples	49
4.1	Choice of the dust analog material	49
4.2	Aggregate sizes	51
4.3	Volume filling factor and inner structure of the aggregates	53
4.4	Allocation of the dust aggregates to the different experiments	53
4.4.1	Drop tower experiments	53
4.4.2	Suborbital rocket flight experiment run	55
5	Data analysis	57
5.1	Drop tower scientific data	57
5.1.1	Aggregate and cluster collisions	57
5.1.2	Determination of the cluster fractal dimensions	58
5.2	Dust growth during the suborbital flight	58
5.2.1	Growing dust aggregates?	58
5.2.2	Growing on the wall?	63
5.3	Suborbital flight data analysis	65
5.3.1	Frame averaging	65
5.3.2	Statistical analysis methods	65
5.4	Suborbital flight frame correction	67
5.4.1	Cell rotational movement	67
5.4.2	Background illumination	69
5.4.3	Glass cleanliness	69
5.5	Determination of the statistical relative velocities	70
5.5.1	Wall velocity	70
5.5.2	Calculating the aggregate relative velocities	71
5.6	Other influences on the aggregate motion	73
5.6.1	Residual accelerations during the suborbital flight	73
5.6.2	Magnetic and electrostatic effects on the aggregate trajectories	74
6	Experimental results	77
6.1	Drop tower dust collisions	77
6.1.1	Aggregate and cluster collisions	77
6.1.2	Cluster restructuring and fragmentation	79
6.1.3	Cluster fractal dimensions	81
6.2	Suborbital flight dust collisions	83
6.2.1	Number density of free-flying aggregates	84
6.2.2	Growth of clusters on the cell walls	84
6.2.3	Sticking probability	86
6.2.4	Aggregate pull-off forces	90
7	Sub-millimeter sized dust aggregates: collision behavior and cluster properties	93
7.1	Inputs to the dust collision model	93
7.1.1	The sticking to bouncing transition	94
7.1.2	The bouncing to fragmentation transition	97
7.2	Properties of clusters composed of sub-mm-sized aggregates	98

7.2.1	Cluster fractal dimensions	99
7.2.2	Tensile strength of aggregates at the surface of clusters	99
7.2.3	Estimation of the surface energy of sub-mm-sized aggregates	101
7.2.4	Collision recipe for clusters composed of sub-mm-sized aggregates	103
7.3	Application to protoplanetary disks	106
7.3.1	The disk models	106
7.3.2	Aggregate sticking and growth	107
7.3.3	Cluster restructuring and fragmentation	111
8	Conclusion	115
A	SPACE components list	117
B	SPACE electronics board	121
C	SPACE hardware test protocols	123
C.1	Vacuum tests	123
C.2	Thermal tests	127
C.3	Camera settings and optics tests	136
C.4	Electronics test	140
C.5	Software tests	141
C.6	Mechanical tests	143
C.7	REXUS interface tests	148
	Bibliography	153
	Publications	159
	Acknowledgements	161
	Curriculum Vitae	163

Summary

In the very first steps of the formation of a new planetary system, dust agglomerates and grows inside the protoplanetary disk that rotates around the newly formed star. In this disk, collisions between the dust particles, induced by interactions with the surrounding gas, lead to sticking. Aggregates start growing until their sizes and relative velocities are high enough for collisions to result in bouncing or fragmentation.

As part of a series of microgravity experiments aiming at the investigation of the transitions between sticking, bouncing and fragmentation of colliding dust aggregates, the Sub-orbital Particle and Aggregation Experiment (SPACE) was designed, built and operated both at the drop tower in Bremen (August 2011) and on the REXUS 12 suborbital rocket (March 2012). The SPACE experiment allowed for the observation of collisions between aggregates of sizes of a few $100\ \mu\text{m}$ that were composed of SiO_2 , a commonly used protoplanetary dust analog material. The microgravity conditions provided by the drop tower and the suborbital flight allowed for collision velocities below $1\ \text{cm s}^{-1}$. At these low velocities, clusters composed of a high number of aggregates (more than 10^4) formed and grew to sizes of up to 5 mm. The analysis of these collisions, by direct tracking in the case of the drop tower data, or statistically for the suborbital flight data, delivered valuable input to a current dust collision model, which maps the outcome of collisions depending on the aggregate sizes and their relative velocities. The data results showed that the sticking probability of a collision is enhanced for aggregate-cluster and cluster-cluster collisions compared to simple aggregate-aggregate collisions. Furthermore, the sticking probability of sub-mm-sized dust aggregates could directly be measured during the suborbital rocket flight, over a velocity range covering the transition between the sticking and bouncing regimes. It was also shown that the formed clusters are more fragile and fragment at collision velocities as low as $5\ \text{cm s}^{-1}$.

In addition, the evolution of clusters formed from sub-mm-sized aggregates during the different experiments could be observed and some of their intrinsic properties derived. The measured characteristics were the cluster fractal dimensions, the tensile strength of their outer aggregate layer and the effective surface energy of their constituents. Threshold energies for cluster restructuring and fragmentation could also be determined. All these cluster properties are important input parameters for molecular dynamics or numerical simulations investigating the behavior of macroscopic clusters ($>1\ \text{mm}$ in size) in protoplanetary disks.

1 Introduction

The latest progress in observational techniques opens promising prospects on a better understanding of planet formation. The Kepler space telescope is continuously discovering new planets orbiting other stars, with sizes now ranging from Jupiter down to Earth dimensions (Howard et al. 2012), indicating that the processes leading to the formation of planets are actually very common in our universe. Furthermore, the revolutionary resolution in sub- and mm-wavelengths obtained with the ALMA telescope (Atacama Large Millimeter Array in Chile) now allows for a direct observation of the presence and spatial distribution of mm- to cm-sized dust grains down to a few astronomical units of the central star in accretion or debris disks around young stellar objects such as T-Tauri or Herbig Ae/Be stars (e.g. MacGregor et al. 2013). As these disks are believed to be the location of planet formation, the now possible observations will bring brand new insights into the processes leading to planetary systems similar to our own. The first published observations (Boley et al. 2012, van der Marel et al. 2013, for example) already demonstrate how powerful this new observational tool is, and how it will help validating current theories on planet formation and protoplanetary disk (PPD) models.

Of course, due to the very long timescales of astronomical processes (disks evolving on a timescale of $\sim 10^6$ years, Hernández et al. 2007, Yasui et al. 2012), observations alone are not sufficient to get a complete picture of the processes leading to planet formation. The combination of observations with theoretical models, numerical simulations and experimental studies is essential for an overall understanding. The experimental work presented here is intended to contribute to the current research on processes taking place in the early stages of planet formation, when dust particles inside the protoplanetary disk grow by mutual collisions. In the following, it is shown how the dust collision experiments performed in this work can help to better understand dust behavior in protoplanetary disks during the first steps of planet formation.

1.1 The planetesimal theory

As mentioned above, the presence of terrestrial planets around other stars seems to be very common. Surveys in the solar neighborhood (Howard et al. 2010b, Wittenmyer et al. 2010) concur with data gathered from space telescopes like Kepler (Howard et al. 2012) in

finding that between 15 and 20 % of the observed main sequence stars host at least one planet. Another exoplanet observation technique, gravitational microlensing, reveals that up to 62 % of the observed stars host super-Earth-like planets ($5-10M_{\oplus}$) (Cassan et al. 2012). These observations reveal the ubiquity of the processes leading to the formation of rocky bodies around newly formed stars.

Indications on how such efficient processes could take place can be inferred from the composition of primitive meteorites (Armitage 2010). These meteorites are called "primitive" as they have undergone only minor alterations since their formation, neither thermally nor chemically, which makes them suitable to gather clues about the environment they were formed in. The majority of primitive meteorites are composed of cm-sized inclusions (chondrules) surrounded by a matrix composed of micrometer-sized grains. The chondrules themselves appear to be former dust aggregates that went through one, or several flash heating events (Hewins 1997, Morris & Desch 2010). This composition indicates that meteorites were formed in an environment where dust particles of μm - to cm-sizes were abundant. As radiometric dating of the meteoritic components places them into the early stages of the Solar System, the so-called Solar Nebula (Amelin et al. 2002), it is likely that the rocky bodies present in the Solar System today found their origin in a dusty environment (Armitage 2010).

In addition, astronomical observations of young stellar objects such as T-Tauri or Herbig Ae/Be stars reveal the presence of disks composed of gas and dust around them, that could be matching environments for the formation of planets from dust (D'Alessio et al. 2001, van Boekel et al. 2003, Testi et al. 2014).

Both of these observations on how and where terrestrial planets could form, lead to the *planetesimal* theory for the formation of planets in protoplanetary disks (e.g. Chambers 2004). In this theory, dust in protoplanetary disks around young stars agglomerates into "planetesimals". These planetesimals are bodies of about 1 km in size, just massive enough for their self-gravity to become stronger than their inner cohesion forces. Some of these planetesimals then undergo runaway growth by gravitational focusing, becoming so-called protoplanets of about Mercury to Mars sizes (Wetherill & Stewart 1989). In a final stage, these protoplanets collide amongst each other due to their mutual orbital perturbances, leading to a stable planetary system as witnessed in our own Solar System (Chambers & Wetherill 1998).

The work presented here deals with the first stage in this process: the agglomeration of dust in protoplanetary disks.

1.2 Dust growth in protoplanetary disks

The very first stage of the planetesimal theory described above is the growth of dust aggregates inside of the protoplanetary disk, by mutual collisions. The smallest grains observed in protoplanetary disks have about μm sizes (e.g. van Boekel et al. 2005). To achieve growth to bigger sizes, two things are required. First the dust particles need to collide amongst each other, i.e. they need to have non-zero relative velocities. Secondly, collisions have to lead to aggregate growth instead of erosion, destruction or simple bouncing.

1.2.1 Sources of dust particle motion

Collisions between particles are caused by several thermal and aerodynamical processes acting on the dust particles embedded in the gas of a protoplanetary disk and inducing relative velocities between them.

Particles surrounded by gas are subjected to Brownian motion (Einstein 1905). For particles with μm sizes or smaller, this Brownian motion induces relative velocities on the order of 10^{-3} m s^{-1} (at 300 K). At these velocities, collisions are in the so-called "hit and stick" regime, i.e. particles always stick upon collision, building fractal aggregates. This thermal growth has been directly observed for example by Blum et al. (2002) for silicate particles (covered by a silicate-organic mantle) of $0.95 \mu\text{m}$ radius. If m is the mass of the dust particles colliding, the relative velocities induced by Brownian motion are proportional to $m^{-\frac{1}{2}}$. Thus, with increasing size, the influence of Brownian motion lessens and becomes negligible compared to the relative velocities induced by aerodynamical processes.

Interactions of the particles and the surrounding gas lead to several drift motions: azimuthal, radial and vertical drift. The main gas-induced effect causing these drift motions is aerodynamical drag. Dust particles orbiting the central star are under the influence of its gravitational field and will therefore tend to have Keplerian orbits. The gas in the disk, however, is supported by its own pressure, which partly compensated the star's gravity, and rotates at sub-Keplerian velocities. In addition, the gas rotates as a torus, i.e. with the same rotation speed on and above the midplane. Therefore, dust particles in the disk rotate faster than the gas, and particles that are not on the midplane oscillate vertically. The induced velocity difference between the dust particles and the gas leads to drag forces on the particles and to their azimuthal, radial and vertical drift. In addition, the deceleration caused by the gas drag depends on the particle size, or more precisely on their cross section to mass ratio. Accordingly, particles of different sizes drift with different velocities and have a relative velocity to one another. This leads to collisions between particles.

Another aerodynamical process leading to relative velocities between particles is turbulence. Gas turbulence was introduced into protoplanetary disk models as a source of viscosity to explain the lifetimes of the disks observed. Laminar disks would accrete onto the central star with a time scale of about 10^{13} years, which is in contradiction with observed disk ages of no more than $\sim 10^6$ years (Armitage 2010). A commonly assumed source of this turbulence could be magnetorotational instability (MRI) of the differentially rotating disk gas (Balbus & Hawley 1991). Just like for drift motions, in gas turbulence the coupling of the dust particles to the gas vortices depends on their mass to cross section ratio. This is why differently sized particles acquire different velocities in the turbulence and relative velocities lead to particle collisions.

Figure 1.1 shows the velocities induced on PPD dust aggregates by the surrounding gas and the resulting relative velocities generated between aggregates. For radii larger than 0.1 mm, gas drag starts to induce relative velocities between differently-sized particles and can reach up to 100 m s^{-1} between μm - and m-sized particles. The influence of gas turbulence on the relative velocities becomes apparent for bodies larger than 1 m in radius, with up to a few 10 m s^{-1} between cm-sized or smaller particles and 100 m-sized bodies.

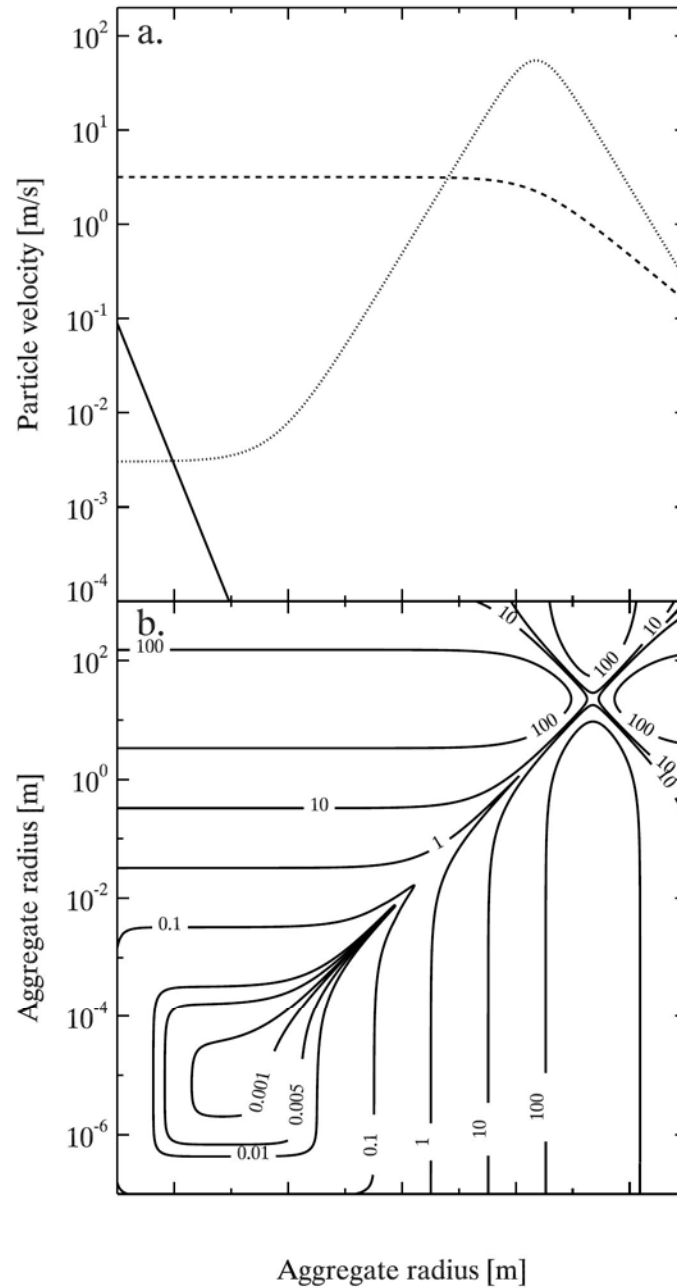


Figure 1.1: Velocities induced by the surrounding gas on dust aggregates in a protoplanetary disk: a. velocities induced by Brownian motion (solid line), radial drift (dotted line) and gas turbulence (dashed line), depending on the aggregate size. Here, only radial drift velocities are depicted. b. relative velocities of dust aggregates induced by all three processes combined (Brownian motion, radial drift and turbulence) depending on the aggregate sizes. The relative velocities are indicated in m s^{-1} . The PPD model used is the Minimum Mass Solar Nebula (MMSN) introduced by Weidenschilling (1977b). These plots were generated using equations by Einstein (1905) (Brownian motion), Weidenschilling (1977a) (radial drift) and Ormel & Cuzzi (2007) (turbulences). A distance to the central star of 1 AU and a low-turbulence environment are assumed.

1.2.2 Dust particle collision behavior

Upon collision, two particles can stick together due to short range dipole-dipole interactions between molecules, known as the Van-der-Waals force. This attractive force can be modelled as a specific surface energy at the contact area between the particles holding them together (Johnson et al. 1971, Derjaguin et al. 1975). This attractive force has to be overcome in order to separate two particles sticking together and the outcome of a collision depends on the collision energy. This is why slow velocity collisions between small particles (e.g. the μm particles subjected to Brownian motion in the PPD) always lead to sticking. Bigger and more complex aggregates (composed of a very high number of monomer particles), however, are influenced by interactions with the surrounding gas (see Section 1.2.1) and gain higher relative velocities, leading them to leave the "hit and stick" regime. Therefore, direct agglomeration of μm -sized dust particles into km-sized planetesimals via simple growth by sticking appears challenging.

1.3 Dust growth challenges

In addition to experiments on μm -sized particles (e.g. Poppe et al. 2000a,b, Blum et al. 2002), several dust collision experiments were performed observing aggregates of bigger masses and at higher relative velocities (see a review by Blum & Wurm 2008, and references therein). 19 of these experiments were combined with the Hertz contact theory (Hertz 1896) by Güttler et al. (2010) resulting in a dust collision model. This model predicts the outcome of a collision between two dust particles depending on their mass and relative velocity: for certain aggregate masses, increasing relative velocities lead to a transition in collision outcomes from sticking to bouncing and even fragmentation for higher velocities. Figure 1.2 sketches this model in its current version (Kothe et al. 2013). The transition between sticking and bouncing follows a power law relation with $v \propto m^{-1.35}$, v being the collision velocity and m the mass of the smaller colliding aggregate. At particle masses of about 10^{-5} g (corresponding to about a mm in radius for silicate particles), the transition takes place for relative velocities of a few cm s^{-1} . The observed collisions around this transition show an evolution of the sticking probability from 0 to 1 illustrated by the dashed lines (Weidling et al. 2012, Kothe et al. 2013). For relative velocities higher than $\sim 1 \text{ m s}^{-1}$, fragmentation was observed (Blum & Münch 1993). The transition from sticking to bouncing and to fragmentation with increasing particle mass and collision velocity is also observed in molecular dynamics simulations (see e.g. Dominik & Tielens 1997, Wada et al. 2009).

The impact of this transition becomes apparent when it is taken into account in PPD dust growth models and numerical simulations. In Monte Carlo dust collision simulations of Zsom et al. (2010) for example, the introduction of aggregate bouncing stalls their growth at sizes around 1 cm in diameter ("bouncing barrier"). In Brauer et al. (2008a), it is aggregate fragmentation that stalls the growth and keeps the dust size distribution under a few mm in radius ("fragmentation barrier"). In addition to these two "collision barriers", the radial drift of the particles towards the central star (induced by gas drag) is also limiting

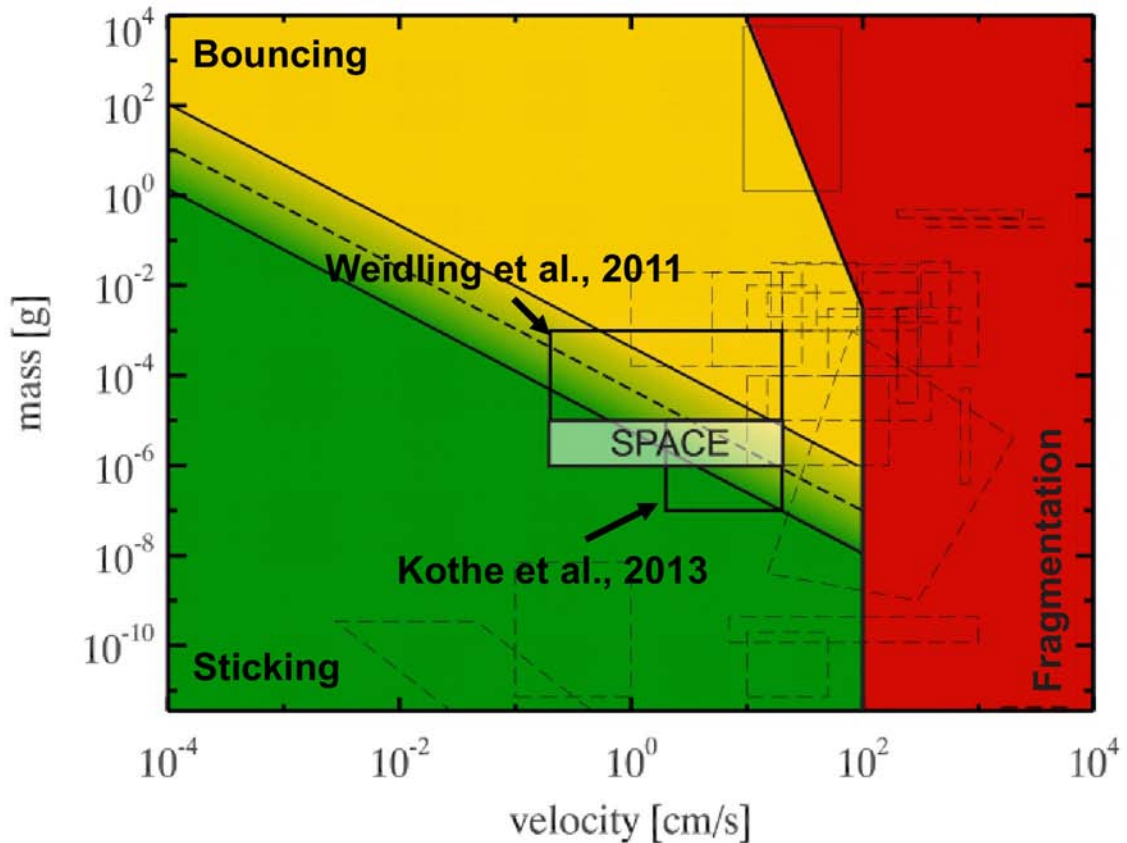


Figure 1.2: Sketch of the dust collision model elaborated by Güttler et al. (2010) and Kothe et al. (2013). The collision outcome is indicated by colors: sticking (green), bouncing (yellow) and fragmentation (red). The parameter field regions investigated by previous experiments are indicated with dashed boxes (see Güttler et al. 2010, for details). The parameters for the experiments of Weidling et al. (2012), Kothe et al. (2013), and the SPACE experiment are indicated. Image credit: S. Kothe

the particle growth (Weidenschilling 1977a). As seen in Figure 1.1, the drift velocities depend on the particle size and reach a maximum around 100 m s^{-1} for meter-sized bodies (considered at around 1 AU). At these speeds, bodies at 1 AU get lost to the central star, either by accretion or evaporation, within ~ 100 years. This systematic body loss to the central star is called "meter-size barrier".

An investigated option for overcoming these three growth barriers (bouncing, fragmentation and drift) is, for example, planetesimal formation by gravitational instability in regions of aerodynamic dust concentration, like turbulent vortices, streaming instabilities of the dust-dense disk midplane or pressure bumps in condensation regions (Johansen et al. 2007, Cuzzi et al. 2008, Chiang & Youdin 2010). Another direction of research is the growth of planetesimals by mass transfer between porous aggregates colliding at high velocities of a few m s^{-1} . Experiments have shown that even though one of the collision partners fragments, part of its mass sticks to the other colliding partner leading to a net aggregate growth (e.g. Langkowski et al. 2008, Kothe et al. 2010, Beitz et al. 2011, Windmark et al. 2012).

These barriers imply that dust agglomeration to planetesimal sizes requires more com-

Table 1.1: Microgravity time and quality for the different possible microgravity platforms. g is the Earth's gravitational acceleration.

Flight type	Microgravity time per experiment run	Microgravity quality
Drop tower Bremen	up to ~ 9 s	$< 10^{-6}g$
Parabolic flight	~ 20 s per parabola	$\sim 10^{-2}g$
Suborbital rocket flight	a few minutes	$\sim 10^{-4}g$
Orbital flight	up to several months (International Space Station)	$\sim 10^{-6}g$

plex processes than simple growth upon collision. Information about aggregate collision behavior at masses and velocities around the transitions between sticking and bouncing and between bouncing and fragmentation are therefore very important for the further investigation of dust growth in PPDs. The Suborbital Particle Aggregation and Collision Experiment (SPACE) is part of a series of experiments attempting to better define the parameters leading to aggregate sticking, bouncing or fragmenting upon collision.

1.4 The SPACE experiment

One of the challenges of observing dust collisions in many-particle systems at gentle velocities of 10 cm s^{-1} and below is the necessity to conduct these experiments under microgravity conditions. Weidling et al. (2012) and Kothe et al. (2013) performed their experiments in the drop tower at the Center of Applied Space Technology and Microgravity (ZARM) in Bremen, where each experiment run can last up to 9 s (microgravity time while the experiment capsule is in free-fall).

Other possibilities for conducting microgravity experiments include parabolic flights on an airplane, suborbital flights on a rocket or orbital flights on either an orbital vehicle or the International Space Station. Table 1.1 lists the associated microgravity times and qualities. The best microgravity qualities are reached at the drop tower and on orbital flights. The drawbacks are a short microgravity time of 9 s at the drop tower and very high flight costs on orbital vehicles. A good compromise between microgravity time and financial costs are suborbital rockets. Compared to parabolic or drop tower flights, however, they are not easily repeatable. With the REXUS project¹, the SPACE experiment got the valuable opportunity to fly on-board a suborbital rocket. REXUS stands for Rocket EXperiments for University Students and is a joint project between the Deutsche Zentrum für Luft- und Raumfahrt (DLR) and the Swedish National Space Board (SNSB). The rocket reaches apogees of ~ 100 km and the time lapse during which the on-board experiments are under reduced gravity conditions is significantly increased compared to

¹<http://www.rexusbexus.net/>

drop tower or parabolic flight experiments, allowing for a "long-term" evolution of a dust aggregate system.

The SPACE experiment was selected in February 2011 to fly on the REXUS 12 rocket. In the process of hardware building and testing, SPACE was also flown at the drop tower in Bremen in August 2011, delivering additional dust collision data that completed the data obtained during the suborbital flight. On March 19th, 2012, SPACE was launched on-board the REXUS 12 rocket, from the Esrange launch site near Kiruna, in Northern Sweden. The successful experiment run allowed for the continuous observation of collisions between sub-mm-sized dust aggregates for about 150 s.

1.5 This work

Section 2 describes the SPACE experiment design-driving requirements and the hardware set-up. Section 3 details the different experiment runs and the hardware performance at the drop tower and during the REXUS 12 suborbital flight. In Section 4, the dust aggregates investigated with SPACE are described.

Section 5 specifies the methods used for the analysis of the SPACE data. In particular for the suborbital flight data, the data analysis and validation was not trivial. In Section 6, the results obtained from the different SPACE experiments are presented. Section 7 draws a few conclusions on sub-mm-sized dust aggregates collision behavior from the experimental data obtained. In addition, some properties of clusters composed of sub-mm-sized aggregates are investigated.

2 Experiment Description

This section describes the Suborbital Particle Agglomeration and Collision Experiment (SPACE), the design-driving requirements (Section 2.1) and the experiment set-up fulfilling these requirements (Section 2.2).

2.1 Experiment design requirements

2.1.1 Experiment objectives

As the SPACE experiment was built to investigate the collision behavior of sub-mm-sized dust aggregates, two main design requirements for the hardware were first, to generate observable dust aggregate collisions under vacuum conditions and second, to record video data of these collisions for later analysis.

To create the required environment for aggregate collisions, the dust aggregates needed to be placed into experiment cells of the appropriate size, with non-adhesive walls. These cells had to shake the aggregates at different velocities during the experiment run to keep the aggregates in the cell inner volume and control their relative velocities. Furthermore, the cells had to provide vacuum conditions for the dust aggregates to collide without any influence of ambient gas.

The observation of the aggregate collisions required the cell walls to be transparent as well as the implementation of an illumination system. A camera with the appropriate resolution and frame rate had to capture the collisions during the experiment run. The camera frames then had to be recorded on a retrievable and robust data storage device to be used in the experiment data analysis.

2.1.2 Carrier requirements

In addition to fulfilling the experiment objectives, the SPACE hardware also had to comply to the requirements of its carrier, the REXUS rocket. The following paragraphs describe and quantify these requirements.

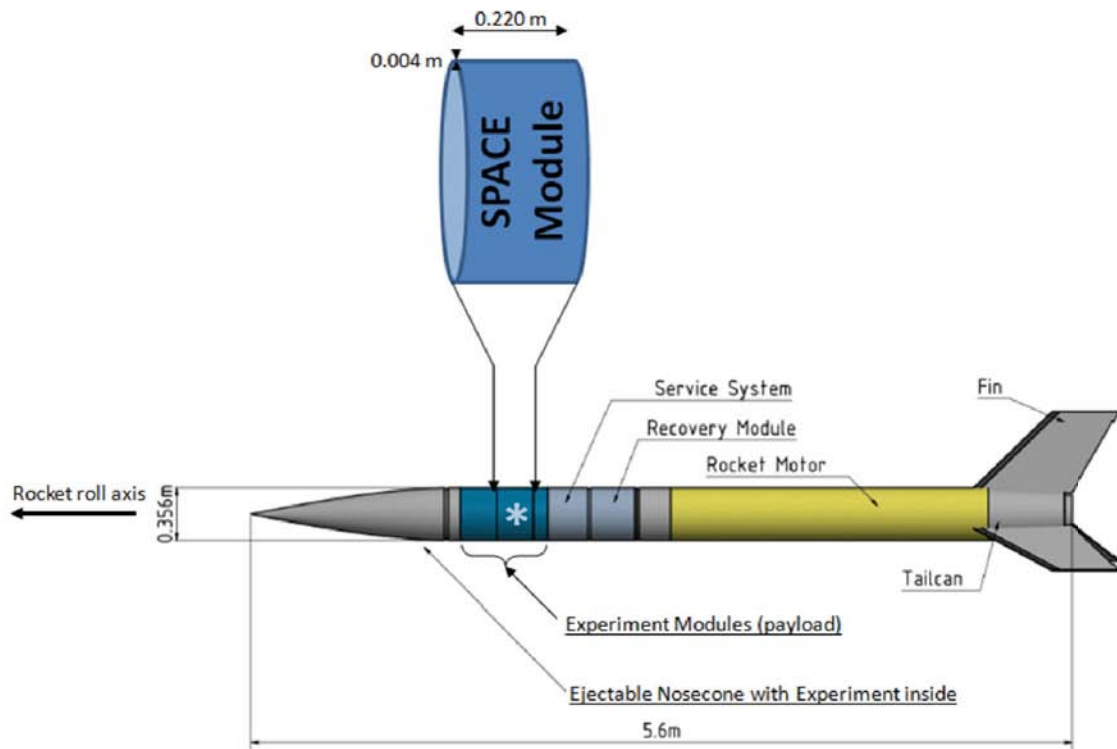


Figure 2.1: Scheme of the REXUS 12 rocket components and payload configuration. REXUS 12 flew four experiments including one under the nosecone. The location of the SPACE experiment is marked with an asterisk and its dimensions are indicated. Image credit: S. Kothe.

Experiment size and mass: Experiments flying on the REXUS rocket have to fit into an experiment module, which is an empty cylinder of 355.6 mm (14") in diameter, 4 mm wall thickness and, in the case of the SPACE experiment, 220 mm height. The actual available height, however, was reduced by the presence of the lower and upper bulkhead. This bulkhead was a 4 mm thick baseplate on which the experiment components could be accommodated. The lower bulkhead supported the SPACE components and the upper one supported the neighbor experiment, as in the final rocket configuration the experiment modules were screwed together to form the payload part of the rocket (see Figure 2.1). Hence, the volume available for accommodating the SPACE experiment was a cylinder of 355.6 mm diameter and 200 mm height.

The typical payload mass on a REXUS rocket is between 40 and 60 kg, comprising 3 to 5 experiments with their modules and bulkheads. The experiment weight limitations are not as restrictive as the size limitations. However, a heavier payload reduces the height of the trajectory apogee and therefore the total microgravity time for experiment runs. Hence, the experiment design should try to keep the weight as low as possible. The objective for the SPACE experiment was a weight between 10 and 15 kg.

Experiment autonomy: An additional implication of flying the experiment on the REXUS rocket was the need for a high degree of autonomy, compared to drop tower experiment runs for example, where data recording and storage were supplied. REXUS did provide power and signal channels, allowing the sending of commands to activate components during the flight. However, the flight time was very short (~ 10 min) and subjected to communication losses. As the SPACE experiment timeline events were very time critical (subsystems switching sequence), the experiment required its own control system to run the event sequence autonomously during the flight.

Rocket interfaces: The bulkhead and the module's inner skin were the mechanical interfaces from the experiment to the rocket. The roll axis (see Figure 2.1), being the direction of lift-off and landing, was the line of strongest loads. This means a rather uniform weight distribution of the experiment components on the bulkhead was recommended. The experiment hardware needed to have a center of gravity as close as possible to the rocket roll axis and to be mechanically designed to survive the launch, re-entry and landing loads (see below and the REXUS Manual, Eurolaunch 2010).

In addition the evacuation of the SPACE vacuum chamber required a late access connection to the hardware inside the experiment module. Indeed, the pumps needed for evacuation could not be implemented in the experiment hardware. To be able to evacuate the chamber as late as possible before launch, an umbilical was required.

The electrical interface between experiment and rocket is also described in the REXUS Manual (Eurolaunch 2010). It consisted of a female D-SUB 15 connector on the rocket side delivering power, signals and a communication interface. During the flight, power was delivered to the experiments by the REXUS Service Module's batteries. Each experiment was provided with about 28 W at 1 A for nominal consumption and up to 3 A peak consumption (through the 28 V line of the REXUS Service Module). Through the D-SUB 15 connector, the Service Module also delivered three signals, Lift-Off (LO), Start Of Experiment (SOE) and Start Of Data Storage (SODS). The LO signal was automatically sent to all experiments at lift-off, while the SOE and SODS signals could be implemented as required by each experiment.

The telemetry and telecommand interface to the rocket was also included in this connection. It allowed receiving hardware health and status information during the flight and operated the experiment during the numerous tests and simulations prior to the flight. It consisted of an RS422 interface to the Service Module which required a baud rate of 38.4 kb s^{-1} for both up- and downlink. Each experiment was responsible for the formatting of their telemetry and telecommand data.

The rocket itself also provided a thermal interface by contact surfaces to the experiments. It was required for the experiments to not heat up the module skin nor the air interfaces with neighboring experiments to more than $10 \text{ }^\circ\text{C}$ above the ambient temperature. Parts interfacing with other modules should not heat up to more than $+50 \text{ }^\circ\text{C}$ and parts in contact with Service Module cables no more than $+70 \text{ }^\circ\text{C}$ (see the REXUS Manual, Eurolaunch 2010).

Launch site conditions: The launch site conditions also set a certain number of constraints on the experiment hardware design choices. Kiruna, in northern Sweden, is situated North of the Arctic circle, at a latitude of 67 °North, and can still have very low outside temperatures of down to -40 °C during REXUS launch campaigns (usually in March). Most of the time, experiments stayed protected inside of the Esrange premises, at room temperatures of about 17 °C. However, after the rocket launcher was elevated, a countdown hold could have left the hardware exposed to the low outside temperature for an indefinite period of time. The experiments had therefore to be reliably functional at -40 °C.

Another constraint was set on the experiment durability by the numerous tests and simulations that were part of the REXUS launch preparation protocol. The hardware had to be able to survive a very high number of power cycles and still be functional for the actual flight.

Flight and landing conditions: The launch phase of the rocket was one of the most critical flight phases for the experiment hardware. The maximum acceleration load of about 20g, g being the Earth's gravitation acceleration, was reached a few seconds after launch (see Section 3.2.1 for more details). In addition, the rocket rotated at about 3 to 4 Hz inducing centrifugal loads of up to 11g inside the experiment module.

The hardware also had to withstand the launch vibration loads. The REXUS sinusoidal qualification levels were at 0.124 m s^{-1} for 10-50 Hz and 4g for 50-2000 Hz on all three axes, and the random vibration levels were at $6g_{\text{RMS}}$ for 20-2000 Hz, g_{RMS} being the random vibration root mean square acceleration (see Eurolaunch 2010).

During the reduced gravity phase, the experiment experienced disturbance accelerations due to both the residual atmosphere it was flying through, and the residual rocket spin. After launch, the rocket was de-spun by releasing two masses on strings (Yo-Yo mechanism) but still rotated at about 0.03 Hz (see Section 5.6.1 for a detailed calculation of the flight residual accelerations). As they were free-flying during this phase of flight, the dust aggregates inside the SPACE experiment cells had a tendency to gather in one corner of the cell due to the residual accelerations, reducing or even stalling inter-aggregate collisions. It was therefore essential to take this effect into account during the experiment design and to create a cell shaking mechanism that counteracted these disturbances.

Finally, the hardware, or at a minimum the memory card containing the experiment data, needed to survive payload re-entry and landing. During re-entry, the experiment module's skin temperature reached peaks above 200 °C, which partly transferred to the inner hardware. The maximum load during the descend was expected to be about 5g at opening of the parachutes. The payload then was planned to touch the ground at a velocity of around 10 m s^{-1} . As the rocket could land into snow or water, it was essential for the experiment to be completely decoupled from power latest during re-entry to avoid electrical shortcuts and data loss.

2.2 Experiment set-up

The overall set-up of the SPACE experiment can be seen in Figure 2.2. For the flight on the suborbital rocket, the dust samples investigated were placed inside three glass cells which were accommodated into a vacuum chamber. The cells were backlit by an LED array and the collisions between aggregates were observed with a high-speed camera through a viewport. The following paragraphs describe the experiment set-up and the components used. A table with a detailed list of the experiment components can be found in appendix A.

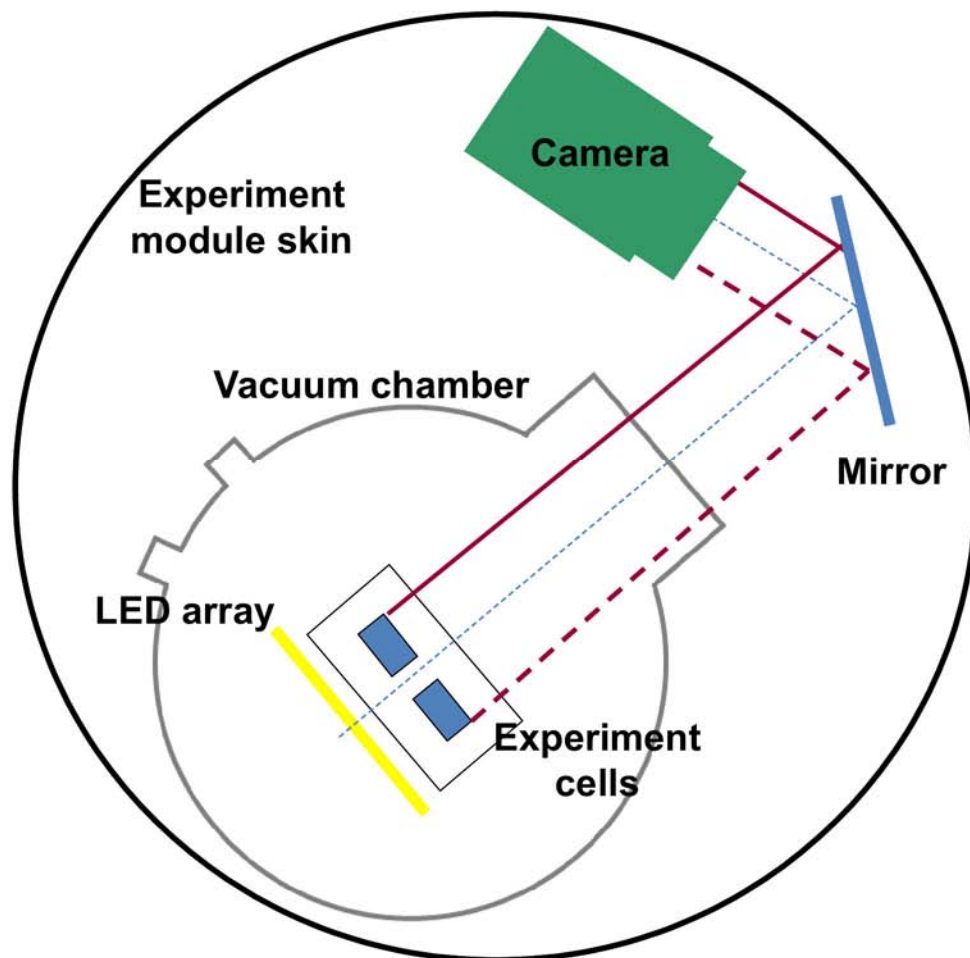


Figure 2.2: Scheme of the overall set-up of the SPACE experiment. The solid and dashed lines indicate the optical path of the light from the LED array behind the experiment cells to the camera sensor.

2.2.1 The mechanical design

Figure 2.3 shows the experiment hardware accommodated on the module bulkhead and inside the module skin. Figure 2.4 shows the hardware inside the vacuum chamber.

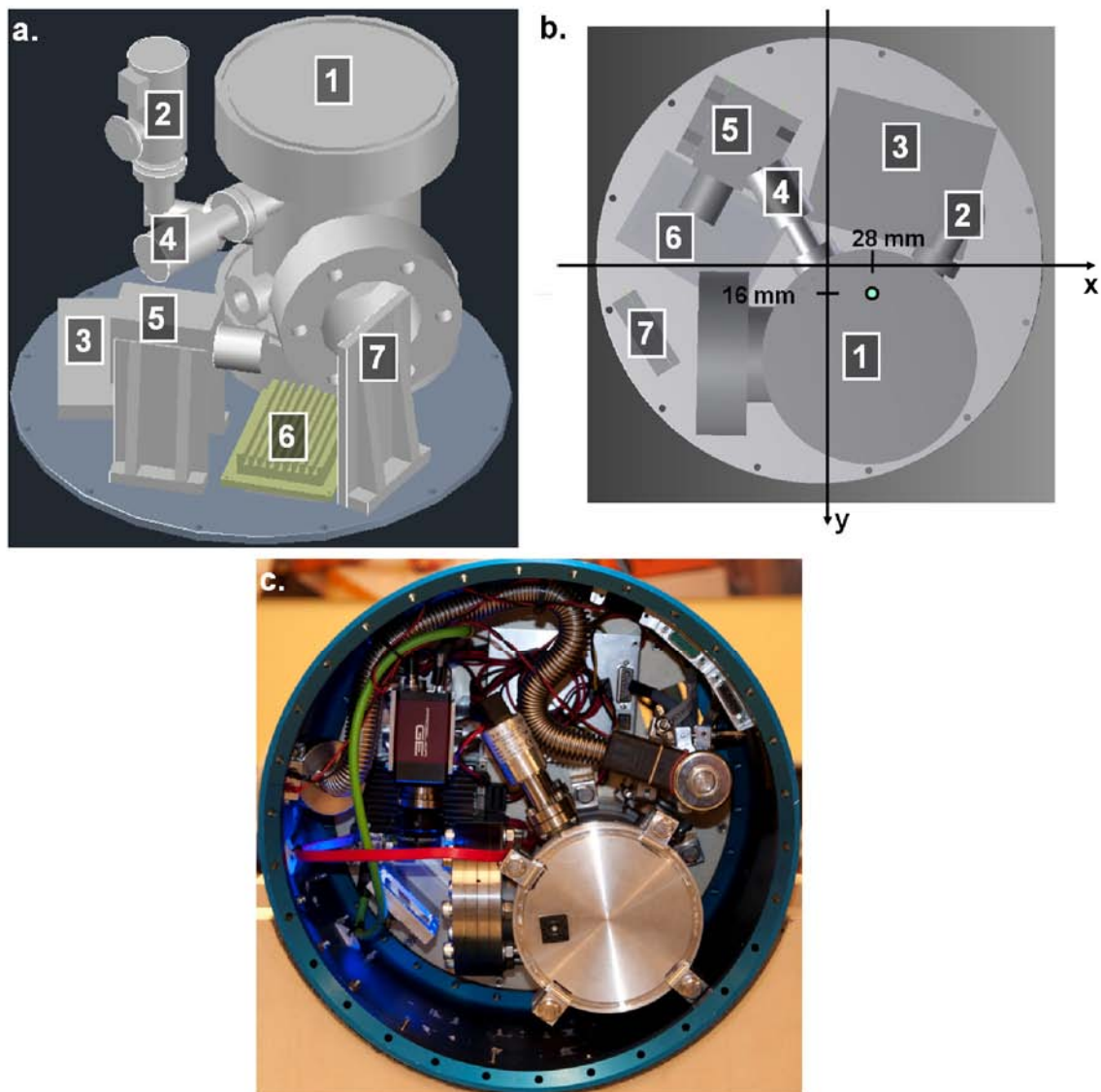


Figure 2.3: SPACE experiment hardware accommodated on the REXUS module bulkhead: a. side view CAD drawing, b. top view CAD drawing of the hardware on the bulkhead. The position and coordinates of the experiment center of gravity are indicated (green circle). c. top view photograph of the hardware inside the experiment module skin (blue outside cylinder). Image credit: D. Heißelmann. The numbers indicate 1. the vacuum chamber (without the clamps, screws and feed-through in a. and b.), 2. the vacuum valve, 3. the electronics box, 4. the pressure sensor, 5. the camera, 6. the on-board computer and 7. the mirror.

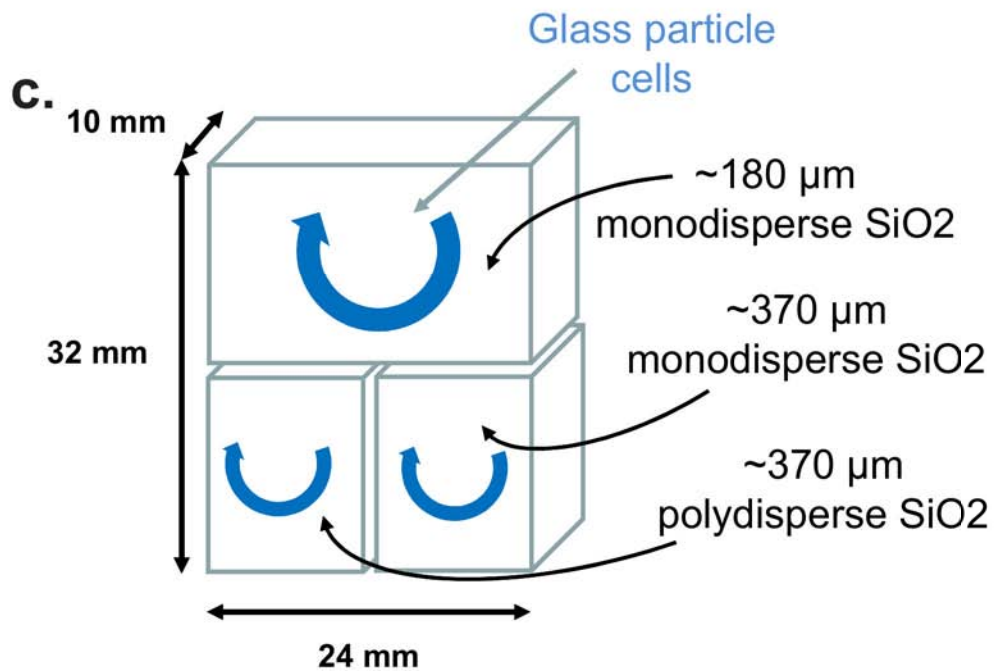
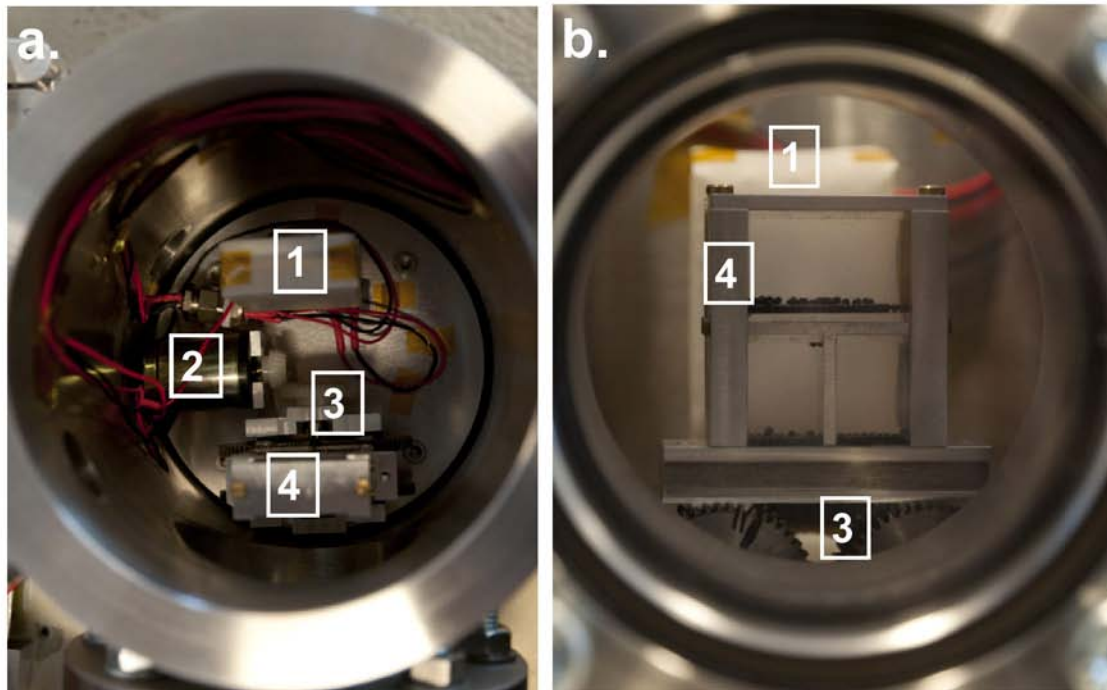


Figure 2.4: SPACE experiment hardware accommodated inside the vacuum chamber: a. top view photograph, b. front view photograph through the vacuum chamber viewport. Image credits: D. HeiBelmann. The numbers indicate 1. the LED array covered with diffusion paper, 2. the shaking motor, 3. the shaking mechanism cog wheels and 4. the experiment cells. c. scheme of the three experiment glass cells with their dimensions and circular motion indicated. The types of dust inserted into each cell are also specified: aggregates composed of monodisperse SiO_2 dust with mean sizes of $180 \mu\text{m}$ in the top cell, and $370 \mu\text{m}$ in the right bottom cell, and aggregates composed of polydisperse SiO_2 with a mean size of $370 \mu\text{m}$ in the left bottom cell (see Section 4.4.2 for details).

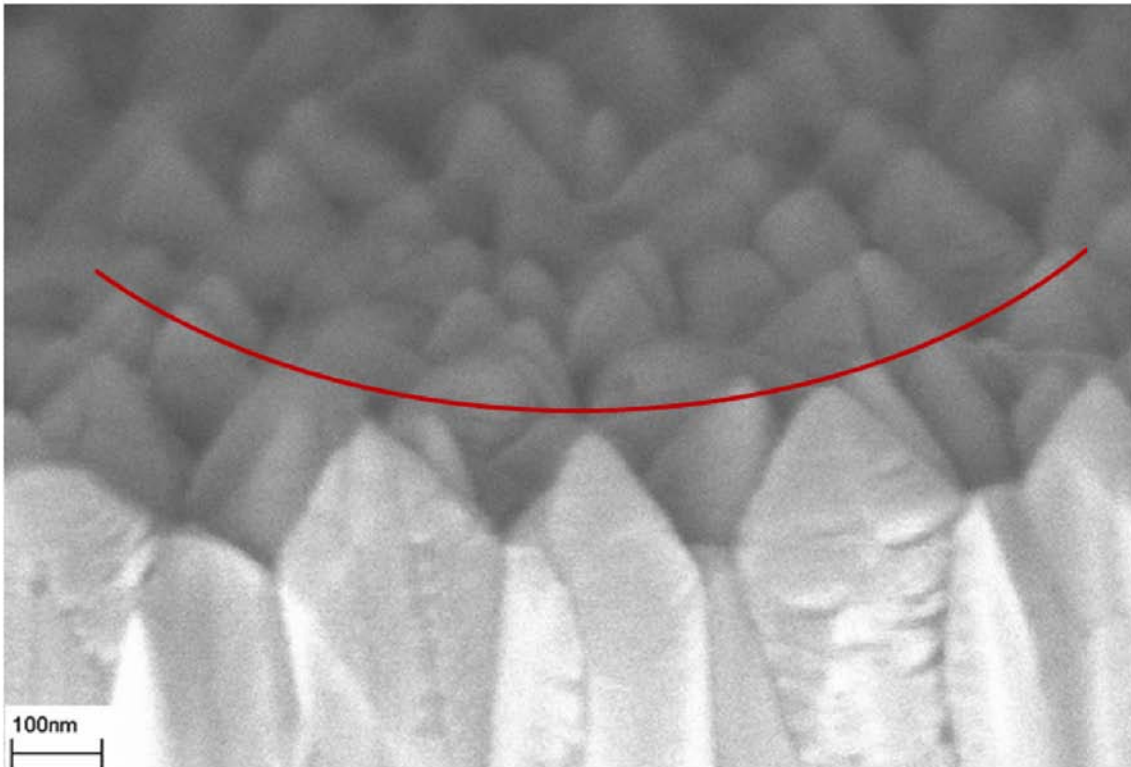


Figure 2.5: SEM image of the nano-particle coating on the inner walls of the SPACE glass cells. The red arc represents the typical size of a dust monomer particle of about $1\ \mu\text{m}$ in diameter (constituent of a dust aggregate) colliding with the wall. Image credit: Oliver Lenck.

The experiment cells: The experiment cells were three rectangular glass boxes held together by an aluminum frame (see Figure 2.4c). Two of these cells were smaller with dimensions of $11\times 10\times 15\ \text{mm}^3$ placed next to each other and the third was about twice as big with $24\times 10\times 15\ \text{mm}^3$ on the top of the two other ones. This cell disposition was optimal for the aluminum frame to resist launch acceleration loads.

The glass used to build the cells was Borofloat 33 technical glass (manufactured by Schott AG), which was able to resist mechanical and thermal loads better than normal glass. This borosilicate glass had a coefficient of thermal expansion lower by a factor of about 3 compared to standard soda lime glass (manufacturer information, Schott AG), resulting in less mechanical stresses due to thermal deformation. In addition, the interfaces between the glass and the aluminum frame were covered with Kapton tape (manufactured by DuPont) to absorb thermal deformations of the materials and reduce the stresses on the glass during launch preparation and flight.

As silicate dust aggregates tend to stick to glass surfaces, the glass was covered with a non-adhesive coating on the inner cell side, provided by the Fraunhofer Institute for Surface Engineering and Thin Films of Braunschweig. To produce this coating, nano-particles of ZnAlO were deposited on the glass surface, creating narrow peaks that prevented (much bigger) dust particles to stick to it by reducing the contact surface significantly (see Figure 2.5).

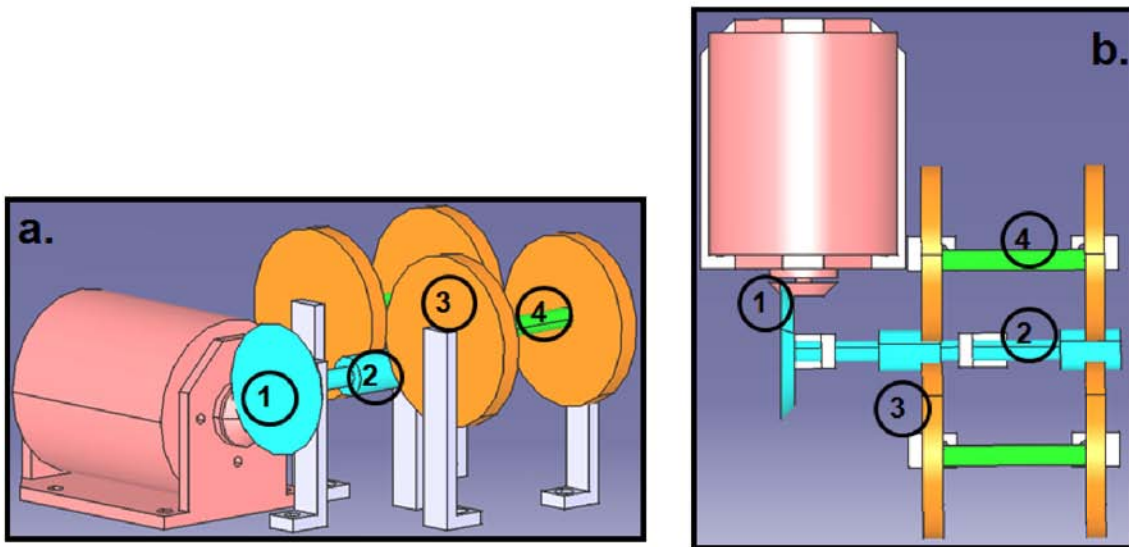


Figure 2.6: 2D-shaking mechanism of the SPACE experiment: a. side view of the shaking mechanism CAD drawing. The transmission ratios were 2:1 behind the motor (1) and 10:1 from the central axis to the shaker frame (2). b. top view of the shaking mechanism CAD drawing. The numbers stand for: 1. the two conical cog wheels, 2. the central axis outfitted with two cog wheels (blue), 3. the four experiment cells frame cog wheels (orange) and 4. the experiment cells excentered axes (green). The experiment cells' frame is not depicted. The motor can be seen in pink.

The shaking mechanism: The shaking of the experiment cells containing the dust aggregates was essential for two reasons: first, it compensated for residual accelerations induced by the rocket flight and kept the aggregates in the inner cell volume, where they could collide with each other. Second, it allowed control of the aggregate relative collision velocities, and thereby the type of collisions observed: either sticking collisions at low velocities or bouncing and aggregate fragmentation at higher velocities.

The quality of the microgravity during the parabolic portion of the rocket's trajectory was expected to be disturbed by the effects of residual accelerations, namely the drag of the residual atmosphere at the flight altitudes of the rocket, and the centrifugal acceleration due to the residual rocket spin at about 0.03 Hz (see Section 5.6.1 for details). These two accelerations acting on the dust aggregates had perpendicular directions. The atmospheric drag acted in the rocket flight axis, while the centrifugal spin acted in the outward radial direction. In order to compensate for both of these disturbances, the shaking mechanism was designed to agitate the cells in two dimensions by applying a circular motion. The concept and set-up of this shaking mechanism are depicted in Figure 2.6. A conical transmission of 2:1 (1) transmitted the motor rotation to a central axis (2). This axis was outfitted with two cog wheels transmitting the motion to the four shaker frame wheels (3) with a ratio of 10:1. Excentered axes (4) at 1 mm off center supported the experiment cells frame and induced their circular motion. The velocity profile with which the shaking mechanism agitated the cells during the SPACE experiment runs is described in Sections 3.1.2 and 3.2.2).

Table 2.1: SPACE mechanical characteristics

Experiment mass [kg] (with module and bulkhead)	14.7
Experiment dimensions [m]	$\varnothing 0.355 \times 0.190$
Experiment footprint are [m ²]	0.0493
Experiment volume [m ³]	0.005
Experiment center of gravity position [mm]	x: -28, y: 16, z: 117 (see Figure 2.3b.)

The mechanical structure of the experiment: As can be seen in Figure 2.3, most of the experiment components were accommodated on the REXUS module bulkhead. This allowed for a high load resistance along the rocket roll axis. The heaviest piece of hardware was the vacuum chamber with 6.9 kg. As it had to be positioned slightly off-center to allow for the correct optical path between the experiment cells and the camera, the center of gravity of the entire experiment was shifted off-center (see Figure 2.3b). The SPACE experiment module was placed as close as possible to the overall rocket center of gravity, in the configuration after motor and nosecone separation, in an attempt to reduce residual accelerations due to spinning or tumbling during flight (see Figure 2.1 for the location of the SPACE module on the REXUS 12 rocket).

The pressure sensor and the vacuum valve were the only components not fixed to the bulkhead but to the vacuum chamber. Both parts weighed 131 g and 462 g, respectively. The pressure sensor was attached to a CF-16 flange via 6 screws and the vacuum valve was attached to a KF-16 flange with a ring shell. These accommodations were designed to resist the rocket flight and landing loads.

Inside of the vacuum chamber, all the components were accommodated on the bottom flange to ensure mechanical robustness (see Figure 2.4). The most sensitive connections were the cog wheel transmissions between the experiment cells and the motor. During a drop tower campaign and a vibration test at REXUS flight loads, it was demonstrated that the hardware was able to resist all flight phases (see Annex C.6).

Table 2.1 summarizes the mechanical characteristics of the SPACE experiment set-up.

The thermal interfaces: In addition to mechanical requirements, the REXUS rocket also set thermal requirements on the experiment hardware. The thermal behavior of the SPACE components and the implemented countermeasures are listed in Table 2.2. The piece of hardware heating up the most was the on-board computer with up to 60°C. To avoid overheating, a heat-sink plate was mounted to the computer. The other electrical components were all mounted to the metal structure of the experiment allowing them to evacuate the heat generated.

Table 2.2: SPACE components thermal characteristics and experiment heating countermeasures.

Component likely to generate heat	Material	Nominal operation range	Highest expected temperature	Countermeasure
Motor	Outer shell: steel/brass	-30 to 85°C	45°C	Motor mounted to an aluminum plate connected to the vacuum chamber bottom flange (aluminum).
LED array	Electronic components, e-board material and aluminum	-30 to 50°C	50°C	LED array mounted in an aluminum frame connected to the vacuum chamber bottom flange (aluminum).
Camera	Outer shell: aluminum	0 to 50°C	45°C	Camera mounted to an aluminum frame connected to the REXUS bulkhead.
Electronics box	Electronic components and E-board material	-30 to 50°C	50°C	E-Box mounted to an aluminum box connected to the REXUS bulkhead.
Single-board computer (SBC)	Electronic components and E-board material	0 to 60°C	60°C	Heat-sink plate mounted to SBC.

2.2.2 The vacuum system

The purpose of the vacuum system was to be able to observe aggregate collisions without any influence of gas on the particle trajectories and collisions. The vacuum chamber was cylindrical with an inner diameter of 100 mm. The top and bottom plates were aluminum blind flanges attached to the chamber core via four double-claw clamps each (ISO-K configuration). The vacuum chamber was outfitted with a CF-63 flange for the viewport, a CF-16 flange for the pressure sensor, another CF-16 flange for the electrical feed-through (8 copper pins) and a KF-16 flange for the vacuum valve.

The experiment was evacuated with a pre-vacuum and a turbo-molecular pump. For obvious dimension and weight reasons, the pumps could not be accommodated inside the experiment module. Therefore, the evacuation took place before the rocket launch, through a module skin umbilical (see Figure 2.7a.). This umbilical was a cylinder oriented towards the bottom of the rocket forming a 30 deg angle with the REXUS module skin. It was outfitted with a KF-16 flange, where the hose coming from the SPACE experiment was connected, and two electrical pins for the valve power connection. Inside the experiment module, the umbilical was placed at an appropriate distance of the SPACE vacuum valve in order to fit the 500 mm hose connecting the umbilical to the vacuum chamber inside the experiment module. The valve was electro-magnetically operated (EVC 110 M manufactured by Balzers). It required 125 W when open, and was powered externally before launch.

To allow for continuing the evacuation as late as possible before launch, in order to optimize the vacuum quality inside the vacuum chamber during the flight, the turbo-molecular and pre-vacuum pumps were accommodated into a Zarges box and fixed to the rocket launcher. A rubber hose connected the turbo-molecular pump to the experiment umbilical (see Figure 2.7b for a pre-integration configuration). The experiment vacuum valve was closed 120 s and the pumps shut-off 115 s and 60 s before lift-off (turbo-molecular and pre-vacuum pump, respectively). At lift-off, the rubber hose tore apart from the umbilical.

2.2.3 The data acquisition and storage systems

The data acquisition system comprised the optical components (LED array and mirror), the camera and the on-board computer. The LED array was composed of 86 blue LEDs distributed over 9 rows and was covered with diffusion paper to uniformize the background illumination. Each LED had an intensity of 8200 mcd and a dominant wavelength of about 470 nm (468 to 474 nm, blue). This color was chosen as the camera sensitivity was better at this wavelength than for other commercially available LEDs.

The optical path between the background illumination and the camera can be seen in Figure 2.2. To accommodate the experiment inside of the rocket module, a mirror was introduced between the viewport and the camera lens. The lens attached to the camera had 23 mm focal length and the aperture was set to 1.4.

The camera used for recording the dust collisions was the Allied Vision Prosilica GE680 (see Table 2.3 for camera details). This camera recorded 640×480 px 8-bit grayscale

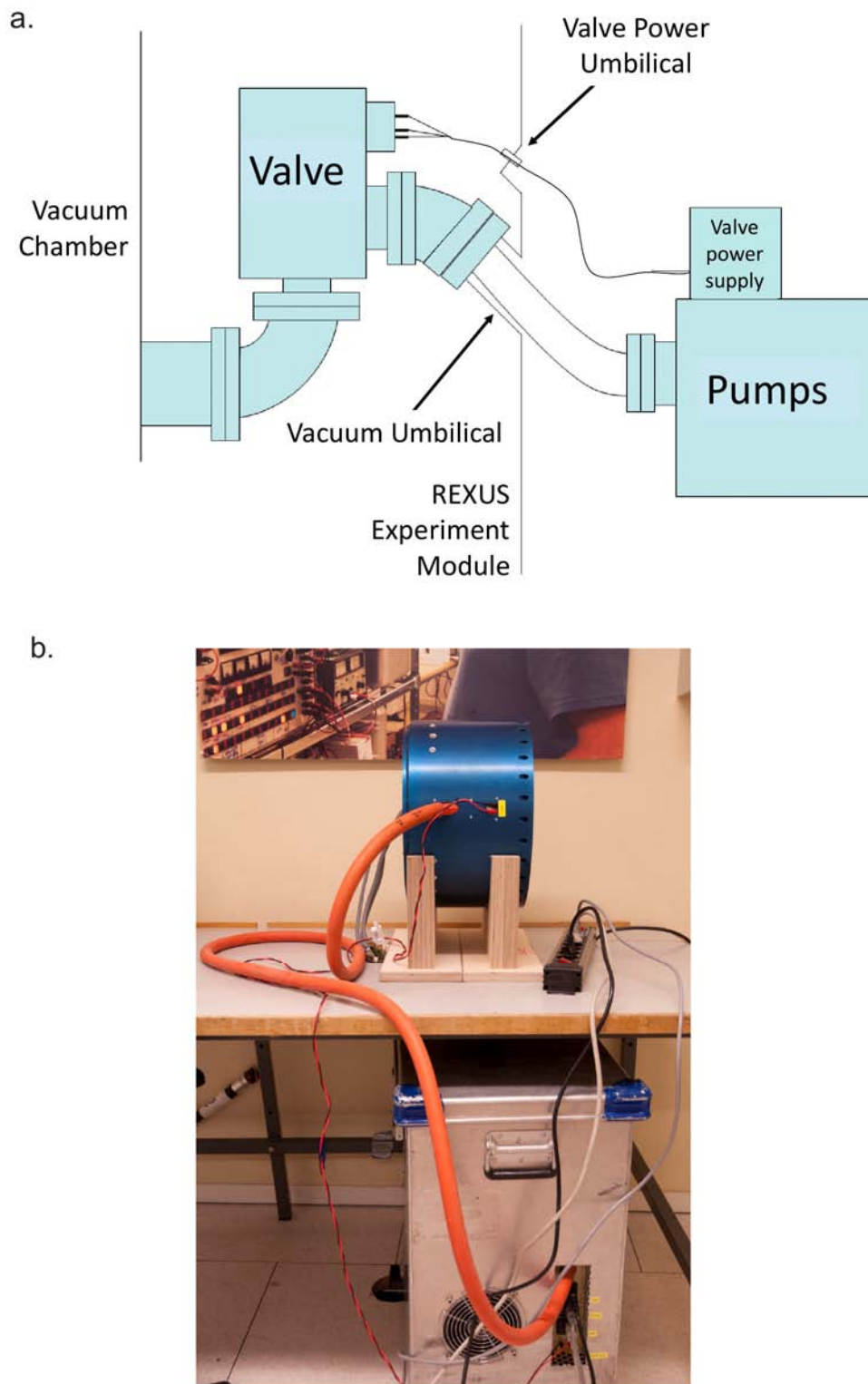


Figure 2.7: SPACE vacuum umbilical for late evacuation before launch. a. scheme of the umbilical concept, b. photograph of the SPACE module (blue cylinder on the table) being evacuated before integration into the REXUS 12 rocket. The Zarges box containing the pumps can be seen under the table. Image credit: D. Heißelmann

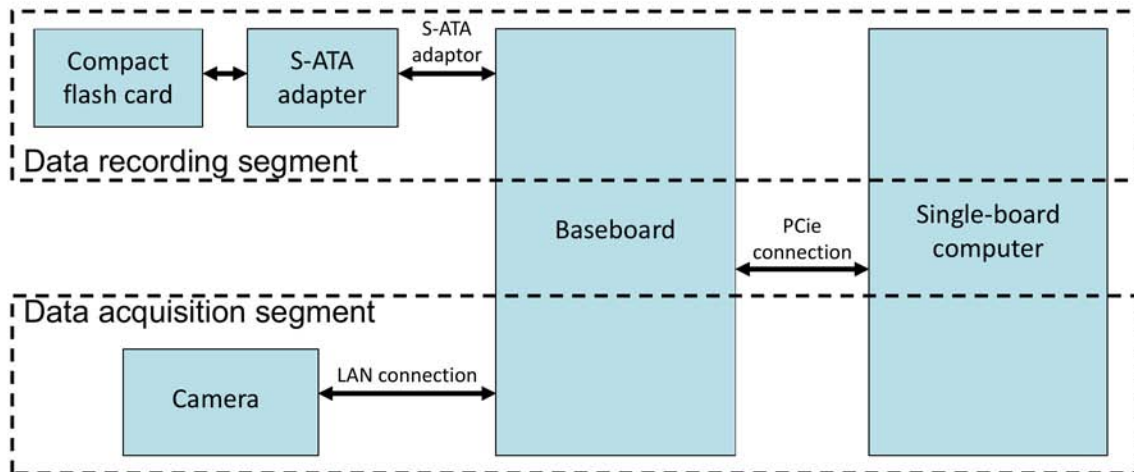


Figure 2.8: Diagram of the SPACE data acquisition and storage system concept.

Table 2.3: Prosilica GE680 Characteristics.

Allied Vision Prosilica GE680	
Maximum acquisition speed possible	205 fps
Maximum resolution	640×480 px
Camera control	External
Data storage	External
Weight	170 g
Dimensions	39 x 51 x 80 mm ³
Power consumption	4.5 W at full capacity

frames at a rate of 170 frames per second. Its small dimensions and light weight made it an appropriate compromise for use in a rocket experiment. However, its lack of autonomy was a major constraint: having neither internal command nor memory units, it needed external control and data storage systems for acquiring and recording data.

The camera control was performed by a single-board computer provided with a Linux Server edition and a C++ program for running frame streaming and recording. The single-board computer used in the SPACE experiment was the Robin Module from Toradex with the corresponding Daisy nano-ITX baseboard. These components were also chosen as a compromise between their size and weight and their capacities (see Table 2.4 for details). The two most crucial abilities needed were an adequate processor speed to record the incoming camera frames and an Ethernet controller that supported so-called "Jumbo frames" required by the Prosilica GE680 frame format at frame rates above 150 fps. Table 2.4 lists the details of data rate and quantity produced during the SPACE experiment run on the suborbital rocket. To be able to perform a 180 s stream at 170 fps in this hardware configuration, 1.5 GB of the Robin flash memory and 5 GB of the data storage flash card were allocated as swap space. In addition, the Linux Server kernel was tuned to highly prioritize the data acquisition and storage. Even with these measures to increase the computer streaming capacities, 170 fps was the highest frame rate at which recording was reliable.

Table 2.4: Data acquisition system requirements and characteristics

Data requirements	
Camera resolution	480 x 640 px
Bytes per frame	307200 B/f
Acquisition speed during the SPACE experiment	170 f/s
Data Rate	52.2 MB/s
Total Data Quantity (for 180 s recording)	9.4 GB
Robin module characteristics	
CPU	Intel Atom Z530
Clock Rate	1.6 GHz
CPU Type	533 MHz Front Side Bus
Power dissipation	5 W
RAM	1 GByte DDR2 533 MHz
Flash disk	4 GB
Throughput	10/100/1000 Mbit LAN
Ethernet Controller	RTL 8111D
Weight	40 g
Dimensions	55 × 84 × 5 mm ³
Power consumption	6 W
Daisy baseboard characteristics	
Connections used by the experiment set-up	PCIe Ethernet LAN S-ATA
Weight	71 g
Dimensions	72 × 100 × 10 mm ³

Figure 2.8 depicts the data acquisition and storage system concept. The experiment on-board computer streamed frames from the camera via an Ethernet cable and directly stored them on an external CompactFlash card via an S-ATA connection. The required storage space was about 10 GB at a data rate of 52 MB/s

2.2.4 Electronics

The requirement for an autonomous run of the experiment necessitated the inclusion of an electronics board into the experiment design. This board had a certain number of functions:

- power distribution as required to the different electronic components, namely the computer, the flashcard adapter, the camera, the LED array and the shaker motor as well as to its own components like the microcontroller, the servo-controller and the solid-state relays
- execution of the experiment timeline during the rocket flight (switching of the camera, the LED array and the motor at the required time)
- control of the shaking speed of the motor (to run the shaking sequence)
- generation of health and status telemetry for the ground station
- handling commands from the ground station while in test mode (hardware and interface tests before launch)
- record the pressure sensor data.

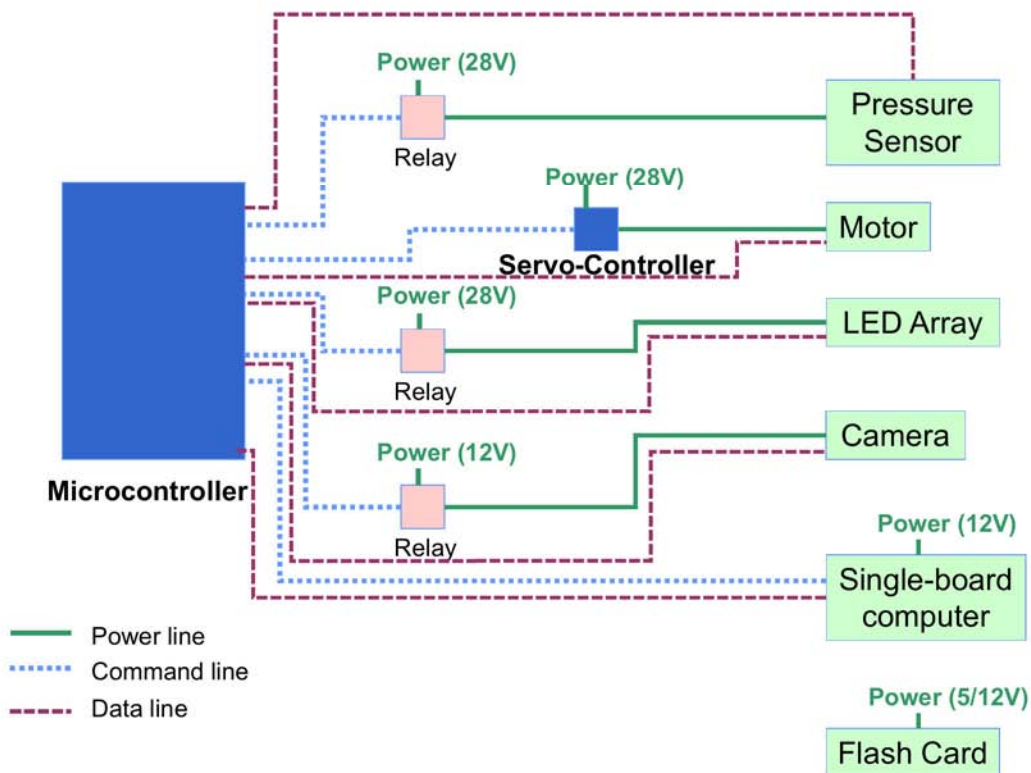


Figure 2.9: Diagram of the SPACE electronics concept. Components listed on the right of the diagram (green boxes) are not on the electronics board.

Table 2.5: SPACE power consumption summary table.

Component	Expected power consumption	Voltage required
Shaker motor	6 W	28 V
LED array	1.5 W	28 V
Electronic components	5 W	5 V
Camera	4.5 W	12 V
Camera control and data storage	7 W	12 V
Pressure sensor	0,3 W	28 V
Total	24.3 W	

Figure 2.9 shows a diagram of the electronics concept. The board provided power lines to the experiment components (green boxes), command lines to the relays (blue dotted lines) that switched power to the experiment components, and data lines for reading the components' power consumption as well as recording the pressure sensor readings (purple dashed lines). The electronics circuit diagram and board print can be seen in Annex B. The microcontroller ATmega32 (Atmel), the servo-controller LS6202 (SGS-Thomson) and the solid-state relays DMP6301A (Crydom) were chosen for their adequate capacities and robustness.

The power consumption of the different experiment components measured in the laboratory is listed in Table 2.5. The total nominal and peak consumption did not exceed 25 W and could meet the REXUS requirements.

2.2.5 The software and experiment sequence

To run the SPACE experiment, three pieces of software were required. The first was a *Basic* code on the microcontroller. This software ran the experiment sequence by switching components on and off, either according to a time table (experiment sequence), or upon reception of Service Module signals. It also controlled the motor input voltage to run the shaker sequence. The second piece of software was a *C++* code on the on-board computer, whose function was to execute the frame streaming and recording during the experiment run. Finally a *Shell* script, also on the on-board computer, set up the connection to the camera and started the *C++* code.

Figure 2.10 depicts the software concept: the software was held by the microcontroller and single-board computer and commanded the motor, LED array, camera and CompactFlash card upon signals received from the REXUS Service Module. The experiment sequence during the REXUS rocket flight ran as follows:

- as soon as the experiment was powered, the electronics board, computer, and flash card were powered
- at reception of the Start Of Experiment (SOE) signal, the camera and the LED Array were powered
- at SOE + 30 s, the microcontroller ran through the shaking sequence
- at SOE + 180 s, the shaker motor, the camera and the LED array were powered off and the single-board computer was switched to stand-by mode
- 300 s after lift-off, the experiment was powered off by the REXUS Service Module.

The implementation of this experiment sequence into the flight timeline is shown in Section 3.2.

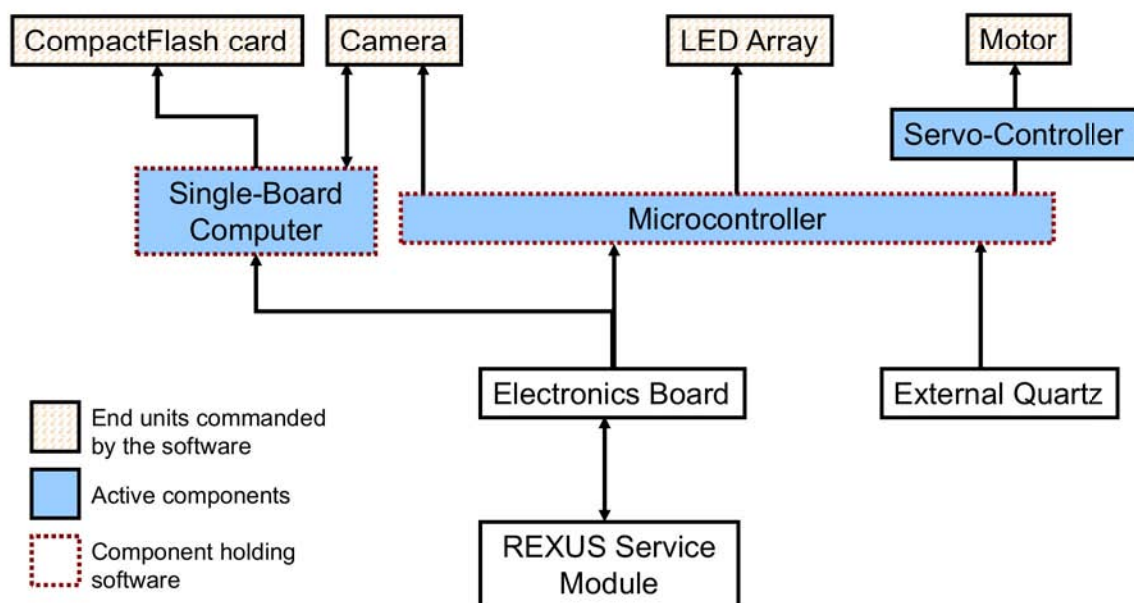


Figure 2.10: Diagram of the SPACE communication concept. The components holding software are indicated by a purple dotted frame and the components controlled by the software are indicated by striped boxes.

2.2.6 Fullfilling requirements

Table 2.6 lists the requirements described in Section 2.1 and their implementation in the experiment set-up. All requirements on the hardware could be fulfilled.

Table 2.6: SPACE set-up requirement fulfillment.

Experiment requirement	Set-up implementation
Experiment objectives	
- generate dust collisions	shaking mechanism
- vacuum conditions	vacuum chamber and late evacuation
- observe dust collisions	camera
- record video data	data acquisition and storage system
Size	∅355.6 mm×220 mm inside the experiment module
Mass	<15 kg
Autonomy	Electronics board and computer
Rocket interfaces	
- power consumption	<28 W
- thermal	highest component temperature <60 °C
- vacuum	umbilical for late evacuation
Launch site conditions	
- temperature	hardware tested for operation from -40 °C to + 70 °C (Annex C.2)
- durability	hardware tested for many power cycles (without dust aggregates in the experiment cells, Annex C.7)
Flight conditions	
- acceleration loads	hardware tested for operation from 0g to 30g (Annex C.6)
- vibration loads	hardware tested for operation in the vibration range of a REXUS flight (Annex C.6)
- temperature loads	hardware tested for operation from -40 °C to + 70 °C (Annex C.2)
Landing conditions	hardware tested for operation from 0g to 30g (Annex C.6) experiment power off at LO + 300 s

3 Experiment runs

This section describes the different experiment runs and the performance of the SPACE set-up at the drop tower Bremen and on the suborbital rocket flight.

3.1 Experiments at the drop tower Bremen

From the 15th to the 19th of August 2011, a preliminary version of the SPACE experiment was tested during the third MEDEA campaign at the drop tower in Bremen (Weidling et al. 2012). This drop tower of 146 m height offers 4.74 s of microgravity time when dropping an experiment capsule and up to 9.3 s when using the catapult . Disturbances to the microgravity quality are lower than $10^{-6}g$, g being the Earth’s gravitational acceleration.

During this campaign, mainly mechanical parts of the experiment were tested, such as the glass cells, the shaking mechanism and the LED array (see Section 2.2 for details). In addition to validating some of the experiment hardware, the drop tower campaign also delivered valuable scientific data. Indeed, the four experiment cells were filled with several samples of SiO₂ dust (see Section 4.4.1 for details) and aggregate collisions and agglomeration under microgravity conditions were observed. In total, the SPACE experiment flew five times.

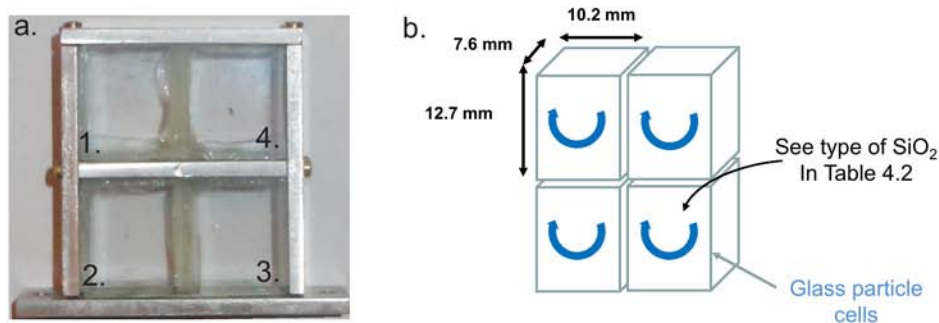


Figure 3.1: Particle glass cells in the drop tower configuration: a. picture of the glass cells (numbered from 1 to 4), b. scheme of the four glass cells with their dimensions and circular motion indicated.

3.1.1 Drop tower experiment set-up

During the experiments at the Bremen drop tower, the hardware still was in development and therefore the experiment set-up was a preliminary version of the experiment design. The first difference to the suborbital flight set-up was that drop tower experiments did not require any autonomy. The complete data recording and storage was provided with the drop tower capsule. The camera used was a Photron Fastcam MC2 producing 8-bit grayscale frames and recording at a resolution of 512×512 px and a rate of 500 fps.

The second difference was that the drop tower set-up had four glass experiment cells (instead of three for the rocket flight) with the identical dimensions of $10.2 \times 7.6 \times 12.7$ mm³ (see Figure 3.1). The glass used was common soda lime glass cut out of microscope slides, which had been anti-adhesively coated by the Fraunhofer Institute for Surface Engineering and Thin Films of Braunschweig (see Section 2.2.1).

The rest of the drop-tower hardware was identical to the rocket flight set-up.

3.1.2 Drop tower shaking profile

The shaking frequencies at each second of each experiment are listed in Table 3.1. The first few seconds were used for de-agglomerating clusters that formed during the experiment preparation and the capsule launch. They ranged from 10.5 Hz to 16.7 Hz. This fast shaking phase was followed by a slower shaking phase, with shaking frequencies from 3 Hz to 6 Hz, allowing for low velocity collisions and cluster formation (see Section 6.1.1).

Table 3.1: Shaking frequencies during each drop tower experiment run (in Hz). During drop 4, a glass chip blocked the shaking mechanism.

Drop	Flight time [s]								
	1	2	3	4	5	6	7	8	9
	Shaking frequency [Hz]								
1	16.7	16.7	8.4	8.4	4.5	4.5	4.5	4.5	4.5
2	16.7	16.7	16.7	16.7/5	5	5	5	5	5
3	10.5	10.5	10.5	3	3	3	3	3	3
4	0	0	0	0	0	0	0	0	0
5	15.5	15.5	15.5	6	6	6	6	6	6

3.1.3 Experiment performance

The technical outcome of this hardware test was that the design of the vacuum chamber inner components, comprising the glass cells, shaking mechanism and LED array could be validated. Except for the first drop, all experiment components behaved nominally and withstood the drop tower acceleration loads. During drop 1, the bottom left screw holding the experiment cell frame to the shaking mechanism broke and the cells detached from the shaking mechanism. For the flight on the suborbital rocket, bigger screws were used for holding the cell frame.

In addition, the use of common glass for the experiment cells had to be reconsidered. During the cell handling before and during the experiment run itself, tensions and loads induced severe cracking and the generation of glass chips (see Figure C.6). During drop 4, one of these chips jammed the cog wheels of the shaking mechanism and the experiment cells could not rotate. For the flight on the suborbital rocket, it was decided to use the more resistant technical glass Borofloat33. It was also noted that enhanced caution had to be applied when handling the coated glass components, as this coating was very delicate and got damaged while handling for the first time.

3.1.4 Scientific data

Drop 1 and 4 did not deliver any scientific data due to the hardware issues described previously. During the three remaining drops, the formation of clusters of sizes up to 5 mm could be observed in some of the cells. These clusters formed free-flying inside of the experiment cell volume. Some examples of clusters observed in the SPACE drop tower experiments can be seen in Figure 3.2.

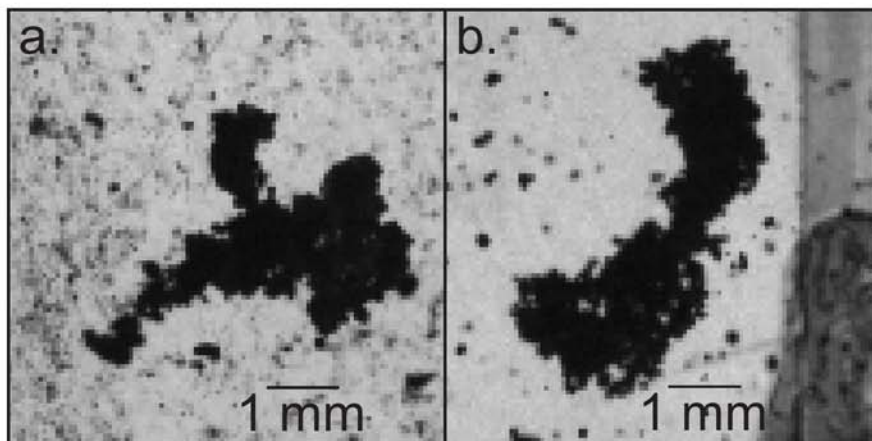


Figure 3.2: Examples of clusters formed during the SPACE drop tower experiments: a. cluster formed in cell 1 after 7.9 s of drop 5 (aggregates composed of spherical polydisperse SiO_2 , see Table 4.2). b. cluster formed in cell 2 after 8.5 s of drop 5 (aggregates composed of monodisperse SiO_2 , see Table 4.2).

3.2 Experiment run on the REXUS 12 rocket

On the 12th of March, 2012, at 13:00 Kiruna time, REXUS 12 was launched from Esrange near Kiruna, Sweden, carrying the SPACE experiment on-board. This section describes the suborbital flight and the experiment in-flight performance.

3.2.1 Rocket flight data

REXUS 12 was carrying 4 experiments on-board, including one under the nosecone (see Figure 2.1). In addition to the payload stage, the rocket consisted of an improved Orion motor, a Recovery Module and a Service Module. The Recovery Module held the secondary and primary parachutes for payload deceleration and landing, along with their release mechanism and a GPS beacon for payload localization and recovery. The Service Module was responsible for providing the experiments with power and signals and guaranteed telemetry and telecommand communications. In total, REXUS 12 had a weight of 542 kg.

Figure 3.4 and Table 3.2 are showing the REXUS 12 and SPACE events during the flight. 21 s after lift-off, the motor burnt out shortly after which it separated from the payload. The Yo-yo mechanism, which consisted of two masses on strings, was released and reduced the rocket's rotation rate from 3-4 Hz to about 0.03 Hz. The trajectory apogee was reached at 82 km in altitude. The reduced gravity phase lasted about 150 s starting with the motor separation, which was the last event inducing strong acceleration perturbances. In order to match the longest and slowest shaking phase of the experiment with the trajectory apogee, where the better microgravity quality was expected, the SOE signal was set to 65 s after lift-off. Subsequently, the data recording was planned to start at 75 s after lift-off. The motor shaking start was set to 30 s after the reception of SOE (95 s after lift-off).

The roll, pitch and yaw accelerations measured by the REXUS Service Module during the flight are plotted in Figure 3.3. The maximum loads the payload hardware was subjected to were reached during launch with about 17g along the roll axis, g being the Earth's gravitational acceleration. Re-entry loads did not exceed 6g.

3.2.2 Flight shaking profile

During the suborbital flight, the microgravity time available was about 15 times longer than during an experiment at the drop tower. The shaking profile applied to the experiment cells had to be adapted accordingly. Moreover, because of the microgravity disturbances described in Section 5.6.1, it was decided to shake the dust cells along two directions in a circular motion (see Section 2.2.1).

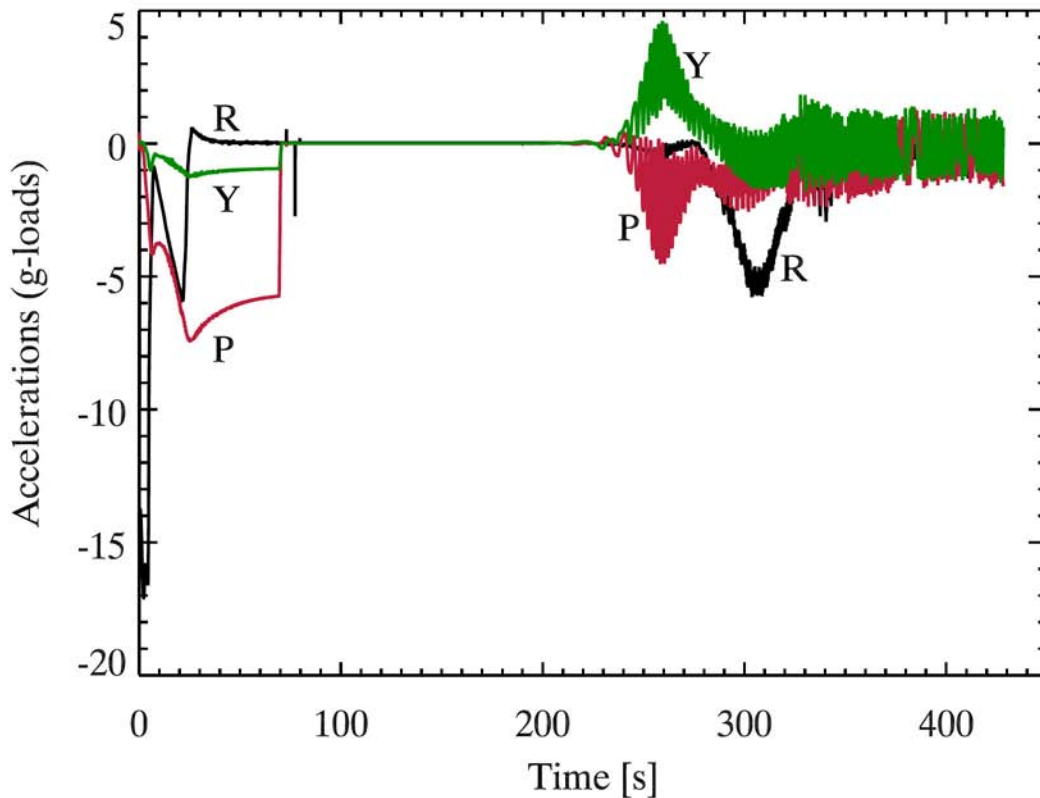


Figure 3.3: Measured REXUS 12 accelerations: on the roll (black, quoted "R"), pitch (red, quoted "P") and yaw (green, quoted "Y") axis. The acceleration is given in units of g, the Earth's gravitational acceleration. The telemetry loss between 120 and 180 s (also seen in Figure 3.4) is indicated by a blue dashed line.

The shaking profile at which the containers were agitated included three cycles, each composed of a shaking period of 5 to 10 s and a longer slow shaking period of 15 to 25 s with transition ramps between them (see Figure 3.5 and Table 3.3). This shaking profile was conceived to submit the aggregate systems to three agglomeration phases and three fragmentation phases. Agglomeration took place when the container rotation speed was ramping down. As the cell walls rotated slower, the relative velocities between aggregates decreased and the sticking probability between them increased, leading to cluster growth. In the opposite way, ramping up the shaking frequency led to higher collision energies and cluster disruption. The slowest and longest shaking phase was scheduled around the apogee of the rocket trajectory, when the quality of the microgravity was at its best (i.e. the residual accelerations were minimal).

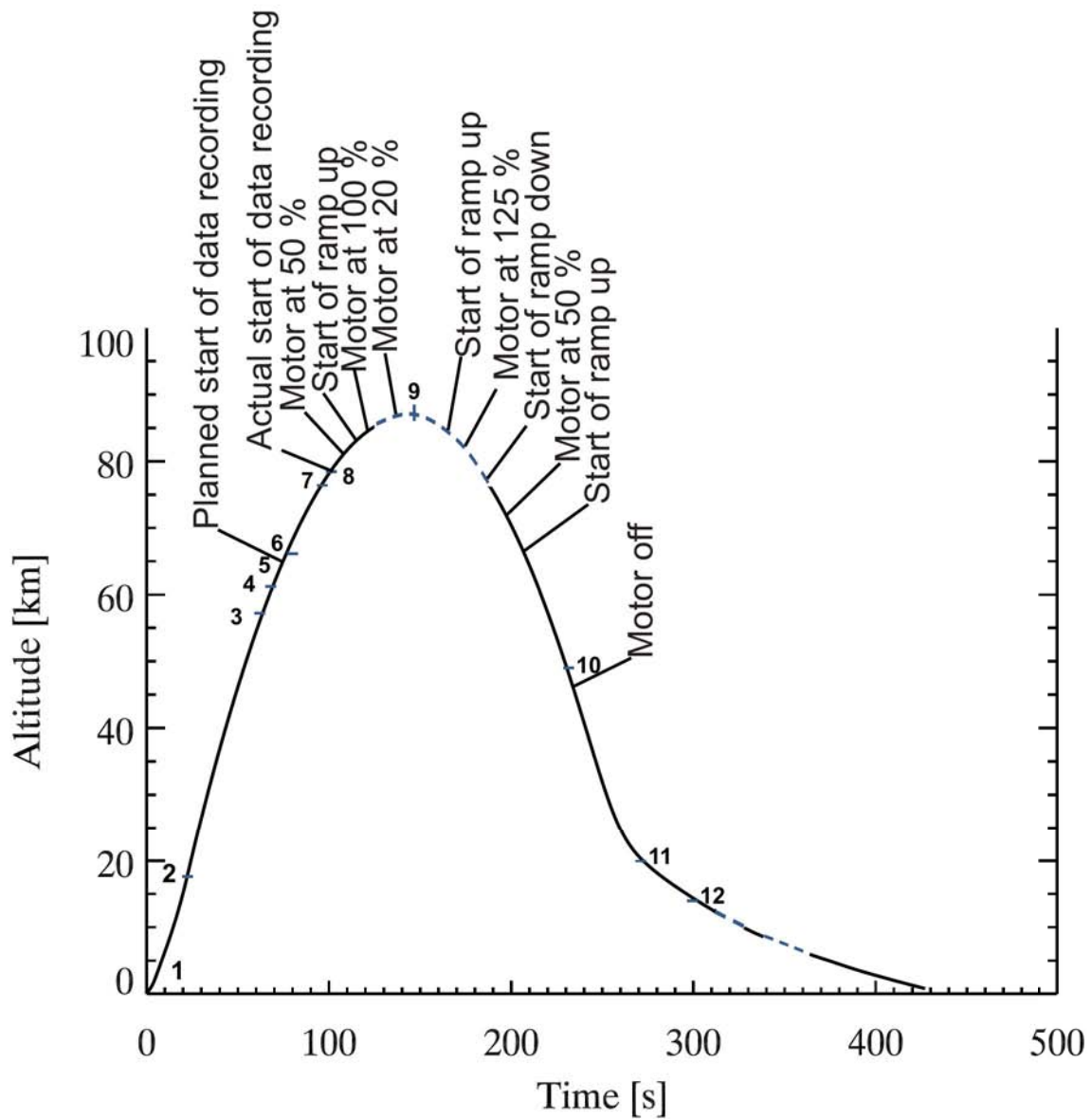


Figure 3.4: Measured REXUS 12 flight altitude according to the flight time. Three data drop-outs happened at around 150 s, 320 s and 350 s. The dashed line around apogee marks the interpolation of the flight parabola. The numbers represent REXUS flight events and are explained in Table 3.2. The actual start of data recording and the motor profile of the SPACE experiment are also indicated. In this graph, the time count starts at rocket lift-off.

Table 3.2: REXUS and SPACE countdown and flight events. LO stands for lift-off.

Number in Figure 3.4	REXUS Event	SPACE Event	Flight Time
	Experiments power on	Main power on: the on-board, computer, flash card and electronics board are powered.	LO - 600 s
	REXUS Service Module switch to battery power	End of SPACE vacuum chamber evacuation	LO - 120 s
1	Liftoff: LO signal to all experiments	SPACE enters the flight mode	LO + 0 s
2	Motor Burn-Out		LO + 21 s
3	SPACE SOE signal	The microcontroller switches on the LED array and camera and motor	LO + 65 s
4	Yo-Yo despin		LO + 70 s
5	Nosecone ejection		LO + 74 s
6	Payload/motor separation		LO + 77 s
7		The microcontroller starts the shaking sequence of the motor (see Figure 3.5)	LO + 95 s
8		Measured start of video data recording	LO + 102 s
9	Apogee		LO + 144 s
10		End of the shaking sequence. Motor, camera and LED array are switched off.	LO + 245 s
11	Start of re-entry		LO + 270 s
12	SPACE power off	All experiment components are off	LO + 300 s
	Planned parachute release		LO + 420 s
	Planned landing of payload		LO + 640 s

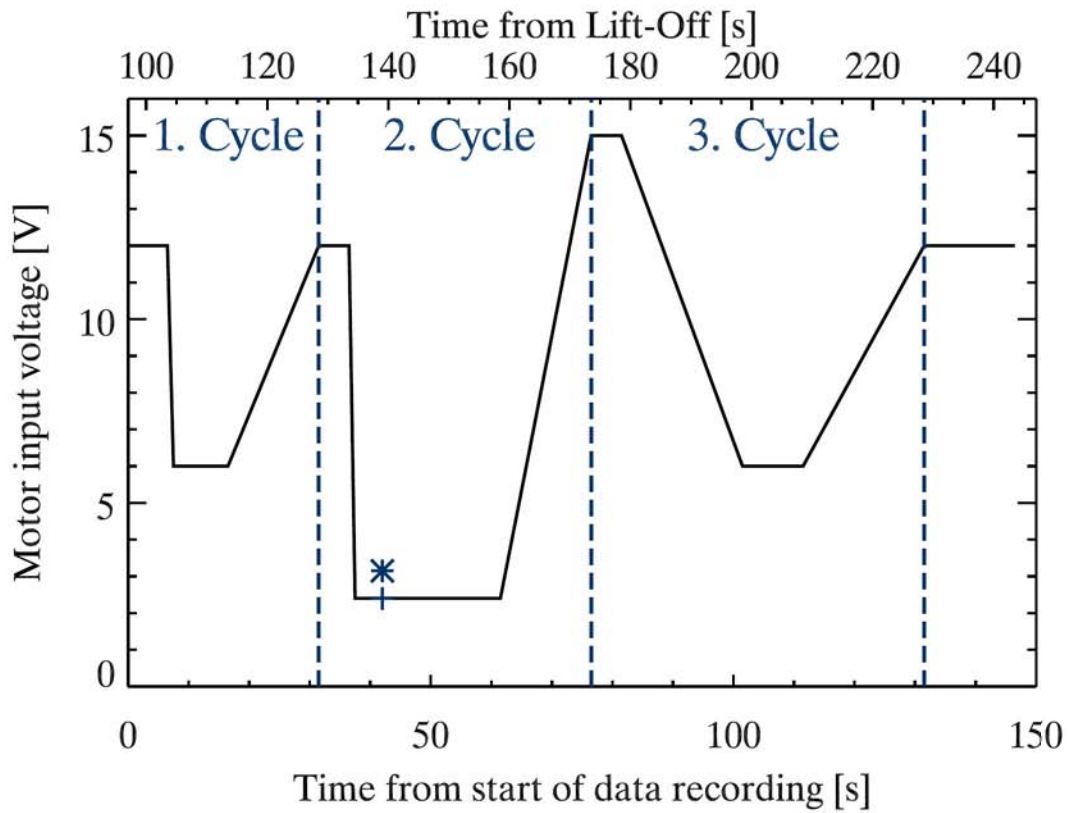


Figure 3.5: Input voltage of the SPACE motor according to the flight timeline. The times indicated originate at the start of data recording (bottom axis) and at rocket lift-off (top axis). The three cycles composed of a growth and a fragmentation phase are specified. Apogee was reached 144 s after lift-off and is indicated by an asterisk.

Table 3.3: Delimitations of the growth and fragmentation phases used for the data analysis. The origin of the times is the first recorded frame 97 s after rocket lift-off. The three cycles can be seen on Figure 3.5.

Phase	Cycle	Start time (s)	End time (s)
Growth	1	6	15
	2	35	46
	3	85	102
Fragmentation	1	17	32
	2	62	76
	3	112	132

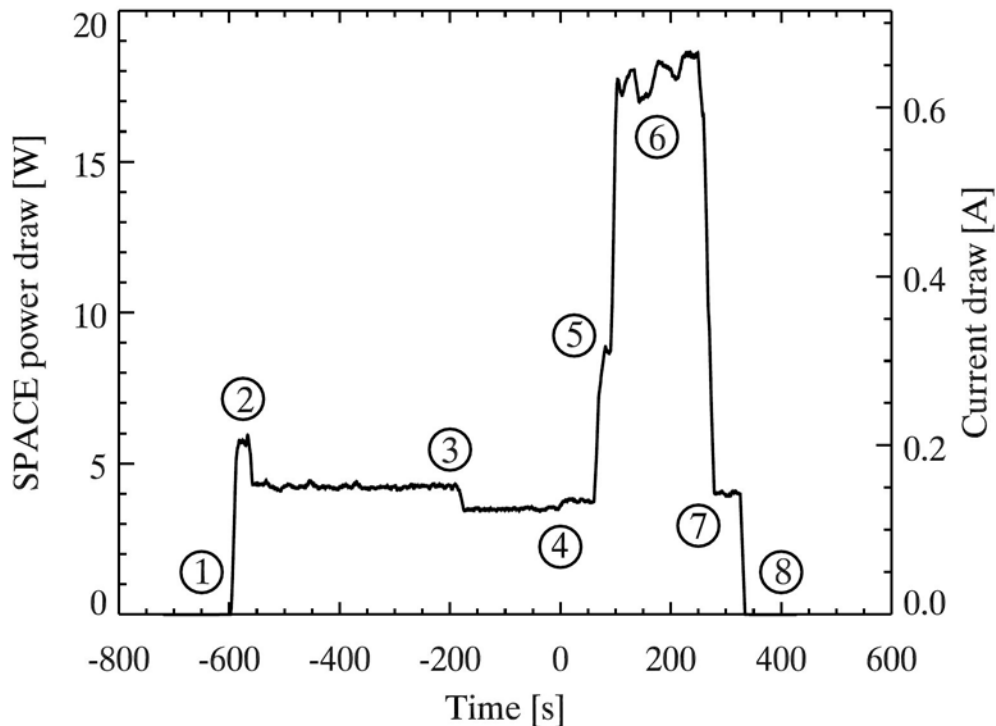


Figure 3.6: SPACE experiment power draw during the REXUS 12 flight. The origin of the times is at lift-off. The following events can be identified: 1. experiment switch on, 2. on-board computer booting, 3. switch to the REXUS 12 Service Module batteries, 4. lift-off, 5. switch on of the experiment camera and LED array, 6. run of the shaking sequence, 7. switch off of the motor, camera, LED array and pressure sensor and 8. experiment shut-down by the Service Module.

3.2.3 Experiment flight performance

During the REXUS 12 flight, the experiment health and status telemetry received at the SPACE ground station displayed a nominal functioning of the experiment. The power consumption records made by the REXUS Service Module during flight can be seen in Figure 3.6. 600 s before launch, the experiment was powered on and the on-board computer booted with a peak consumption of 6 W (0.21 A at 28 V). During the countdown before launch, the computer and electronics had a nominal consumption of 3.5 W. At 65 s after lift-off, the experiment switched on the camera and the LED array, increasing its power consumption to 8.9 W shortly after which the motor was switched on. The maximum power consumption of about 18 W (0.64 A at 28 V) was reached between 100 s and 250 s after lift-off while all components were on and the computer was recording data at maximum capacity.

The computer data log also confirmed the nominal functioning of the experiment hardware. In addition, the microcontroller memory, which was recovered intact, confirmed the nominal functioning of the vacuum system. Figure 3.7 shows the pressure readings recorded during the flight and confirms that the air pressure inside the vacuum chamber remained below 8.7×10^{-5} mbar during the experiment.

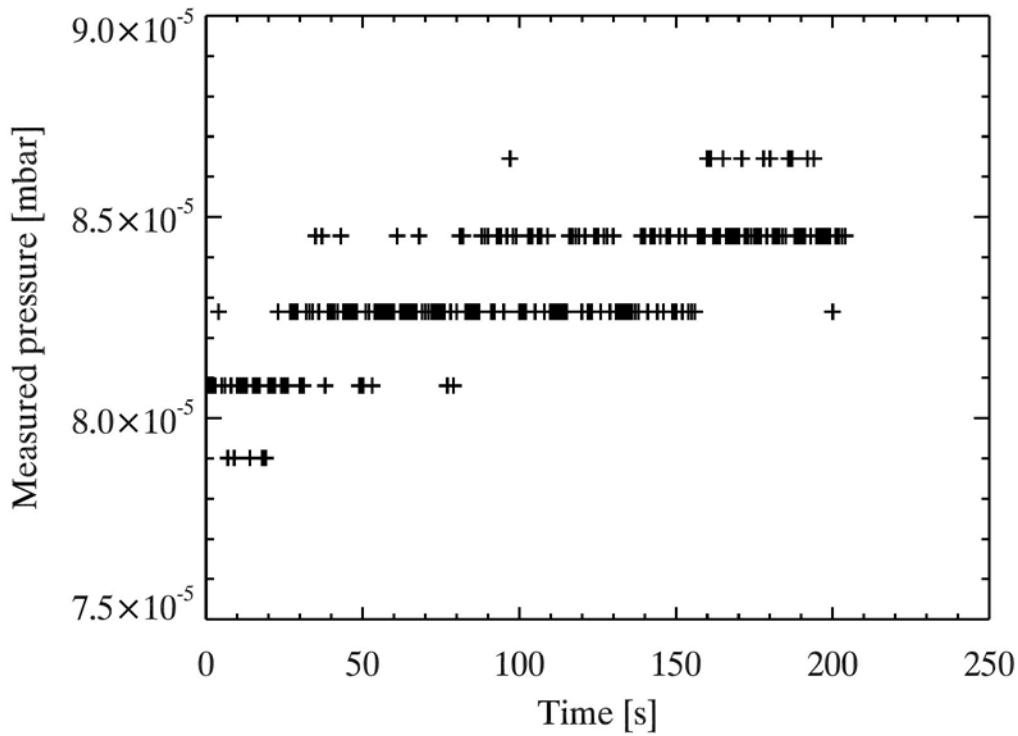


Figure 3.7: Pressure measured inside the SPACE vacuum chamber during the REXUS 12 flight. The time origin is at rocket lift-off. The pressure sensor was switched off at LO + 200 s

The frame streaming logs revealed a certain number of missing frames between the first 5 and 15 s of the recording time: the streaming randomly lost a couple of frames, never more than 5 in a row, on an irregular pattern. This "hick-up" of the data recording system was a known behavior and had been observed on ground during hardware tests. Its origin could not be determined with certainty, but seemed to lie in the "warming up" of the on-board computer processor. The option of starting the data recording earlier in the flight timeline was avoided, since it implied all experiment components to be on and functioning at their maximum capacities during the high acceleration phases of the launch. As the amount of lost frames was very low compared to the total amount recorded, and as the frame loss always stopped after the first 10 s of the recording flight, this behavior was evaluated acceptable and did indeed not influence the later data analysis.

One discrepancy with ground test behavior was detected in the starting time of the camera streaming. On all ground tests (including temperature tests), the camera required about 10 s between receiving power and starting frame acquisition. During the REXUS flight, however, 31.65 s separated the camera powering and the time of the first frame. In the experiment sequence design, 30 s buffer time were implemented between the expected time of the first recorded frame and the start of the particle shaking (which marks the start of the actual experiment run). That is why the non-recorded time of the shaking sequence only lasted 1.65 s.

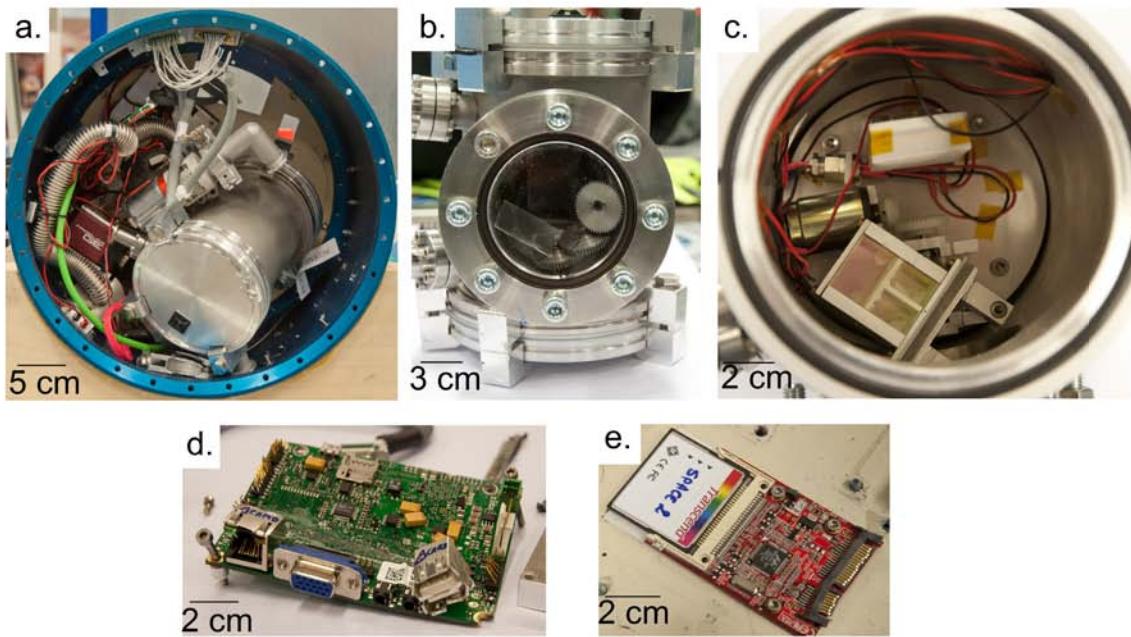


Figure 3.8: SPACE hardware after payload recovery: a. top view of the complete experiment module, b. front view of the vacuum chamber inner volume through the chamber view port, c. top view of the vacuum chamber inner volume, d. on-board computer baseboard, e. CompactFlash memory card with S-ATA adapter. Image credits: D. Heißelmann.

3.2.4 Recovery

At lift-off + 420 s, the drag parachute was supposed to be released, pulling with it the main parachute which should have substantially decreased the fall velocity of the payload stage. A nominal ground impact velocity for a REXUS flight would usually be around 10 m s^{-1} (see the Rexus Manual, Eurolaunch 2010). During the REXUS 12 flight, however, the release of the secondary parachute did not trigger and the payload impacted ground with a much higher velocity. The rocket hit an open space covered with about a meter of snow, which damped the crash. The impact loads were still much higher than expected, and, moreover, the strongest loads were not along the rocket roll axis but along an oblique axis, due to free tumbling of the payload during re-entry.

Furthermore, the GPS beacon leading the recovery helicopter to the payload never started emitting, as it is usually triggered by the release of the drag parachute. Hence, a recovery was solely based on the good eyes of the helicopter team searching a calculated impact area. Fortunately, despite being entirely covered in snow, the payload could be retrieved. The outer skin of the rocket was undamaged. However, lots of the inner experiment hardware had been broken by the crash. In the case of the SPACE experiment, most of the components were destroyed. Figure 3.8 shows a few pictures taken while unmounting the experiment after recovery. There were exactly two hardware components that remained undamaged: the electronic board and the memory card. Therefore a recovery of the scientific data was possible.

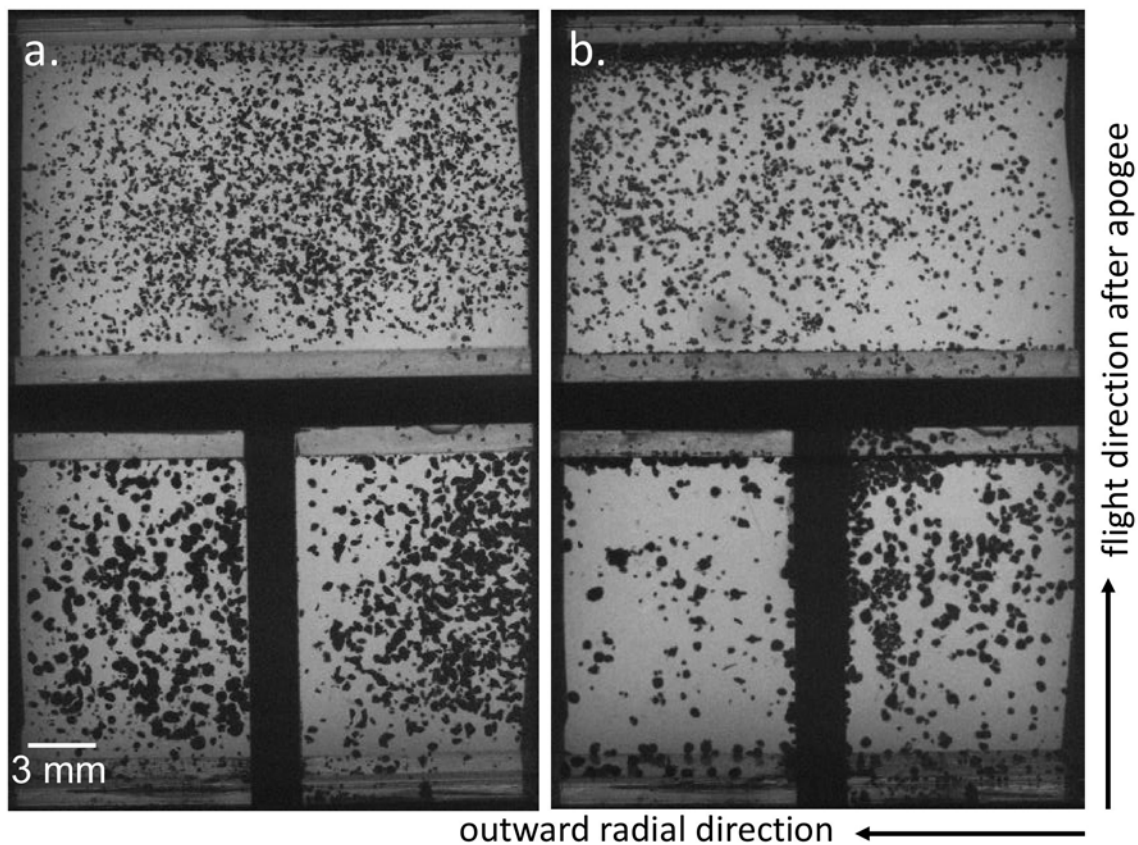


Figure 3.9: Two 8-bit grayscale frames recorded during the SPACE experiment run: a. at the very beginning of the experiment (1 s after start of data recording), when all the dust aggregates were free-flying, b. during a slow shaking phase of the experiment run (50 s after start of data recording). During slow shaking phases, aggregates preferentially accumulated in the cells' left upper corner due to microgravity disturbances (see Section 5.6.1 for details). The rocket flight and outward radial directions are indicated.

3.2.5 Scientific data

The scientific data recorded revealed an unexpected behavior of the dust aggregates: during slow shaking phases, instead of agglomerating inside the experiment cell volume, the dust aggregates formed agglomerates on the cell glass walls. This could be easily identified as dust sticking to the glass walls rotated with the container, whereas free-floating particles had linear trajectories. During the slowest and longest shaking phase (see Section 3.2.2 and Figure 3.4), collisions with the glass very quickly depleted the number of aggregates in the inner cell volume. Thus, no free-flying collisions could be observed. This constituted a major difference to other dust collision microgravity experiments, such as the SPACE experiment at the drop tower Bremen, or the experiments performed by Weidling et al. (2012) and Kothe et al. (2013). During most of the other shaking phases of the experiment run, however, particles were free-flying in the cell volume and collision properties of the dust aggregates could be analyzed (see Section 5).

4 Dust samples

This section describes the dust analog material investigated with the SPACE experiment set-up. For both, the drop tower and the rocket flight experiments, SiO₂ aggregates of different types and sizes were used.

In the following, single dust aggregates introduced into the experiment glass cells before the beginning of the experiment ($\sim 100 \mu\text{m}$ in size) will be referred to as *aggregates* or equivalently *monomer aggregates*. Indeed they are themselves aggregates of smaller dust *monomer particles* of mean sizes around $1 \mu\text{m}$ and acquired commercially. During the different SPACE experiments, several of these aggregates stuck together to form bigger agglomerates. These new structures will be referred to as *clusters*.

4.1 Choice of the dust analog material

The choice of silicates as sample material is relevant for several reasons. First, the spectral analysis of many young stellar objects such as T-Tauri and Herbig Ae/Be stars displays a $10 \mu\text{m}$ absorption feature indicating the presence of silicates in their circumstellar disks (see e.g. Bouwman et al. 2001, Sicilia-Aguilar et al. 2007, Sargent et al. 2009). Secondly, protoplanetary disk models and their associated dust condensation sequence predict the presence of numerous forms of silicates in the planet formation regions (Boss 1998, Henning & Meeus 2009). Finally, silicates are found in meteorites, which are remnants of the planet formation phase of the Solar System (see e.g. Scott 2007). These observations are indicating that silicates play an important role in the early stages of the formation of rocky bodies in disks around young stars and are, therefore, relevant for use in dust collision experiments like SPACE.

The dust material used to observe collisions in the SPACE experiments was chosen such as to be representative for materials thought to be found in the early Solar System, the so-called Solar Nebula, or in other observable protoplanetary disks. This supports the application of the coagulation and fragmentation properties observed during the experiments to dust collision behavior in these protoplanetary environments.

A commonly used dust analog material is silicate dioxide, SiO₂. Table 4.1 lists the relevant characteristics for the dust types investigated in this work (see also Blum et al. 2006b, for more details). SiO₂ was already used in several dust collision experiments aiming at the investigation of dust behavior in protoplanetary disks (see e.g. Blum & Wurm 2008,

Table 4.1: Properties of the dust types investigated with the SPACE experiment.

Dust type	Spherical Monodisperse	Spherical polydisperse	Irregular polydisperse
Figure	4.1c.	4.1b.	4.1a.
Manufacturer	Micromod	Admatechs (SO-E3)	Sigma-Aldrich
Monomer radius (μm)	$0.76 \pm 0.03^{(1)}$	0.8 to 1.2 ⁽³⁾	0.05 - 5 ⁽⁵⁾
Density (kg/m^3)	2000 ⁽¹⁾	2600 ⁽³⁾	2600 ⁽⁵⁾
Young's modulus (GPa)	54 ⁽²⁾	41 ⁽⁴⁾	41 ⁽⁴⁾
Poisson number	0.17 ⁽²⁾	0.17 ⁽⁴⁾	0.17 ⁽⁴⁾

⁽¹⁾ Blum et al. (2006b)

⁽²⁾ Seizinger et al. (2012)

⁽³⁾ manufacturer information Admatechs

⁽⁴⁾ Weidling et al. (2012)

⁽⁵⁾ manufacturer information Sigma-Aldrich GmbH

and references therein). More recently, Güttler et al. (2010), Weidling et al. (2012) and Kothe et al. (2013) performed related experiments in the laboratory, in the Bremen drop tower and on parabolic flights, investigating SiO₂ collisions of aggregates of different sizes and at different velocities. SiO₂ can be commercially acquired in several shapes and sizes. The species used in the SPACE experiment was produced by Admatechs, Sigma-Aldrich and Micromod (see Table 4.1). Monodisperse dust is composed of same-sized spherical monomer particles. Polydisperse dust has a monomer particle size distribution. The monomers can be spheres or irregularly shaped particles. In the following, these polydisperse dust types will be called *spherical* and *irregular* polydisperse dust, respectively. For SiO₂ acquired by Sigma-Aldrich, this size distribution was investigated in further details by Kothe et al. (2013). SEM images of these three sample materials can be seen in Figure 4.1. The investigation of monodisperse dust is interesting because it is easy to model in molecular dynamics or smooth particle hydrodynamics (SPH) simulations (see for example Wada et al. 2009, Güttler et al. 2009, Seizinger et al. 2012), and was already used in many other dust collision experiments. As its properties are best known, experiment and simulation results using monodisperse dust can be compared one to another. However, the dust in real astronomical environments is expected to be irregularly shaped, which makes experiments with polydisperse dust also relevant. Comparing the behavior of both types of particles has already revealed some interesting differences in sticking and collision properties (for example irregular SiC and diamond grains in Poppe et al. 2000a). This is why both types of dust, mono- and polydisperse SiO₂, were flown on the SPACE experiment.

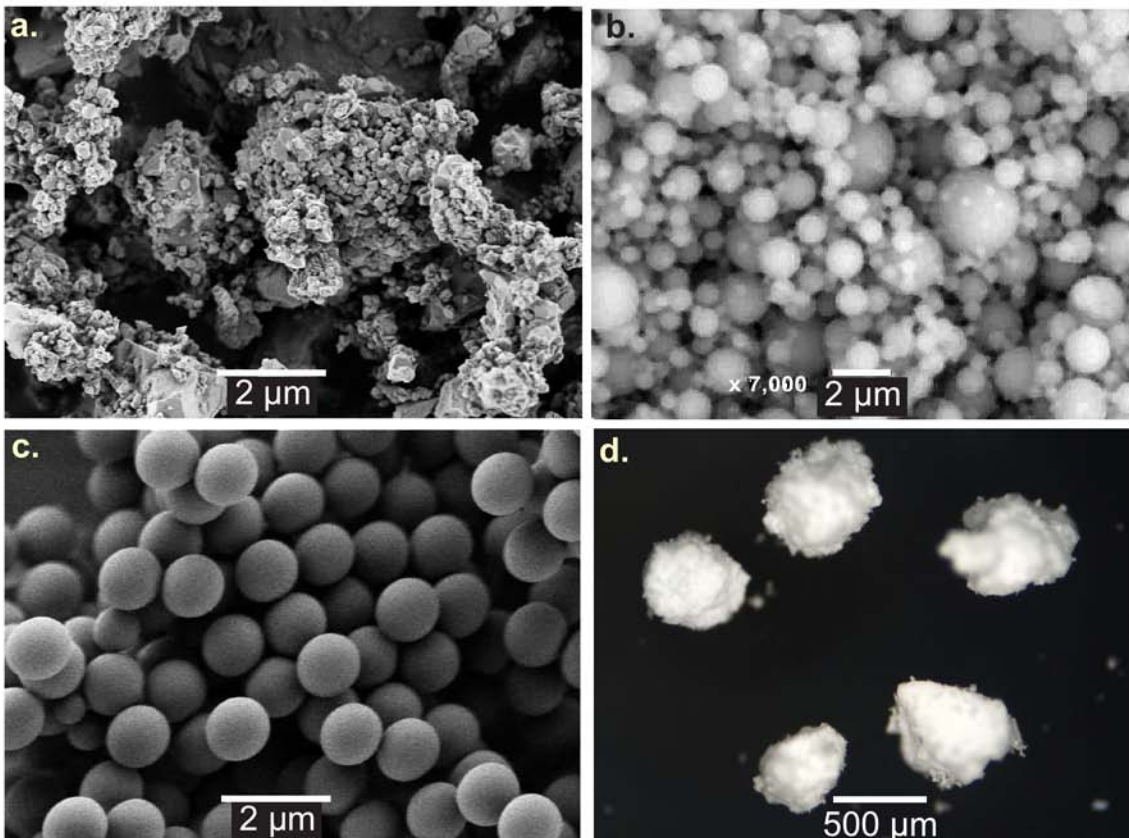


Figure 4.1: Dust analog SiO_2 used in the SPACE experiment: a. SEM picture of an aggregate composed of irregular polydisperse SiO_2 (Sigma-Aldrich). Image credit: E. Beitz b. SEM picture of an aggregate composed of spherical polydisperse SiO_2 (Admatechs). Image credit: N. Machii c. SEM picture of an aggregate composed of monodisperse SiO_2 (Micromod). Image credit: E. Beitz d. microscope picture of aggregates composed of irregular polydisperse SiO_2 , sieved between 250 and 500 μm .

4.2 Aggregate sizes

As described in Section 1.2, dust aggregates growing in a protoplanetary disk have relative velocities between each other induced by different thermodynamical (Brownian motion) and aerodynamical (settling to the midplane, gas drag and turbulences) processes. Depending on the aggregate sizes, collisions at these velocities do not always lead to sticking and growing anymore, but as the aggregates experience restructuring and compaction with increasing collision energies, their new properties lead to bouncing or fragmentation upon collision. It is still under discussion whether both of these collision outcomes are an obstacle to further aggregate growth or favor it (see Zsom et al. 2010, Windmark et al. 2012) and experiments in size and velocity ranges around the transition from sticking to bouncing can deliver crucial information on dust growth behavior as input to disk models and simulations.

The dust collision model developed by Güttler et al. (2010), which was improved by Kothe et al. (2013), aims at better characterizing the transitions between the sticking, bouncing and fragmentation regimes. Recent experiments by Weidling et al. (2012) and Kothe et al. (2013) have been investigating more specifically the transition between the

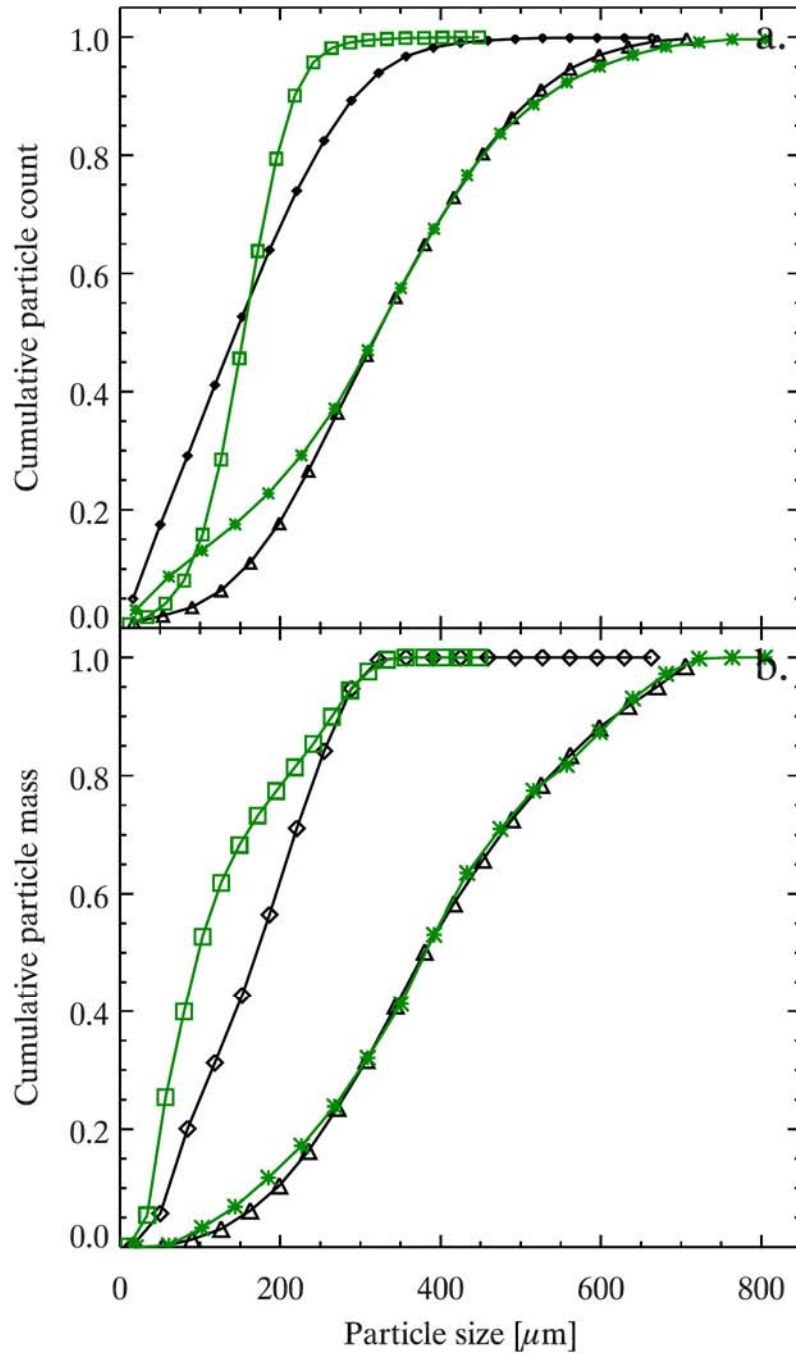


Figure 4.2: Size distributions a. by cumulative particle count (number of particles with a size smaller than the size indicated in the x-axis) and b. by cumulative mass (total mass of the particles smaller than the size indicated in the x-axis) of the different SiO_2 aggregates used in the SPACE experiment: aggregates sieved between 100 and 250 μm and composed of monodisperse (black diamonds) and spherical polydisperse dust (green squares) and aggregates sieved between 250 and 500 μm and composed of monodisperse (triangles) and spherical polydisperse dust (green asterisks).

sticking and bouncing regimes. Sub-mm- to cm-sized aggregates colliding at velocities between 1 and 10 cm s⁻¹ are precisely in this regime (see Figure 1.2). In this context, two sub-mm size distributions were chosen for the aggregates to be flown in the SPACE experiment: a smaller distribution between 100 and 250 μm and a bigger one, between 250 and 500 μm .

Aggregates composed of commercially acquired SiO₂ monomer grains actually coagulate inside of their storage container. To produce the two size distributions investigated in the SPACE experiment, these aggregates were sieved to the required sizes. The resulting size distributions were measured and can be seen in Figure 4.2. A microscope picture of a sample of sieved aggregates can be seen in Figure 4.1d.

4.3 Volume filling factor and inner structure of the aggregates

The volume filling factor of SiO₂ aggregates produced as described in Section 4.2 was investigated by Weidling et al. (2012) and Kothe et al. (2013). Weidling et al. (2012) determined a value for the volume filling factor by accurately measuring the volume and mass of aggregates composed of polydisperse SiO₂, with sizes between 500 and 4000 μm with a material density $\rho = 2600 \text{ kg/m}^3$ for polydisperse SiO₂. They found a value of $\phi = 0.35 \pm 0.05$. Kothe et al. (2013) analyzed nano-CT images of sieved monodisperse SiO₂ aggregates at sizes around 100 μm and determined a value of $\phi = 0.37^{+0.06}_{-0.05}$. These two values are relatively close together. For the sub-mm-sized aggregates investigated in this work, identical in size and preparation to the ones used by Kothe et al. (2013), a volume filling factor of $\phi = 0.37$ was assumed.

In addition, Kothe et al. (2013) examined the inner structure of such dust aggregates. They observed a 100 μm -sized SiO₂ aggregate with a nano-CT microscope and showed that the inner volume filling factor of these aggregates is regular, displaying only a very slight compaction at the outer border of $\pm 5\%$ compared to the inner part of the aggregate. This result shows that the collision behavior of these aggregates is not influenced by their preparation method.

4.4 Allocation of the dust aggregates to the different experiments

4.4.1 Drop tower experiments

The SiO₂ aggregates prepared for the drop tower experiment runs were sieved into a size distribution between 100 and 250 μm and were distributed amongst the experiment cells as

Table 4.2: Details of the SiO₂ aggregate types and sizes observed during the five SPACE drop tower experiments. The asterisk (*) denotes spherical polydisperse dust manufactured by Admatechs (type SO-E3). The other polydisperse dust listed is irregular and manufactured by Sigma-Aldrich. As these experiments were performed with a preliminary version of the experiment hardware, not all cells were filled with dust aggregates and not all drops delivered useful experimental data. Data that was not relevant is marked by N/A. The agglomerate sizes are indicated with their standard deviation.

Drop	Cell	Dust type	Mean aggregate diameter [μm]	Quantity [mg]	Result type
1	1	polydisperse	118 \pm 88	13.2	N/A ⁽¹⁾
	2	polydisperse*	156 \pm 28	13.2	N/A ⁽¹⁾
	3	compacted monodisperse	118 \pm 88	17.1	N/A ⁽¹⁾
	4	monodisperse	118 \pm 88	17.1	N/A ⁽¹⁾
2	1	polydisperse	156 \pm 28	11.0	no agglomeration
	2	polydisperse*	156 \pm 28	11.0	monomer agglomeration
	3	monodisperse	118 \pm 88	14.3	cluster agglomeration
	4	N/A	N/A	N/A	N/A
3	1	N/A	N/A	N/A	N/A
	2	polydisperse	156 \pm 28	11.7	no agglomeration
	3	compacted monodisperse	118 \pm 88	6.8	cluster agglomeration
	4	N/A	N/A	N/A	N/A
4	1	N/A	N/A	N/A	N/A ⁽¹⁾
	2	polydisperse*	156 \pm 28	8.6	N/A ⁽¹⁾
	3	N/A	N/A	N/A	N/A ⁽¹⁾
	4	N/A	N/A	N/A	N/A ⁽¹⁾
5	1	polydisperse*	156 \pm 28	8.8	cluster agglomeration
	2	monodisperse	118 \pm 88	6.8	cluster agglomeration
	3	monodisperse	118 \pm 88	6.8	cluster agglomeration
	4	N/A	N/A	N/A	N/A

⁽¹⁾see Section 3.1.3

listed in Table 4.2. Four different types of aggregates were used. The first were aggregates of monodisperse dust, which is composed of same-sized spherical particles, manufactured by Micromod (Figure 4.1c.). The second were compacted aggregates of monodisperse dust. These aggregates were prepared like the ones mentioned above but in addition, they were shaken on a metal plate for 10 min at 10 Hz (plate shaking frequency). This leads to a compaction of the outer parts of the aggregates (see Weidling et al. 2009, for details). The third aggregate type were aggregates of polydisperse dust which is composed of irregularly shaped particles, manufactured by Sigma-Aldrich (Figure 4.1a.). Finally, the last aggregate type were SiO₂ aggregates of polydisperse dust which is composed of different-sized spheres, manufactured by Admatechs (type SO-E3) (Figure 4.1b.).

Table 4.3: Details of the SiO₂ aggregate types and sizes observed during the rocket flight experiment run. The polydisperse dust listed is irregular and manufactured by Sigma-Aldrich. The cells are identified as seen by the camera in experimental configuration (see Figure 2.4c.).

Cell	Dust type	Mean aggregate diameter [μm]	Quantity [mg]	Result type
Top	monodisperse	118 \pm 88	19.2	Cluster agglomeration on the cell walls ⁽¹⁾
Bottom left	monodisperse	320 \pm 90	15.3	Cluster agglomeration on the cell walls ⁽¹⁾
Bottom right	polydisperse	320 \pm 90	19.8	Cluster agglomeration on the cell walls ⁽¹⁾

⁽¹⁾see Section 3.2.5

4.4.2 Suborbital rocket flight experiment run

For the REXUS flight, the aggregates were sieved into size distributions between 100 and 250 μm and between 250 and 500 μm . Two types of SiO₂ aggregates were used: aggregates of monodisperse dust, manufactured by Micromod (Figure 4.1c.) and aggregates of polydisperse dust composed of irregular particles, manufactured by Sigma-Aldrich (Figure 4.1a.).

The dust samples were distributed into the experiment cells as listed in Table 4.3). From the three aggregate types used in the suborbital flight experiment run, the smaller aggregates composed of monodisperse dust were observed to grow fastest during the drop tower experiments (see Section 6.1.1). Therefore they were placed into the bigger top cell with the largest available volume.

5 Data analysis

This section describes how the video data gathered during the different SPACE experiments was analyzed. As mentioned in Section 4, single sieved particles inserted into the experiment cells will be named *aggregates* or equivalently *monomer aggregates*. These $\sim 100 \mu\text{m}$ *aggregates* are themselves composed of *monomer particles* of $\sim 1 \mu\text{m}$ in size. Agglomerates of aggregates building up during the experiments will be named *clusters*.

5.1 Drop tower scientific data

The SPACE experiment participated into a drop tower campaign with five catapulted drops (see Section 3.1). For each drop performed, the collision behavior of dust aggregates inside of four experiment cells was recorded. However, due to hardware issues, only drops 2, 3 and 5 delivered data that could be analyzed. For these three drops, Table 4.2 lists the agglomeration results in the experiment cells. This section describes the tools and methods used for the analysis of this data.

5.1.1 Aggregate and cluster collisions

For the experiments in which cluster agglomeration was observed (see Table 4.2), aggregates and clusters could be tracked individually. In this case, the collisions in the different experiments were analyzed with a semi-automatic tracking program also used by Güttler et al. (2010), Weidling et al. (2012) and Kothe et al. (2013). This program tracks the center-of-mass position of aggregates upon indication by the user and after frame binarization. For each user-detected collision, it computes the velocities of the colliding aggregates allowing for the determination of the collision velocity. In addition, the program tracks the cross section area of the aggregates on each two dimensional frame. As the aggregates rotate during the time they are tracked, they present different angles to the camera and, thus, different surface areas. The average of their visible surface over their tracking time is used to calculate their mass.

In the case of no observable or only monomer agglomeration, individual aggregates were too small and too numerous to be tracked.

As the cell glass of the preliminary version of the hardware used at the drop tower was an ordinary glass, it developed cracks during hardware assembly and the non-adhesive coating (see Section 2.2.1) underwent damages. These cracks and coating damages led to a non-uniform background illumination that could not be corrected properly, as it changed with time. However, the induced imperfections had only minor effects on the actual tracking of aggregates and clusters, as they were much smaller than the tracked aggregate.

5.1.2 Determination of the cluster fractal dimensions

The bigger clusters that grew during the drop tower experiments had a 3D fractal dimension of less than three. The exact dimension can be approximated using several 2D frames of each cluster, where it can be seen from different angles. For each frame, the 2D fractal dimension is determined using the box-counting method (Falconer 2003). In this method, a grid of varying mesh size is laid over a cluster with $\epsilon \times \epsilon$ boxes and, for each frame, the number $N(\epsilon)$ of grid boxes covered by the cluster is compared to the total number of boxes ϵ^2 . ϵ is increased progressively and the fractal dimension of the cluster projection on this frame, D_f , is deduced via

$$N(\epsilon) \propto \epsilon^{-D_f}. \quad (5.1)$$

To take the three-dimensionality of the cluster into account, D_f is then averaged over several frames. For a detailed description of this method applied to similar dust aggregates, see Kothe et al. (2013).

5.2 Dust growth during the suborbital flight

This section describes how the SPACE flight data can deliver information on dust aggregate properties and growth despite the fact that the observed clusters are growing on the glass walls of the experiment cell instead of free-flying in the inner cell volume, as they usually do in drop tower data.

5.2.1 Growing dust aggregates?

Before analyzing the aggregate growth behavior in the suborbital flight experiment, it has to be investigated if the dust clusters are indeed growing through dust-dust collisions instead of dust-glass collisions. In the latter case, the results would only deliver information about the interaction of the dust and glass and not the desired dust properties.

To investigate this, a series of Monte-Carlo simulations was performed, where particles were randomly deposited on a surface representing the cell glass wall. When colliding with the cell wall, the particles either encounter bare glass or another particle already sticking to the glass. The purpose of these simulations was to reproduce the aggregate deposition pattern seen on the SPACE experiment cells and to see whether the aggregates stuck directly to the glass or tended to form clusters through dust-dust collisions. The parameters that were varied between the simulations were the initial number of particles deposited on the glass surface, N_{sim} , and a glass sticking probability parameter, κ , defined as

$$\kappa = \frac{C_{\text{glass_stick}}}{C_{\text{glass}}}, \quad (5.2)$$

with $C_{\text{glass_stick}}$ being the number of collisions on bare glass that led to a deposition of the particle on the wall, and C_{glass} the total number of collisions on bare glass. This parameter accounts for the probability for a collision of an aggregate onto the bare glass to lead to aggregate deposition.

Before the simulation starts, no particles are on the surface. A number N_{sim} of particles are created with a size distribution similar to the size distribution of the dust aggregates inserted into the experiment cells. At each step of the simulation, one of the created N_{sim} particles collides with a randomly chosen location on the surface. A collision with the bare surface either leads to deposition according to the sticking probability κ or to bouncing back into the cell volume. In the latter case, the particle collides with the surface again, on a random new position. A collision with another particle already sticking to the surface always leads to deposition (the sticking probability between particles is considered to be 1). The simulation stops when all the N_{sim} particles are deposited.

As the frames recorded during the experiment had a resolution of $56.5 \mu\text{m}/\text{px}$, it was possible to simulate the particle growth on a one-to-one scale. The smaller sieved aggregates observed in the SPACE experiment had a mean size of $120 \mu\text{m}$ ranging from ~ 20 to $300 \mu\text{m}$ in diameter and the bigger aggregates had a mean size of $330 \mu\text{m}$ ranging from ~ 50 to $600 \mu\text{m}$ (see Figure 4.2). Hence, 1 to 25 pixel particles inserted into the simulation correspond to the size range of dust aggregates observed in the SPACE experiments. Simulation wall surfaces of $221 \times 362 \text{ px}$ and $192 \times 141 \text{ px}$ correspond to regions of interest inside the $15 \times 24 \text{ mm}^2$ and $15 \times 11 \text{ mm}^2$ visible surfaces of the larger and smaller experiment cells.

For the small monodisperse SiO_2 dust distribution, the real inserted number of aggregates was $N_{\text{exp}} \simeq 4000$. Thus, the initial number of particles created in the simulations was varied from 3000 to 5000 with a step size of 100 particles. For the larger distributions of aggregates composed of mono- and polydisperse, the real number of inserted aggregates was $N_{\text{exp}} \simeq 400$. Here, the initial number of particles was varied from 300 to 500 with a step size of 10. For both distributions the glass sticking parameter κ was varied from 0.0001 to 0.1 with a step size of 0.0001.

A few examples of the simulation results can be seen in Figures 5.1 and 5.2. For low glass sticking probabilities κ , only very few seeds deposited on the surface and clusters grow from there, leading to a few large clusters. For higher values of κ , many more particles deposit on the glass surface and the simulation results in a higher number of smaller clusters.

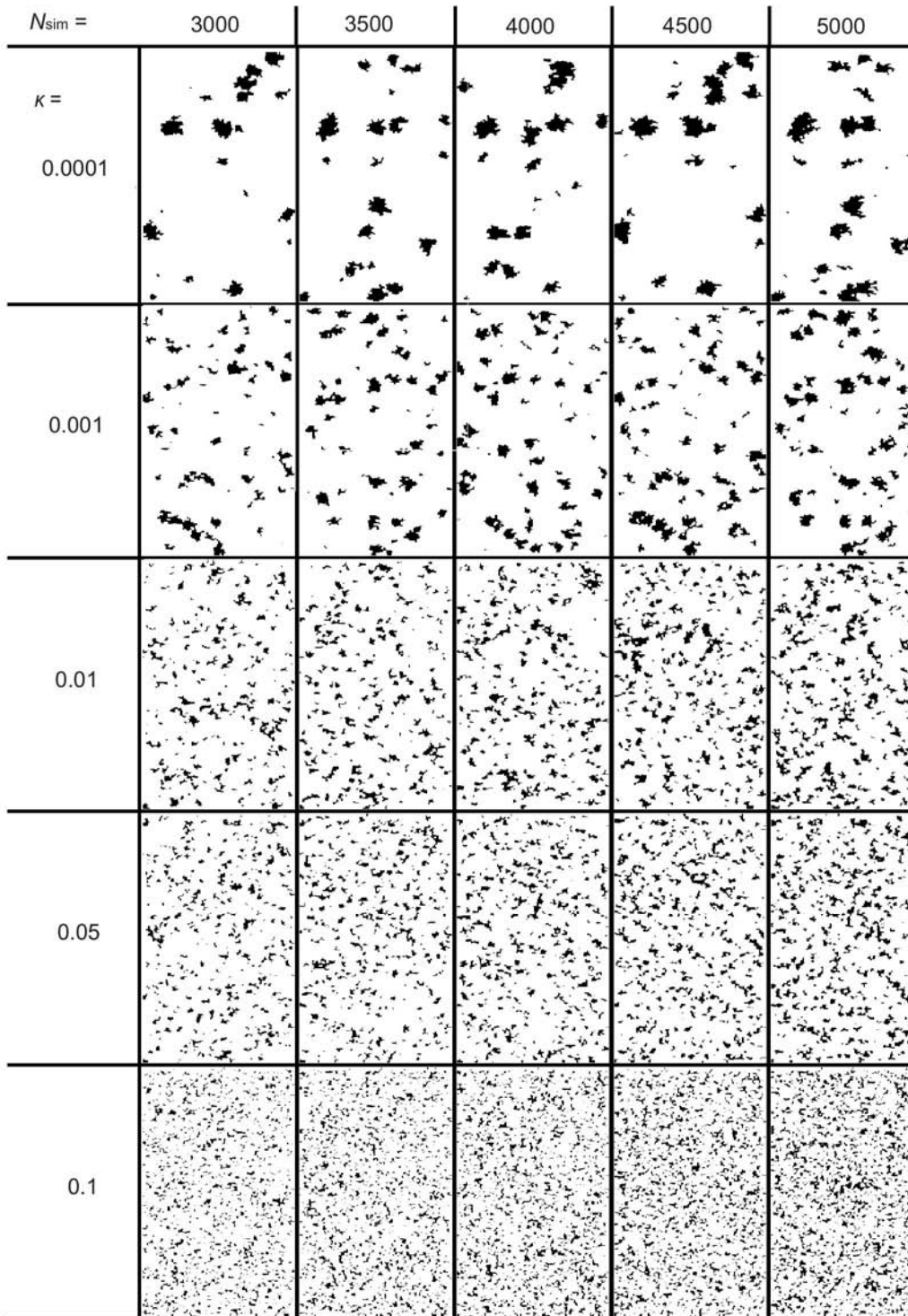


Figure 5.1: Monte-Carlo simulation results for the agglomeration of the small monodisperse dust size distribution used in the SPACE experiment rocket flight (mean size of $120 \mu\text{m}$). The simulation surface of 221×362 px represents a region of interest inside the bigger experiment cell. Each column has the same initial number of particles inserted into the simulation N_{sim} . Each row has the same glass sticking probability κ .

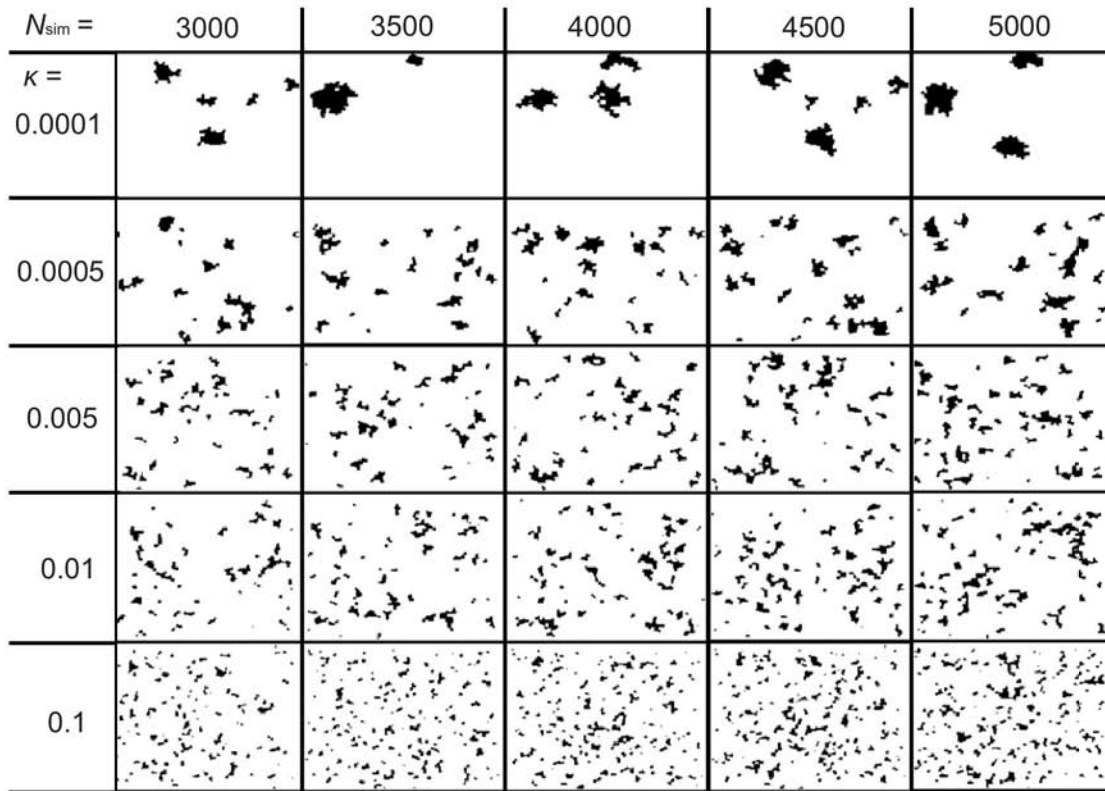


Figure 5.2: Monte-Carlo simulation results for the agglomeration of the large size distribution of aggregates composed of monodisperse dust used in the SPACE experiment rocket flight (mean size of $330 \mu\text{m}$). The simulation surface of 192×141 px represents a region of interest inside one of the smaller experiment cells. Each column has the same initial number of particles inserted into the simulation N_{sim} . Each row has the same glass sticking probability κ .

To quantitatively compare the results of the simulation with experimental data, a SPACE frame taken at 47 s after start of recording was used. This frame was recorded during a slow shaking phase (see Table 3.3), while all particles are incorporated in clusters and none are free-floating. This frame was binarized and the resulting number of clusters and their size distribution were determined. The root mean square of the bin by bin difference between this size distribution and the size distribution of the simulation result, σ_{dist} , was used as comparison criterium. To smooth out binarization effects on the size distribution of the data frame, the bin sizes were chosen at 4 px for the small and 9 px for the larger dust distribution. The simulations were run 5000 times for each set of parameters and the mean σ_{dist} determined. The best matches (minimum σ_{dist}) were found for $N_{sim} = 4600$ and 360 and $\kappa = 0.0055$ and 0.0045 for the smaller and larger aggregate distributions, respectively (Table 5.1). Figure 5.3 illustrates the best match between data and simulations for the smaller aggregate size distribution. The size distributions of 5000 simulation runs and of the chosen data frame are plotted in grey and in light red, respectively. It can be seen that the size distribution of the data frame lies within the size distribution range obtained for the simulations. As the number N_{sim} of inserted particles is in good agreement with the number of aggregates inserted into the SPACE experiment cells, glass sticking values around 0.5 % can be assumed. It can be concluded that it was not an enhanced glass

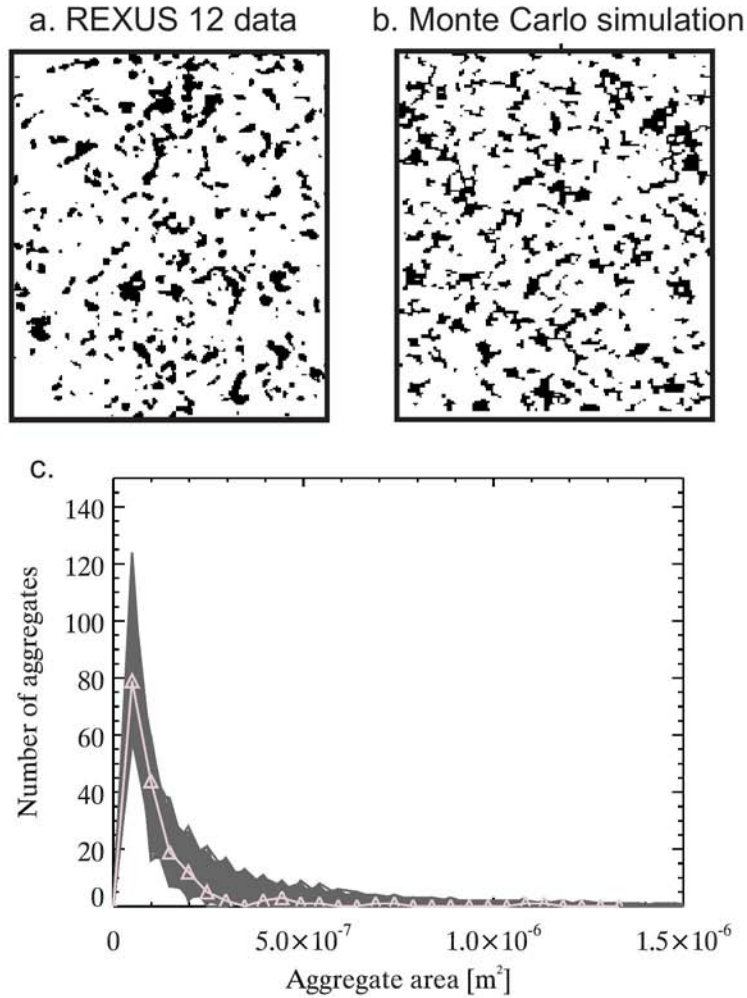


Figure 5.3: Results of a Monte-Carlo simulation for the smaller aggregate size distribution used in SPACE during the suborbital flight: a. binarized SPACE data frame at 47 s after start of data recording (region of interest at the center of the cell containing the smaller size distribution of aggregates composed of monodisperse dust). At this point of the experiment run, all dust aggregates are clustered on the cell wall. b. Monte-Carlo simulation depositing 4600 particles on a surface with a glass sticking parameter $\kappa = 0.0055$, c. size distribution of the data frame seen in a. (light red line, triangles) and 5000 runs of Monte Carlo simulations with the parameters of image b. (gray lines). The bin size for these distributions is 4 px ($1.23 \times 10^{-8} \text{ m}^2$).

Table 5.1: Monte-Carlo simulation results: the best match between simulation and data for both dust distributions are presented. N_{exp} and N_{sim} are the inserted numbers of aggregates into the experiment cell and into the simulation, respectively, κ is the glass sticking probability parameter and σ_{dist} the final size distribution difference which both are described in the text.

Aggregate distribution	N_{exp}	N_{sim}	κ	σ_{dist}
Small	4240	4600	0.0055	18.3
Large	375	360	0.0045	11

sticking efficiency that led to clusters on the cell walls but indeed the enhanced number of collisions of the aggregates on the glass, induced by residual accelerations during the rocket flight (see Section 5.6.1). This is also supported by the fact that the glass walls did not get dirty during the experiment run (see Section 5.4.3) despite the very high number of collisions.

It can also be concluded that dust clusters were not growing on the glass directly but on a few dust aggregates that deposited on the glass and served as seeds. Accordingly, clusters in the SPACE experiment grew by collisions between dust aggregates and the further data analysis will deliver information on the properties of these aggregates.

5.2.2 Growing on the wall?

The next question is whether or not the fact that the clusters grew on the cell glass walls, instead of free-flying in the cell volume, is a restriction to determining the collision properties of the dust. Indeed, compared to the mass of the considered aggregates, the mass of the cell wall can be considered as infinite, which could influence the collision parameters. The interesting collision parameters for the sticking and fragmentation events observed in the rocket flight experiment run are given by the Johnson-Kendall-Roberts (JKR) model of elastic collisions of spheres (Johnson et al. 1971). According to this model, the radius of the contact surface area between two colliding soft spheres is given by

$$a^3 = \frac{3R}{4E^*} (F + 3\gamma\pi R + \sqrt{6\gamma\pi R F + (3\gamma\pi R)^2}) , \quad (5.3)$$

$$\text{with } \begin{cases} \frac{1}{R} = \frac{1}{R_1} + \frac{1}{R_2} \\ \frac{1}{E^*} = \frac{1-\nu_1^2}{E_1} + \frac{1-\nu_2^2}{E_2} \end{cases}$$

where a is the contact surface radius, $R_{1/2}$, $\nu_{1/2}$ and $E_{1/2}$ are the radii, Poisson number and Young modulus of the two colliding spheres with indices 1 and 2, respectively, γ is their surface energy and F is the pressure force of one sphere on the other. This means that for an aggregate of mass m impacting another free-flying aggregate with the same composition properties but a different mass M , their relative velocity being v (case a. in Figure 5.4), their common sticking surface area will be determined by R , E^* , γ and F . If this is compared to the case where the target aggregate is sticking to a wall considered to have an infinite mass with respect to the mass m of the incoming aggregate (case b. in Figure 5.4), the parameters R , E^* and γ are approximately unchanged. This is a reasonable assumption if the upper part of the aggregate, where the impact takes place, is not affected by the lower part, where it sticks to the glass wall. Molecular dynamics numerical simulations of aggregates composed of a high number of monomer particles, e.g. in Wada et al. (2011), support such an approximation by showing (e.g. in their Figure 5) that aggregates are only locally affected by low-velocity collisions (under 2 m s^{-1} for their ice aggregates).

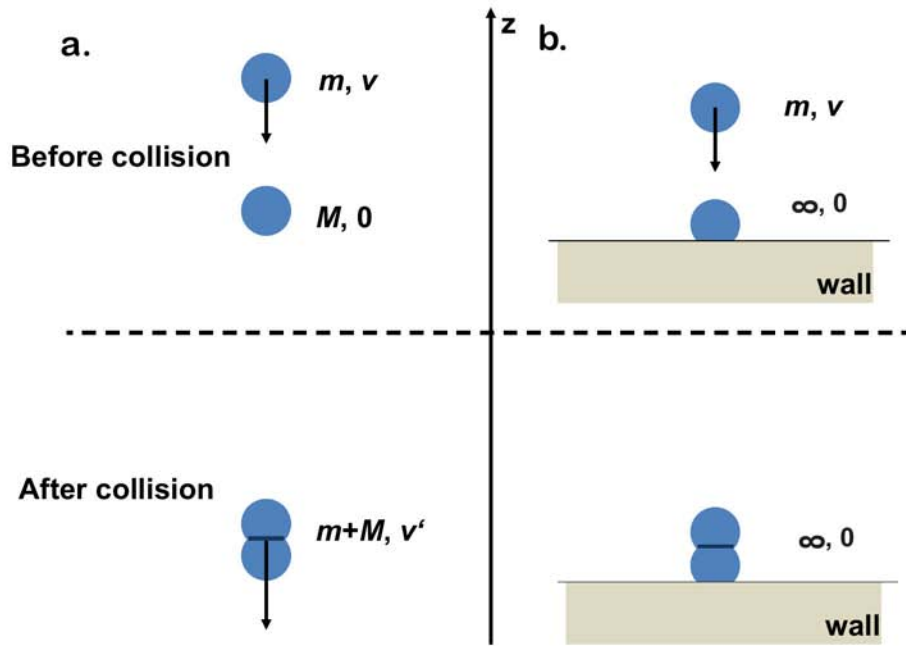


Figure 5.4: Scheme of an aggregate of mass m and velocity v colliding a. with an aggregate at rest of mass M and b. with an aggregate sticking to a wall of infinite mass.

As for the pressure force F of one aggregate on the other, it can be seen as the change in momentum of the impacting aggregate before and after the impact. This momentum variation can be compared for the two cases a. and b. in Figure 5.4. In case a. an aggregate of mass m impacts another free-flying aggregate of mass M with a relative velocity v . After a sticking collision, the resulting aggregate has a mass $m + M$ and a velocity $v' = \frac{m}{m+M}v$ (the collision is considered to be perfectly elastic). Hence, for the impacting aggregate

$$\Delta p = |p_{\text{final}} - p_{\text{initial}}| = |(m + M)v' - mv| = \mu v \quad (5.4)$$

with $\mu = \frac{1}{\frac{1}{m} + \frac{1}{M}}$ being the reduced mass of the system.

In the second case the target aggregate is considered to be already sticking on the wall (case b. in Figure 5.4). This aggregate has the same properties as before but, as now $M \gg m$, the reduced mass $\mu = m$ and $\Delta p = mv$. This value of Δp could also be obtained by two aggregates of the same mass m (implying $\mu = \frac{1}{2}m$) flying towards each other with the same velocity v (the relative velocity then would be $2v$). This means that the configuration of an aggregate sticking to a target aggregate on a wall (case b.) is equivalent to an aggregate sticking to another of the same mass and velocity, free-flying in the cell volume (case a.). Therefore, it is reasonable to consider clusters growing on the experiment cell walls as being equivalent to clusters growing inside the cell volume.

5.3 Suborbital flight data analysis

To study the multi-particle systems presented here and ensure the occurrence of observable collisions during the experiment run, a high number of aggregates was inserted into each experiment cell. This resulted in too high an optical depth in the cells to be able to study collisions individually. It was also impossible to measure their number and sizes directly. The flight data had to be analyzed in a statistical manner, by analyzing the interesting aggregate properties averaged over a high number of collisions.

A way of accessing the desired information was to average each image over a certain number of frames before and after it. Because the aggregates were constantly moving, the total surface of each aggregate was thus taken into account by contributing to the background grayscale. Furthermore, non-moving clusters growing on the glass wall became fully visible (see Figure 5.7c.).

5.3.1 Frame averaging

Each frame of the SPACE experiment was averaged over 201 frames (1.2 s) as follows:

$$\text{frame}_N = \frac{1}{201} \cdot \sum_{i=N-100}^{N+100} \text{frame}_i \quad \text{for } 100 < N < 27900 \quad (5.5)$$

An example of the frames obtained by this averaging can be seen in Figure 5.7c. The clusters on the glass walls are apparent as dark spots and can be monitored along the experiment. Furthermore, the background grayscale value of cluster-free parts of the frame delivers information on the quantity of dust aggregates that are free-flying at that moment: the darker the background, the more aggregates are free-flying, and the brighter the background, the more aggregates are incorporated in clusters on the cell walls.

5.3.2 Statistical analysis methods

The analysis of the frame background grayscale and of the clusters on the cell walls are in fact two distinct ways of retrieving information on the experiment aggregates. Figure 5.5 shows histograms of two data frames: in the left frame (a.), all of the dust aggregates present in the cell are free-flying. Its histogram (c., dashed red line) shows a rather diffuse distribution of medium-dark grayscale values: a uniform gray background. In the right frame (b.), however, all aggregates are incorporated in clusters and none are free-flying. The histogram now shows two peaks (c., solid black line): a strong and narrow peak for bright (high) grayscale values accounting for the now very bright background,

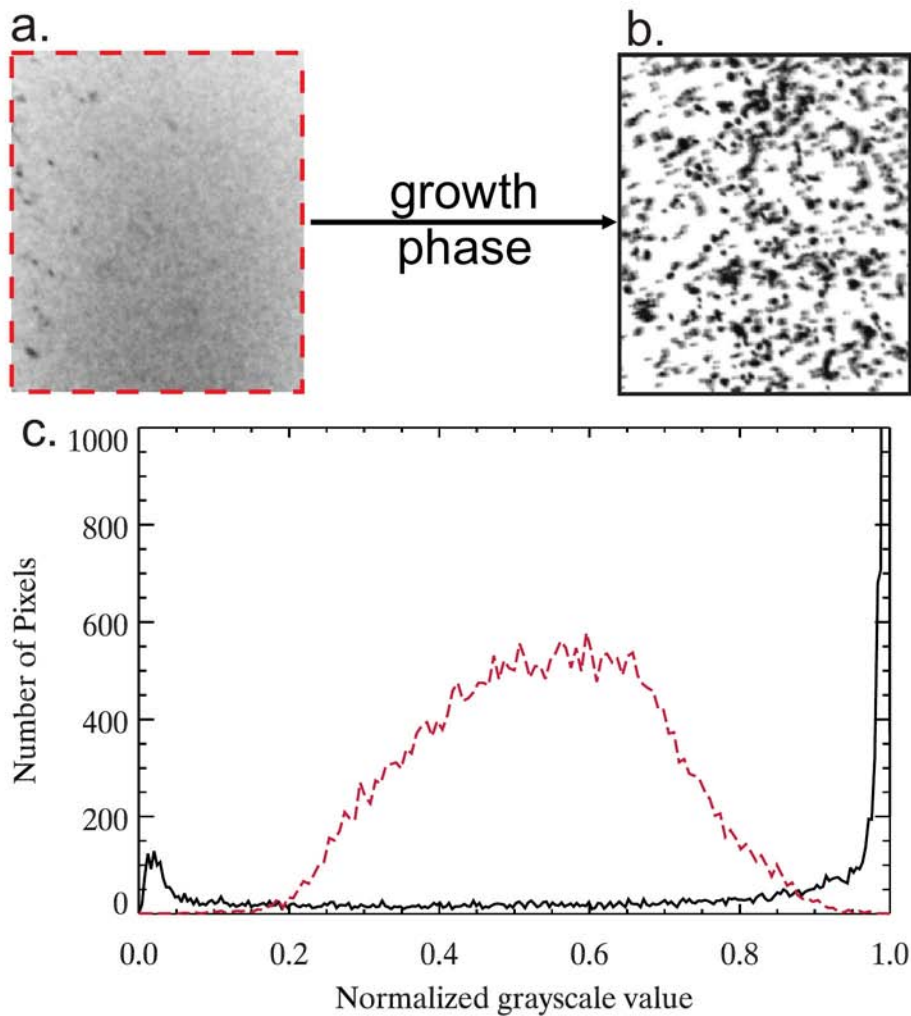


Figure 5.5: Analysis method used on the SPACE experiment data to determine the number of free-flying aggregates in the experiment cells at each moment: a. Region of interest inside an averaged data frame of the larger experiment cell (see Figure 2.4c.) at the beginning of the experiment run (1.2 s after start of recording), when all aggregates are free-flying. b. Region of interest inside an averaged data frame of the same experiment cell during a slow shaking phase (47.1 s after start of recording), when all aggregates are incorporated in clusters. c. Histograms of these frames a. and b.: when all aggregates are free-flying (a.), the background is uniformly gray (dashed red line), whereas the dark particles (small peak in lower grayscale values) and the bright background (high and narrow peak in higher grayscale values) are clearly differentiated when the aggregates are all incorporated in clusters (solid black line).

and a smaller but also quite narrow peak in very dark (low) grayscale values accounting for the visible clusters on the cell walls. As the glass remained perfectly clean during the experiment run (see Section 5.4.3), these two frames can be used to calibrate the background grayscale to the fraction of aggregates free-flying in the cell volume at this time (see Section 6.2.1).

The other analysis method consists in binarizing the averaged frames and look at the area covered by clusters at a certain point in time. Figure 5.6 illustrates this by presenting two frames at the beginning and the end of a fragmentation phase: clusters (black areas) have dissolved with time. The total frame surface covered by clusters can be tracked with time and plotted according to the collision velocity (see Section 6.2.2).

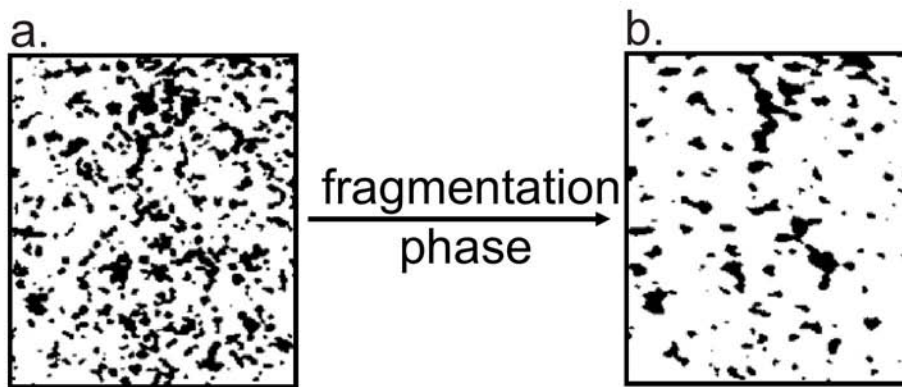


Figure 5.6: Analysis of the clusters growing on the cell walls inside the SPACE experiment during the suborbital flight : a. Region of interest inside an averaged and binarized data frame of the bigger experiment cell at the beginning of a fragmentation phase (61.8 s after beginning of the recording) and b. Region of interest inside an averaged and binarized data frame of the same cell at the end of this fragmentation phase (76.5 s after beginning of the recording). The frame area covered by clusters (black areas) has decreased.

5.4 Suborbital flight frame correction

To allow for the statistical data analysis described above, the correction of the recorded frames is of utmost importance. Averaging can only be performed on non-moving frames (the original frame sequence was rotating with the shaking mechanism). Moreover, a background grayscale analysis can only deliver meaningful information if the frame background is spatially (over the entire cell) and timely (during the entire experiment) uniform.

5.4.1 Cell rotational movement

In order to obtain non-moving cell walls in each frame, the cell rotation induced by the shaking mechanism had to be corrected. In this new reference system, free-flying aggregates and clusters on the glass walls can easily be identified: the latter are immobile over all frames, while free-flying aggregates are still moving. The initially linear aggregate trajectories are transformed into cycloids.

The first step in performing this correction was to determine the position of the experiment cell walls in each frame. In a second step, each frame was shifted in a way that the cell walls were always at the same position.

The shifting of the frame to place the cell walls at the same position in each frame induced the loss of border regions for each cell, reducing the further analysis to a region of interest covering the inner part of the cells. However, as the clusters on the side walls were not

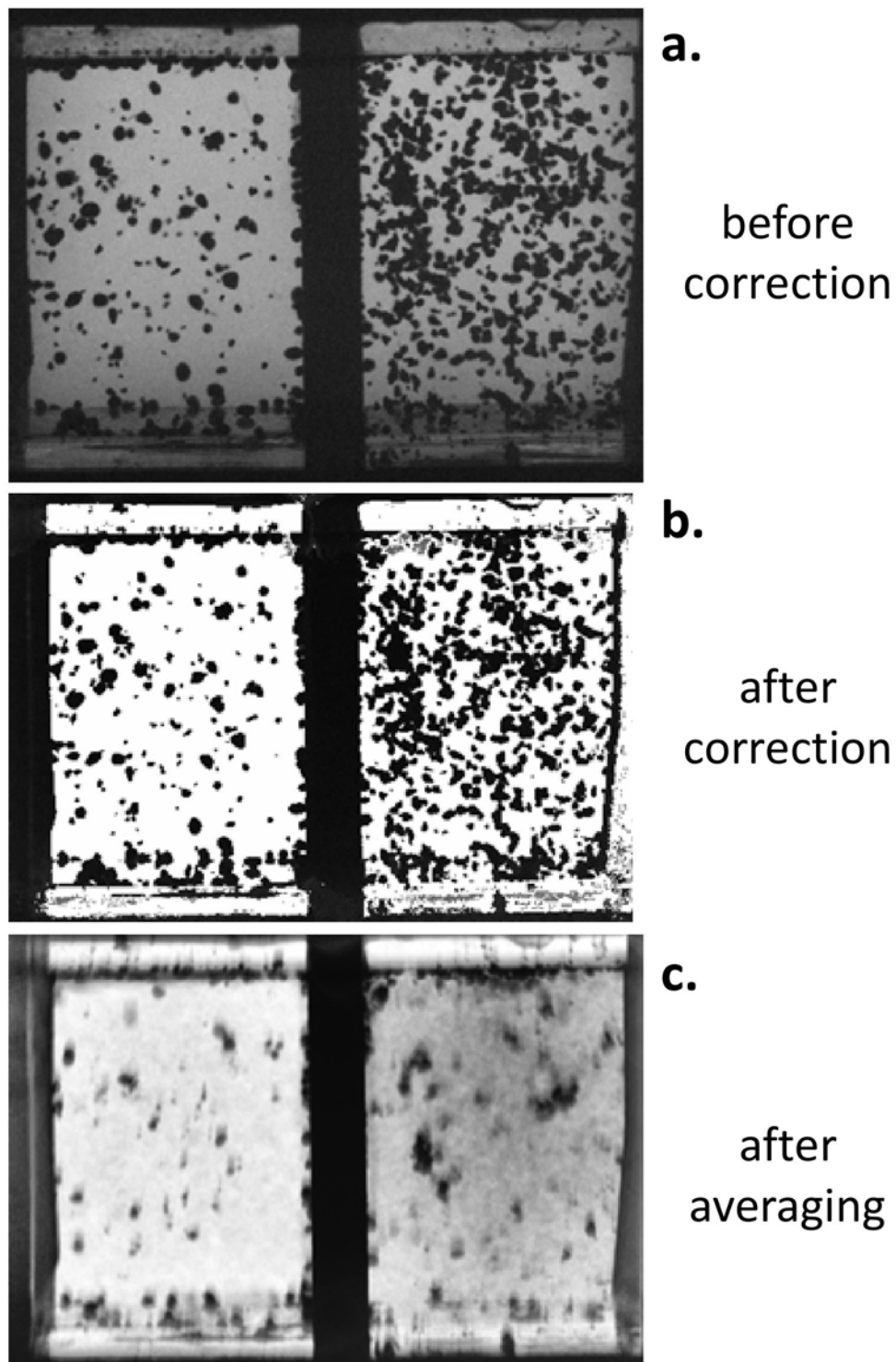


Figure 5.7: Image processing: a. SPACE data frame at 11.8 s after beginning of frame recording showing the two lower experiment cells (containing $\sim 320 \mu\text{m}$ aggregates), b. the same frame after background illumination correction, c. the same frame after background correction and averaging over 201 frames (1.2 s). The clusters on the cell wall become apparent and the background grayscale value depends on the number of free-flying aggregates.

properly visible and could not be used in the data analysis, the loss of these border regions did not impact the results. Moreover, the preferential agglomeration of aggregates into one corner of the cells due to residual flight accelerations (see Section 5.6.1) had less influence on the results, as the borders were partially cut off.

This method successfully eliminated the rotational movement of the experiment cells from the recorded frames. However, the cells had an additional movement along the line of sight of the camera: they were wobbling slightly due to frictions between the cog wheels of the shaking mechanism. This produced a non-zero noise level in the grayscale histogram of averaged frames (see Figure 5.5c.) that could be disregarded as not being related to the number of free-flying aggregates.

5.4.2 Background illumination

As the background grayscale value of the images was an indicator of the number of free-flying aggregates in the experiment cell volumes, it was essential to perform background correction (flat-fielding) for each frame. In a first step the background illumination of the cells was determined. The main background imperfections were a darker spot due to one non-functioning LED and a loss in the light intensity towards the lower cell regions due to the edge of the LED array (both can be seen in Figure 3.9). These imperfections were specific to the SPACE experiment run on the rocket and could not be corrected by subtracting a previously taken background frame: the background illumination had to be determined from the flight frames.

To do this, the value of each pixel of a reference frame was set to the grayscale value that was most frequently displayed during the time of the experiment run. As aggregates were never covering the same area during all 150 s of recording, this most frequent value was the background grayscale. The result of subtracting this computed background to the recorded frames can be seen in Figure 5.7b.

5.4.3 Glass cleanliness

The aggregates observed in the SPACE experiment were composed of dust monomer particles and the high number of collisions taking place during the 150 s of experiment run in microgravity could have led to aggregate erosion, liberating fine μm -sized dust in the experiment cell. This fine dust sticking to the glass walls would have led to a gradual smearing, thereby influencing the background grayscale value of the averaged frames (as well as the background illumination correction described above). Therefore, the glass cleanliness along the experiment run had to be checked.

To this purpose, one pixel of each cell was chosen and its grayscale value measured at three points in time: once at the beginning of the experiment, once in the middle and once at the end. It was assessed that the background grayscale values did not change during the experiment and stayed at ~ 172 , 187 and 175 for the three chosen pixels, respectively (Figure 5.8). The result of this investigation guarantees that the glass stayed perfectly clean during the whole experiment run and no further correction was required.

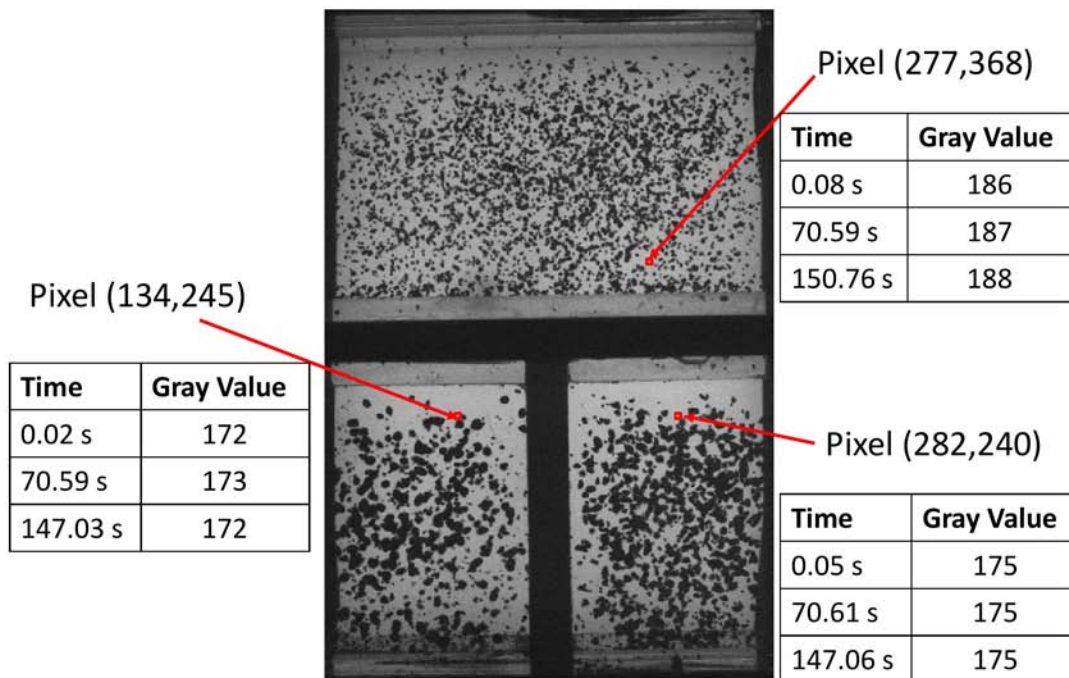


Figure 5.8: Glass smearing analysis: by choosing three random background pixels at the beginning (up to 0.08 s), in the middle (around 70 s) and at the end (after 147 s) of the experiment run and looking at their gray scale value it can be concluded that the glass walls of the experiment cells stayed clean during the whole experiment. The times refer to the start of data recording.

5.5 Determination of the statistical relative velocities

As mentioned in Section 5.3, the optical depth in the SPACE suborbital flight experiment was too high to track aggregates individually. It was therefore not possible to determine collision velocities by following the aggregate positions with time. This led to a statistical approach of the aggregate velocity determination, according to the shaking frequency of the experiment cells. In a first step, this rotation frequency was measured from the recorded data. This rotation speed was then used to determine a mean collision velocity between free-flying aggregates and the clusters on the experiment cell walls.

5.5.1 Wall velocity

The rotation velocity of the experiment cells was determined by the rotation velocity of the DC/DC motor (see Section 2.2.1 for a description of the shaking mechanism). Figure 3.5 shows the input voltage received by the motor during the experiment run on REXUS 12. However, the motor rotation speed did not follow the input voltage linearly. The exact cell rotation speed at each moment had to be determined from the data recorded during the flight.

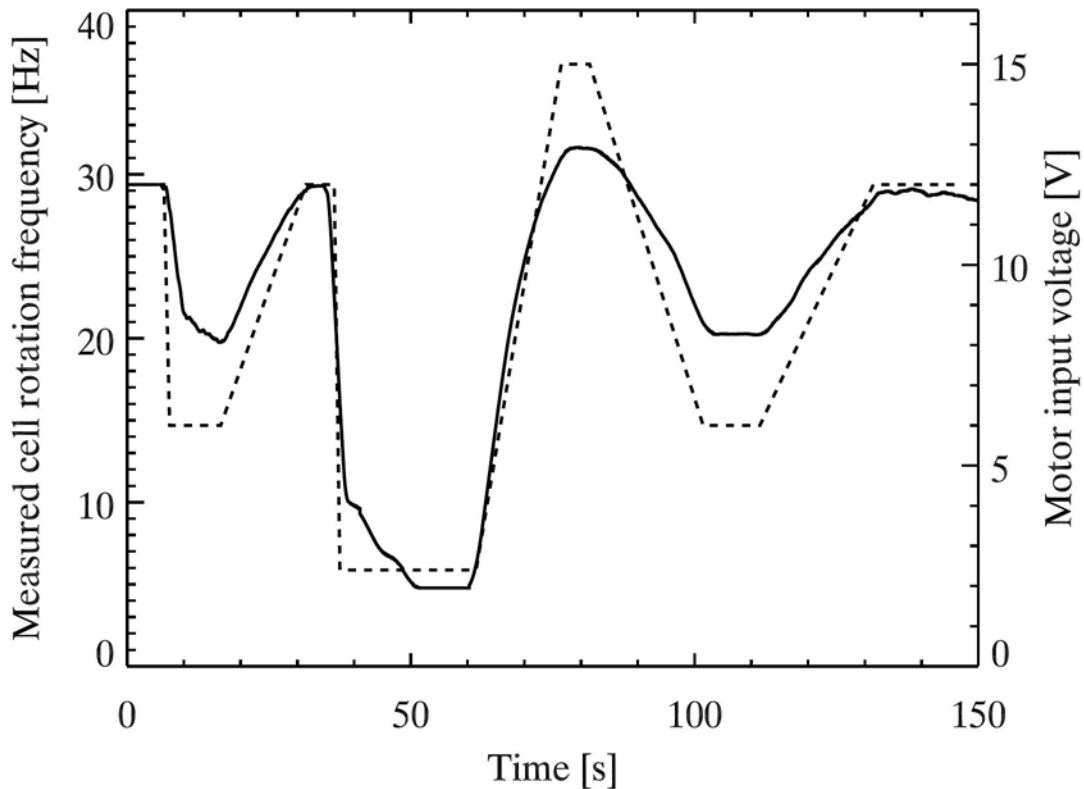


Figure 5.9: Measured motor rotation frequency during the SPACE suborbital flight experiment (solid line, left axis). Also plotted is the motor input voltage (dashed line, right axis).

This was done by counting the number of frames needed for a full rotation. The rotation velocity obtained at a full turn was then interpolated between each measured value (full turn) to obtain a rotation velocity at each recorded frame between the full turns. The result of this investigation can be seen in Figure 5.9 (solid line, left axis). Also plotted is the motor input voltage (dashed line, right axis). As can be noticed, the motor response behaved non-linearly when outside the nominal input voltage range (around 12 V). Furthermore, the fast downward ramps displayed a damping before settling to the lower shaking velocities.

5.5.2 Calculating the aggregate relative velocities

The residual accelerations during flight (see Section 5.6.1) were neglected and the velocity of the dust aggregates was assumed to be solely induced by collisions with the container walls. For the two sizes of experiment cells and dust aggregates, the mean free path of the aggregates inside the cell volume was calculated with $\lambda = 1/(n\sigma)$, n being the number density of particles in the experiment cell, and σ their mean cross section. For the smaller

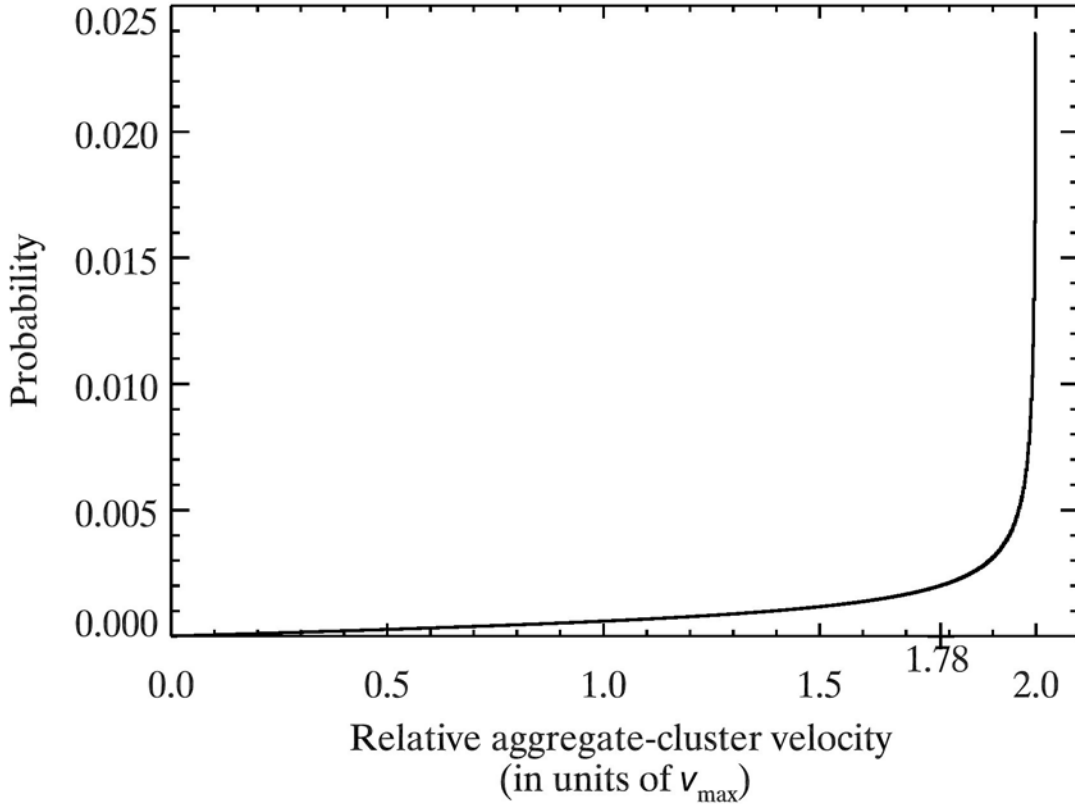


Figure 5.10: Resulting relative collision velocity probability between an in-flying aggregate at v_{\max} and a rotating cluster on the wall with linear velocity v_{\max} . The mean of all possible collision velocities weighted by their probability is at $1.78v_{\max}$.

size distribution counting ~ 4240 aggregates of mean diameter $120 \mu\text{m}$ and a cell volume of $15 \times 10 \times 24 \text{ mm}^3$, the mean free path was $\lambda = 16 \text{ mm}$. For the larger size distributions counting ~ 375 aggregates of mean diameter $320 \mu\text{m}$ and a cell volume of $15 \times 10 \times 11 \text{ mm}^3$, the mean free path was 13 mm . Thus, in both cases the mean free path of the aggregates was comparable with the size of the cell. Considering collisions between aggregates and the cell walls to be perfectly inelastic, and knowing that the pressure in the cells was below 10^{-4} mbar during the experiment run (the influence of gas on the aggregate trajectory could be neglected), the free-flying aggregates were assumed to obtain and retain the maximum linear wall velocity until they collided with another aggregate or cluster on the cell walls. The clusters growing on the wall were rotating at wall speed (see Figure 5.9 for the cell shaking profile). The relative velocity between the incoming aggregate and the rotating cluster was between 0 and $2v_{\max}$, v_{\max} being the maximum wall velocity. Indeed, as just described, a free-flying aggregate moving towards the wall was approaching with a velocity v_{\max} (considered constant). On the other hand, a cluster growing on the wall had a velocity v_{clus} , ranging from $-v_{\max}$ to v_{\max} , as it was rotating at wall frequency. Thus the relative velocity v_{rel} was in the range $0 \leq v_{\text{rel}} = v_{\max} + v_{\text{clus}} \leq 2v_{\max}$.

In the collision direction, the cluster had a sinusoidal linear velocity of the form $v_{\text{clus}} = r\omega\cos(\omega t)$ varying between $v_{\text{max}} = r\omega$ and $-v_{\text{max}}$. Its probability of having a velocity v at the time of collision was

$$P(v)dv = f \times [t(v + \frac{dv}{2}) - t(v - \frac{dv}{2})] \quad (5.6)$$

with $f = \frac{\omega}{2\pi}$ the cell rotation frequency and $t(v) = \frac{1}{\omega}\arccos(\frac{v}{r\omega})$. As described in Weidling et al. (2009), the chances of an aggregate colliding with a cluster moving away from it were lower than the chances to hit a cluster moving towards it. Hence, the probability of equation 5.6 was convolved with a linear collision probability from 0 to 1 between 0 and $+v_{\text{max}}$ (only aggregates moving towards the cluster on the cell wall were considered). The resulting probability of a certain collision velocity is shown in Figure 5.10. The most frequent collision velocity was at twice the maximum linear wall velocity, $2v_{\text{max}}$. The relative velocity used for the further data analysis was the mean of the possible velocity range (between 0 and $2v_{\text{max}}$) weighted by the velocity probability: $1.78v_{\text{max}}$.

5.6 Other influences on the aggregate motion

This section estimates the disturbance accelerations acting on the dust aggregates observed and compares them to the intentionally induced shaking accelerations.

5.6.1 Residual accelerations during the suborbital flight

During the experiment on the suborbital flight, the dust aggregates in the containers were subjected to two types of residual acceleration: atmospheric drag and rocket spin.

The residual atmospheric drag accelerations were due to the fact that the REXUS 12 rocket had an apogee of 82 km, an altitude at which the aerodynamic effects of the remaining atmosphere on the rocket were still influential. The drag force induced along the direction of flight was $F_{\text{drag}} = \frac{1}{2}\rho v^2 A C_d$, with ρ being the local air pressure, v , A and C_d the rocket's flight velocity, cross section and drag coefficient, respectively. Comparing the rocket's flight altitude profile with the recorded SPACE data, it could be determined that the frame streaming started at an altitude of about 70 km, lasted through the passing of apogee (82 km) and stopped during descent at about 50 km. Hence, it could be assumed that the relevant data used for this analysis was recorded above an altitude of 70 km (the last seconds of recording were not relevant for the data analysis). The standard atmosphere model (1976 US Standard Atmosphere) at this altitude, yields $\rho_{\text{air}} = 7.42 \times 10^{-5} \text{ kg/m}^3$. The rocket had a diameter of $d = 0.356 \text{ m}$ and a cross section of $A = \pi(\frac{d}{2})^2 = 9.95 \times 10^{-2} \text{ m}^2$. The drag coefficient $C_d = 0.341$ was calculated from measurements made on the REXUS rocket by Anderson et al. (2009) on a REXUS flight in 2009. The maximum rocket speed was $v = 562 \text{ m s}^{-1}$ at 70 km which led to a maximum drag force on the rocket of $F = 0.398 \text{ N}$. For a rocket mass of $m_r = 515 \text{ kg}$, the maximum

residual drag acceleration was $a_{\text{drag}} = F_{\text{drag}}/m_r = 7.72 \times 10^{-4} \text{ m s}^{-2} = 7.86 \times 10^{-5} g$, with g being the Earth's gravitational acceleration. As the dust aggregates were free-flying in vacuum inside of the experiment cells, which are directly coupled to the rocket itself, this was the residual drag acceleration they experience relative to the cell walls.

The residual rotation speed of the rocket after de-spin was measured by the Service Module to be $\omega_r = 11 \text{ deg/s} = 0.19 \text{ rad/s}$. The resulting centrifugal acceleration on one of the SPACE dust aggregates was $a_{\text{centrif}} = \omega_r^2 R$ with R being the distance of the aggregate to the roll axis of the rocket. The way the experiment was designed, the distance to the rocket's roll axis could be approximated to $R = 0.04 \text{ m}$. Thus, the residual spin acceleration on an aggregate was about $a_{\text{centrif}} = 1.47 \times 10^{-4} g$ with g being the Earth's gravitational acceleration.

The effects of these residual accelerations on the behavior of the dust aggregates can be seen in Figure 3.9b. The tendency of the aggregates to gather in the upper left corner of the frame revealed the combination of a residual acceleration acting on them in the direction of flight (vertically on the frames) and in the radially outward direction (horizontally), increasing the number of their collisions in this corner of the cell.

To see if these two residual accelerations had an influence on the collision behavior of the observed aggregates, the values calculated were compared to the accelerations induced by the rotating cell walls. The minimum rotation frequency of the cells was $f_{\text{min}} = 4.78 \text{ Hz}$, inducing a minimum wall acceleration of $a_{\text{min}} = (2\pi f_{\text{min}})^2 \tilde{r} = 0.90 \text{ m s}^{-2} = 9.2 \cdot 10^{-2} g$, $\tilde{r} = 1 \text{ mm}$ being the rotation radius of the experiment cells. This is almost 3 orders of magnitude stronger than the residual accelerations calculated above. It is therefore reasonable to neglect the effects of residual accelerations in the data results.

5.6.2 Magnetic and electrostatic effects on the aggregate trajectories

To validate the data results as being meaningful for pure dust aggregates properties, it was also important to rule out magnetic or electrostatic effects on the collision properties. Both magnetic and electrostatic effects are known to play an important role on dust particle collisions (e.g. Poppe et al. 2000a, Nübold et al. 2003). However, in this series of experiments with SiO_2 dust aggregates the intention was to investigate aggregate properties free from these influences.

Ruling out magnetic effects was trivial as none of the materials used for this experiment were magnetic. Furthermore, to avoid electrostatic charging of any kind, the glass cells holding the particles were built inside of an aluminum frame acting as a Faraday cage and preventing the charging of the particles by the carrier (drop tower capsule or rocket). Before inserting the dust aggregates into the containers, they were grounded for several days to avoid initial particle charging.

To make sure that these precautions guaranteed negligible electrostatic effects, the charging of the aggregates observed was derived from the analyzed data. For the REXUS flight experimental data, the relevant collisions were between free-flying aggregates and clusters forming on the cell walls. Electrostatic effects were ruled out by picking a few random aggregates, which could be directly observed colliding with a container wall, and

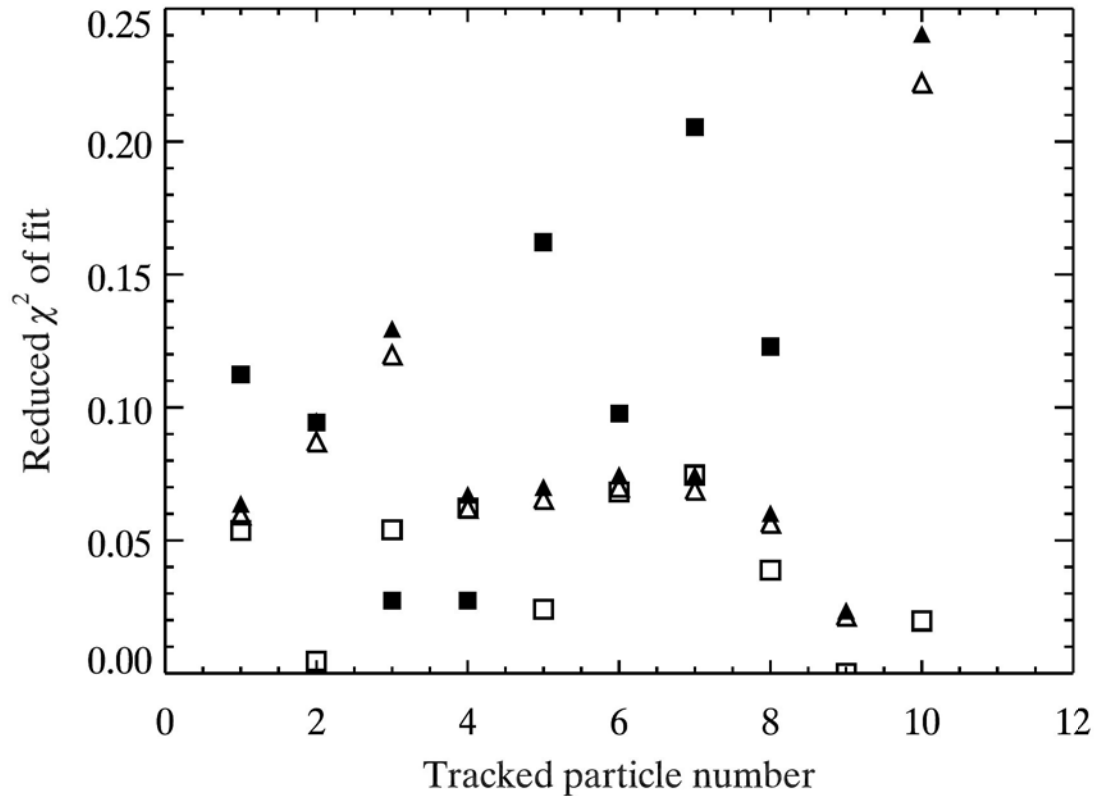


Figure 5.11: Reduced χ^2 error statistics for linear and parabolic fits to the trajectories of 10 traceable aggregates in the cell containing the larger aggregates composed of monodisperse dust during the SPACE rocket flight experiment: before (triangles, open for the linear fit and filled for the parabolic fit) and after impact with a glass wall (squares, open for the linear fit and filled for the parabolic fit).

determining the form of their trajectories. In the case of electrostatic charging of the dust and the cell walls, the aggregates would have behaved like charged particles in an electric field: their trajectories approaching the cell wall would have been non-linear with respect to time due to induced acceleration or deceleration. For the 10 analyzed collisions, the reduced χ^2 error statistics of both the linear and parabolic fit of their trajectories approaching and leaving the glass wall was measured (see Figure 5.11). The mean χ^2 error statistics for a linear trajectory fit were 0.083 and 0.040 before and after the aggregate collision with the cell wall, respectively. For the parabolic fit, these values were 0.90 and 0.12, respectively, indicating a better fit of the trajectory to linear than to parabolic.

In the drop tower data, each aggregate and cluster was tracked individually and the reduced χ^2 error statistics of both the linear and parabolic fit of each trajectory could be determined. Figure 5.12 plots the normalized cumulative aggregate count for the error statistics values (number of aggregates with a reduced χ^2 parameter lower than the value indicated on the x-axis). The deviation from the parabolic fit (dashed line) is higher than the deviation from the linear fit (solid line), indicating a better fit of the trajectory to linear than parabolic. For both these data sets, the second degree coefficient of the parabolic fit, p_2 , can be related to an electrical charge of the corresponding aggregate. If each aggre-

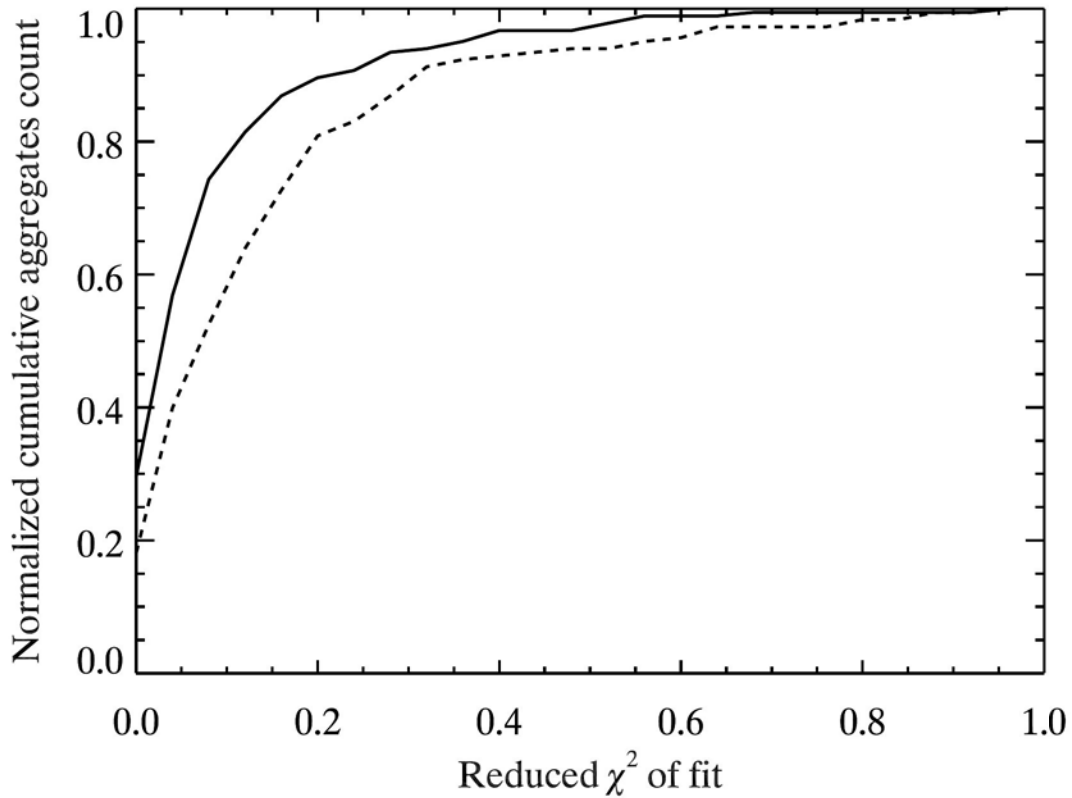


Figure 5.12: Cumulative aggregate count for the reduced χ^2 error statistics for linear and parabolic fits to the trajectories of all tracked dust aggregates during the SPACE drop tower experiments (solid line for the linear fit and dashed line for the parabolic fit). The y-axis gives the normalized number of aggregates with a reduced χ^2 error statistics parameter lower than the number indicated on the x-axis.

gate is considered as being a particle of charge q moving in a uniform electric field E , then $p_2 = \frac{1}{2} \frac{qE}{m}$, with m being the mass of the aggregate, in a gross approximation. The electric field was approximated to be $E = \frac{q}{4\pi\epsilon_0 r^2}$ with ϵ_0 being the dielectric constant in vacuum and r the distance from the aggregate to the interacting charge (taken here as about twice the aggregate diameter). The charge q producing the electric field was assumed to be held by an aggregate that was either also free-flying, in the case of the drop tower experiments, or sticking to the cell wall, in the case of the suborbital flight experiment. This charge was considered identical to the charge of the in-flying aggregate whose trajectory was being investigated. The mean number of elementary charges carried by each monomer particle ($\sim 1 \mu\text{m}$ in size) was calculated to be 0.015 and 0.57 for the suborbital flight and the drop tower experiments, respectively.

The induced accelerations were $a_{\text{el}} = 2p_2 = 7.27 \times 10^{-11} \text{ m s}^{-2}$ and $2.25 \times 10^{-8} \text{ m s}^{-2}$ for the suborbital flight and the drop tower experiments, respectively. These accelerations could be neglected compared to the ones induced by the cell shaking.

6 Experimental results

This section presents the results of the SPACE experiments obtained via the analysis methods described in the previous section.

6.1 Drop tower dust collisions

During the drop tower experiments, aggregates and clusters were tracked individually (see Section 5.1.1). The collisions observed took place between aggregates and clusters (Section 6.1.1) or between clusters and the experiment cell walls (Section 6.1.2). In addition to the collision properties, the cluster fractal dimensions could also be determined

6.1.1 Aggregate and cluster collisions

From the five drop tower experiments, data from eight cells could be analyzed (see Table 4.2 for the type of result). The 162 collisions observed are presented in Figure 6.1. For each collision, the mass of the smaller colliding aggregate and the collision velocity are plotted. The different symbols represent the different types of aggregates observed

Table 6.1: Legend for the symbols used to visualize collisions of different kind of aggregates observed during the SPACE drop tower experiment runs.

Aggregate type	Sticking/bouncing collisions	Fragmenting collisions
Aggregates composed of monodisperse SiO ₂	○/●	*
Compacted aggregates composed of monodisperse SiO ₂	◇/◆	x
Aggregates composed of spherical polydisperse SiO ₂	△/▲	+

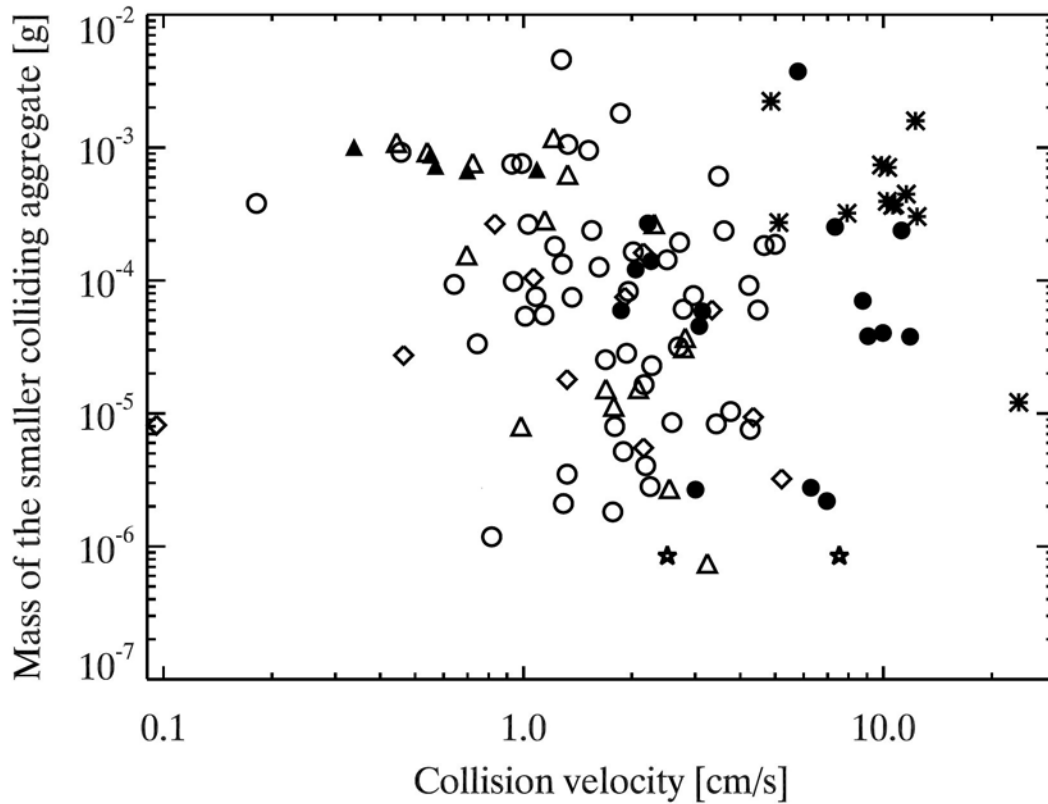


Figure 6.1: Collisions between dust aggregates and clusters during the drop tower experiments listed in Table 4.2 according to the mass of the smaller collision partner, the relative aggregate velocity and the collision outcome: sticking (open symbols) and bouncing (filled symbols). The three dust types are non-compacted and compacted aggregates composed of monodisperse SiO₂ (circles and diamonds, respectively) and spherical polydisperse SiO₂ (triangles). The data points deduced from non-agglomerating aggregates composed of irregular polydisperse SiO₂ are represented by stars.

(circles for aggregates composed of monodisperse SiO₂, diamonds for aggregates of the same material that underwent preliminary compaction and triangles for aggregates composed of spherical polydisperse SiO₂, see Table 6.1). Open symbols represent sticking, filled symbols bouncing and asterisks mark fragmenting collisions. Aggregates composed of monodisperse SiO₂ were the only ones observed fragmenting upon mutual collision.

Aggregates composed of irregular polydisperse SiO₂ did not cluster at all and their size distribution did not change during the experiment run. It can be assumed that all collisions taking place in this experiment cell lead to bouncing of both collision partners. The mean free path of these aggregates during the experiment was calculated to be $\lambda = 1/(n\sigma) = 8.31$ mm. This is of the same order as the experiment cell size, and the mean aggregate collision velocity can be determined by assuming that free flying aggregates have a speed of about v_{\max} , the maximum velocity of the cell walls (see Section 5.5.2 where the mean collision velocity between aggregates and clusters during the suborbital flight was determined in a similar manner). The resulting mean collision velocities were 2.51 cm s^{-1} for drop 2 and 7.54 cm s^{-1} for drop 3. In both cases, the mean aggregate mass was 8.61×10^{-7} g. These two "bouncing" data points are plotted as stars in Figure 6.1 and represent an average over a great number of collisions.

Aggregates composed of spherical polydisperse SiO_2 displayed two different behaviors during drop 2 and drop 5. During drop 2, the initial clusters were efficiently destroyed at a fast shaking frequency of 16.7 Hz. At the slower frequency of 5 Hz, they clustered only a few monomers at a time. These clusters were then destroyed by encounters with the cell walls before they could grow any further. They were too small and surrounded by too many free-flying aggregates for them to be tracked with the program described in Section 5.1.1. During drop 5 however, clusters started forming already during the fast shaking phase at 15.5 Hz and continued to grow at 6 Hz. In 23 sticking collisions at low velocities down to under 1 cm s^{-1} , clusters grew to masses of up to about 10^{-3} g , which corresponds to ~ 1160 monomer aggregates (triangles in Figure 6.1). 5 bouncing collisions at these velocity- and size-ranges (1 cm s^{-1} and 10^{-3} g) were observed as well (filled triangles).

For the aggregates composed of monodisperse dust that were not previously compacted, a total of 116 collisions were analyzed. The outcome of these collisions was sticking for 88 of them, bouncing for 16 and fragmentation for 12. With relative velocities down to a few mm s^{-1} , these aggregates formed clusters of up to about 10^{-2} g , which corresponds to ~ 11600 monomer aggregates. The bouncing collisions were observed at higher velocities between 2 and 11 cm s^{-1} for aggregate sizes ranging from the sieved monomer aggregate ($\sim 10^{-6} \text{ g}$) to the bigger clusters ($\sim 10^{-3} \text{ g}$). At about 5 cm s^{-1} , the first fragmenting collision was observed. Except for one, which took place at the highest observed velocity of 23.8 cm s^{-1} , the other fragmenting collisions happened in collisions between bigger clusters ($2 \times 10^{-4} \text{ g}$ and more).

Aggregates composed of monodisperse SiO_2 that were previously compacted (by shaking them 10 minutes on a plate at 10 Hz) were observed in 18 collisions resulting in sticking (diamonds). Neither bouncing nor fragmenting collisions between these aggregates could be analyzed. The aggregates were observed during drop 3, which had the slowest shaking profile from all considered drops (10.5 and 3 Hz shaking frequencies compared to >15 and >5 Hz for drops 2 and 5). Therefore, the collision velocities were also smaller, ranging from 0.1 to 6 cm s^{-1} . The masses of the clusters reached $5 \times 10^{-4} \text{ g}$, which is more than one order of magnitude smaller than those composed of aggregates that were not previously compacted.

6.1.2 Cluster restructuring and fragmentation

In addition to the collisions between aggregates and clusters, the drop tower data also showed collisions of aggregates or clusters with the cell walls. These aggregates were tracked and the collision properties were deduced (Figure 6.2). The highest observed collision velocities were around the maximum wall speed of $\sim 20 \text{ cm s}^{-1}$, corresponding to the maximum shaking frequency of 16.7 Hz. The mass presented is the reduced mass of the collision, i.e. the mass of the aggregate/cluster, as in comparison, the wall is considered to have an infinite mass.

For aggregates composed of monodisperse SiO_2 , 64 bouncing and 37 fragmenting wall collisions were observed. For smaller clusters of masses between 10^{-4} and 10^{-3} g , both

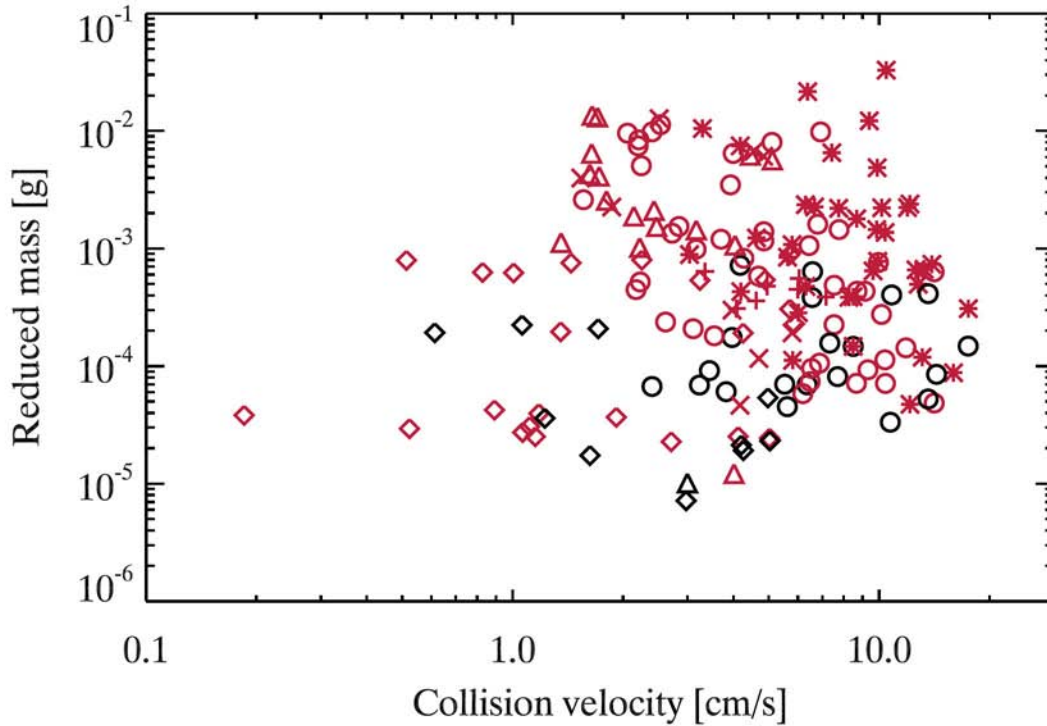


Figure 6.2: Outcome of collisions between aggregates or clusters with the experiment cell walls during the SPACE drop tower experiments. The symbols used are listed in Table 6.1. No sticking collisions with the walls were observed and bouncing collisions are represented by open symbols for an easier graph reading. Asterisks, plus and x signs represent fragmentation collisions for non-compacted and compacted aggregates composed of monodisperse dust and aggregates composed of polydisperse dust, respectively. Collisions for which aggregate or cluster restructuring was visible are showed in red.

collision outcomes were observed for the maximum velocities of $\sim 20 \text{ cm s}^{-1}$. Bigger clusters, however, fragmented more frequently than they bounced. The two other types of aggregates also displayed a transition from bouncing to fragmentation with increasing cluster mass and velocity. For compacted aggregates composed of monodisperse dust, 34 bouncing and 8 fragmenting wall collisions were observed. For aggregates composed of spherical polydisperse dust, 17 bouncing and 9 fragmenting wall collisions were observed.

Figure 6.2 shows all the collisions between aggregates/clusters and the cell wall in the drop tower experiments, according to the reduced mass of the collision and the collision velocity. Collisions where aggregate or cluster restructuring was visible are plotted in red. For the non-compacted aggregates composed of monodisperse dust and the aggregates composed of polydisperse dust, most of the restructuring events occurred at velocities and masses higher than 5 cm s^{-1} and 10^{-4} g , respectively, and became more frequent with increasing velocity and cluster mass. For the compacted aggregates composed of monodisperse dust, restructuring events already occurred at velocities as low as 0.19 cm s^{-1} for masses around $4 \times 10^{-5} \text{ g}$.

It can be noted that even at higher relative velocities, the bigger clusters observed colliding with the cell walls had masses of up to $\sim 10^{-2}$ g. For aggregates composed of polydisperse SiO_2 , these clusters formed during the fast phase of the shaking profile of the experiment in a growth process just like the bigger clusters observed colliding with each other inside of the cell volume (see Section 6.1.1). For the other two aggregate types, the clusters observed colliding with the cell walls were remnants of the drop tower capsule launch. They formed while aggregates were lying in a heap on the bottom of the cell and were pressed together when the capsule was accelerated. Afterwards, they were partially destroyed by the fast shaking at the beginning of the microgravity phase, which reduced their size.

6.1.3 Cluster fractal dimensions

The mean 2D fractal dimension of the tracked clusters, determined via the box-counting method described in Section 5.1.2, was 1.70. The individual fractal dimensions are plotted in Figure 6.3 according to the cluster equivalent radius. This equivalent radius is calculated based on the aggregate projected cross section. It corresponds to the radius of a sphere with the same cross section area as the aggregate. As in Figure 6.1, diamonds and circles represent compacted and non-compacted aggregates composed of monodisperse dust, respectively, and triangles represent aggregates composed of polydisperse dust (see Table 6.1). The fractal dimensions range from 1.53 to 1.94 at smaller aggregate sizes of around 0.03 cm equivalent radius and from 1.61 to 1.71 at bigger sizes of about 0.16 cm (see Figure 6.4 for some examples). It can be seen that the clusters composed of compacted aggregates do not reach the same sizes as those composed of non-compacted aggregates (equivalent radii up to 0.062 cm instead of 0.16 cm for non-compacted aggregates). Their fractal dimensions are also lower than for clusters composed of non-compacted aggregates: the mean value is 1.69, while clusters composed of non-compacted aggregates have a mean fractal dimension of 1.76. The mean fractal dimension of the clusters composed of aggregates of polydisperse dust is 1.72.

The fractal dimension of the aggregates/clusters colliding with the cell walls were determined in the same manner (Figure 6.3b). The values range from 1.52 to 1.93 for a mean value at 1.71. Compacted and non-compacted aggregates composed of monodisperse dust have mean fractal dimensions of 1.66 and 1.76 respectively and the aggregates composed of polydisperse dust have a mean fractal dimension of 1.73.

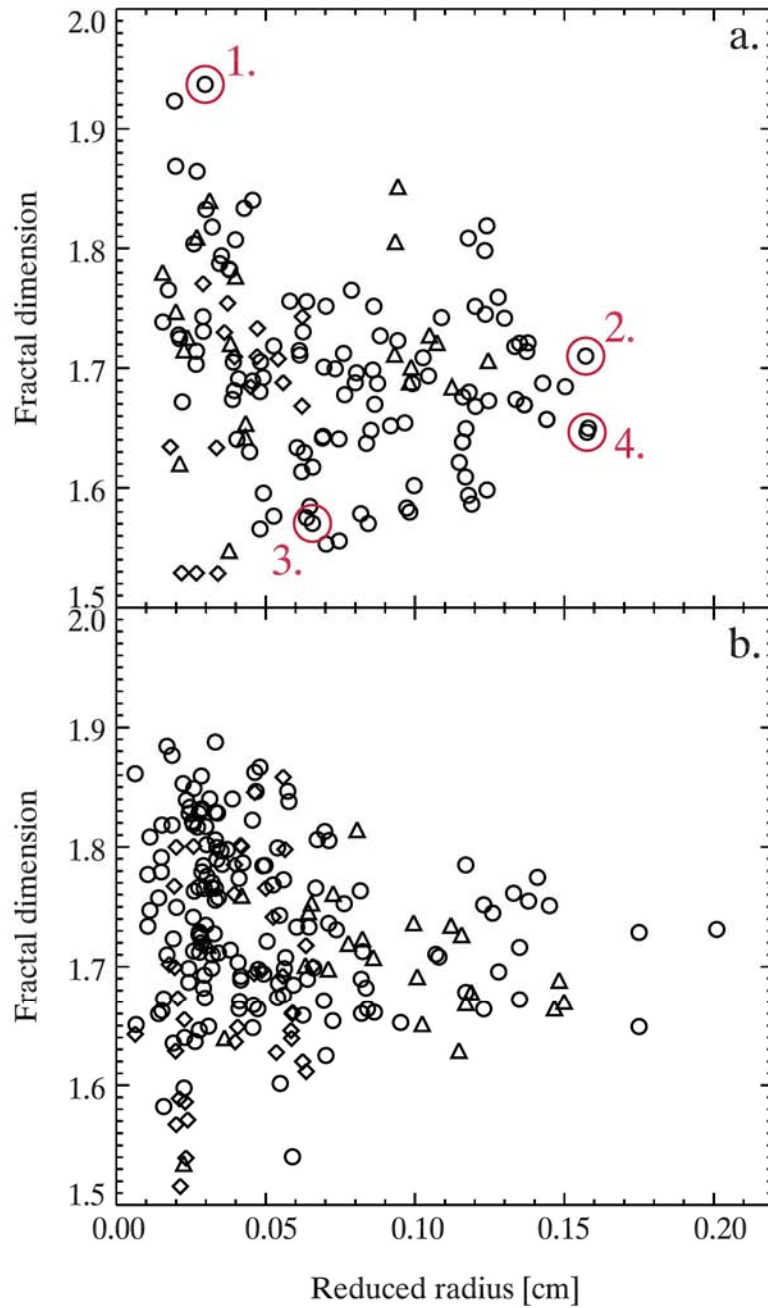


Figure 6.3: Drop tower aggregate and cluster fractal dimensions: a. Two-dimensional fractal dimensions of the aggregates tracked during the drop tower experiment runs plotted against their mean equivalent radius for aggregates involved in inter-aggregate collisions. The symbols correspond to the different types of aggregates observed (see Table 6.1. The aggregates/clusters marked with numbers are shown in Figure 6.4. b. Two-dimensional fractal dimensions of the aggregates/clusters colliding with the experiment cell walls during the drop tower experiment runs plotted against their mean equivalent radius for the three types of aggregates observed. The symbols used are listed in Table 6.1.

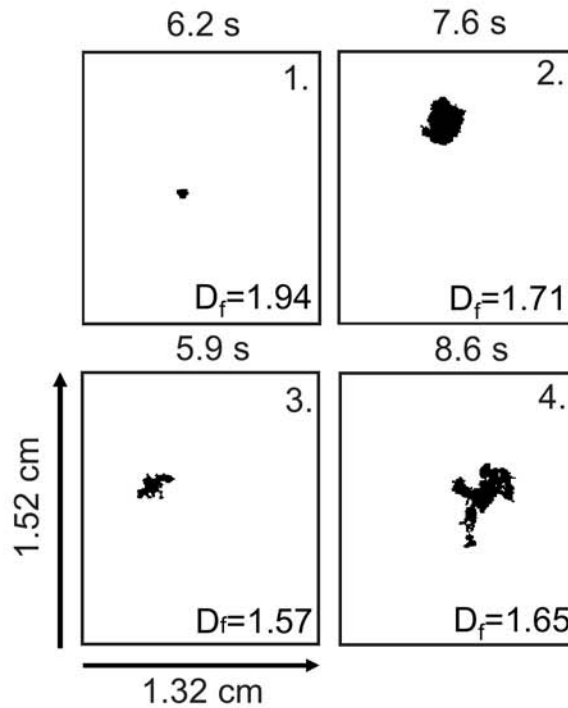


Figure 6.4: Examples of aggregates/clusters composed of monodisperse SiO_2 displaying the maximum (a,b) and minimum (c,d) fractal dimension for their respective sizes: 1. fractal dimension $D_f = 1.94$ and equivalent radius $r_{\text{eq}} = 0.30$ mm, 2. $D_f = 1.71$ and $r_{\text{eq}} = 1.57$ mm, 3. $D_f = 1.57$ and $r_{\text{eq}} = 0.66$ mm and 4. $D_f = 1.65$ and $r_{\text{eq}} = 1.58$ mm. These four examples are from drop 2 cell 3 (see Table 4.2) and their fractal dimension and radii are marked in Figure 6.3. The time elapsed after start of data recording (launch of the drop tower capsule) is indicated.

6.2 Suborbital flight dust collisions

This section describes the results obtained by the SPACE suborbital flight experiment. As described in Section 5.3, the flight data was analyzed in a statistical manner, unlike the drop tower data, where collisions were tracked individually. The background grayscale analysis allowed for a determination of the number density of free-flying aggregates (Section 6.2.1). Together with the analysis of clusters growing on the cell walls (Section 6.2.2), the sticking probability of the aggregates in the SPACE experiment could be determined continuously during the growth phases of the experiment shaking profile (Section 6.2.3). Furthermore, the dismantling of clusters during fragmentation phases allowed for a determination of the pull-off forces of aggregates from the surfaces of these clusters.

6.2.1 Number density of free-flying aggregates

As described in Section 5.3.1, the background grayscale of the averaged recorded frame delivered information on the number of free-flying aggregates in the inner cell volume at each moment. In the following, this is quantified to determine the number density of free-flying aggregates during the different phases of the experiment.

The background grayscale value of each averaged frame was determined as being the maximum of the normalized histogram of this frame (see Figure 5.5c., solid line). When no aggregates were flying in the cell volume, the background had the brightest possible value which is 1. When all aggregates were free-flying, like at the very beginning of the experiment (see Figure 5.5c. dashed red line), its value was around 0.7.

This background grayscale value, G , is related to the optical depth of the aggregate system τ , by $G = e^{-\tau}$. The optical density is in turn related to the aggregate number density in the experiment cell volume n , by $\tau = n\sigma_{\text{mono}}L$, where σ_{mono} is the projection area of one monomer aggregate and L the depth of the experiment cell. Accordingly, the number density of free-flying aggregates is

$$n = -\frac{\ln(G)}{\sigma_{\text{mono}}L}. \quad (6.1)$$

The aggregate number density over the experiment is plotted in Figure 6.5. The slow shaking phase of the second cycle (see Table 3.3) can clearly be recognized at around 50 s after start of data recording: no aggregates were flying in the volume. The two other slow shaking phases (cycles 1 and 3) were less pronounced at around 15 and 110 s after start of data recording, as both still had free-flying aggregates.

6.2.2 Growth of clusters on the cell walls

When averaging the corrected recorded frames, the clusters growing on the glass walls become visible (see Figure 5.5b.). Figure 6.6 shows the evolution of the total area covered by these clusters in a frame during the experiment run: during fast shaking phases, the clusters covered no or only small surfaces, while the maximum value of the cluster area was reached during the very slow shaking phase of cycle 2 after around 50 s after start of data recording. The absolute value of the area covered by clusters growing on the cell walls appears to be higher for the large size distribution of aggregates composed of monodisperse dust than for the two other types of dust. However, this had no influence on the results as only derivative values were used. As this difference is not reflected in the background grayscale analysis, it is likely that, by chance, more growth seeds were created on the glass surfaces perpendicular to the line of sight, compared to the two other cells, where parallel surfaces, which do not get accounted for in the absolute value of wall cluster surfaces, got more of the flying aggregates.

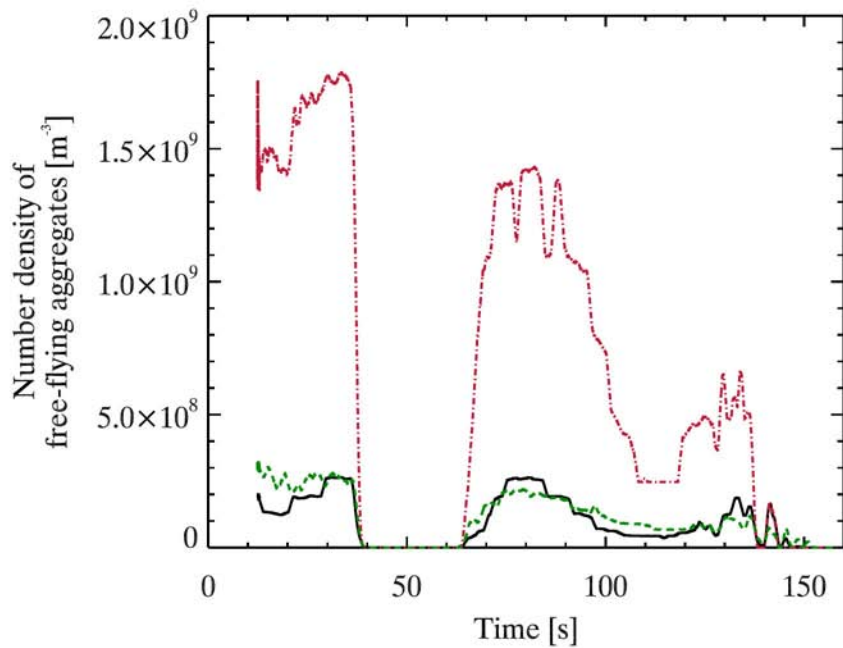


Figure 6.5: Particle number densities in the three cells of the SPACE experiment: the large size distributions of aggregates composed of poly- and monodisperse dust (black solid and green dashed lines, respectively) and the small size distribution of aggregates composed of monodisperse dust (red dash-dotted line). The origin of the times is at start of data recording.

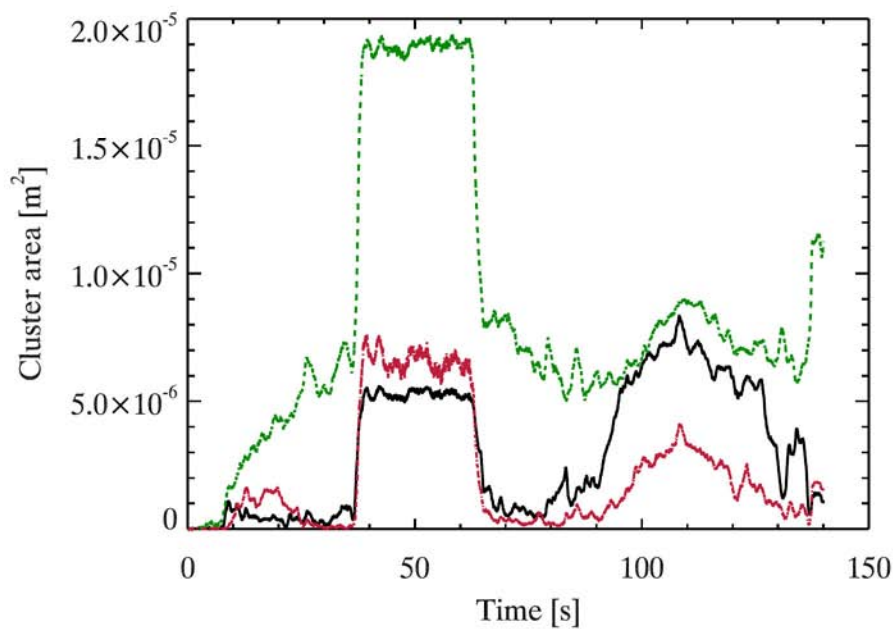


Figure 6.6: Cell wall surface area covered by clusters during the SPACE experiment for all three dust types: the large distribution of aggregates composed of poly- and monodisperse dust (black solid and green dashed line, respectively) and the small distribution of aggregates composed of monodisperse dust (red dash-dotted line). The origin of the times is at start of data recording.

6.2.3 Sticking probability

The derivative of the number density profile determined above can be used to derive the growth rate dn/dt of clusters during slow shaking phases (6 to 15 s, 35 to 46 s and 85 to 112 s, see Figure 3.5 and Table 3.3), which in turn can be used to calculate the sticking probability β of the coagulating system of aggregates.

Smoluchowski's equation for particle coagulation can be adapted to the assumption that the growing clusters in the SPACE experiment were composed of a number i of single monomer aggregates (see Smoluchowski 1916, Blum 2006):

$$\begin{aligned} \frac{\partial n(i, t)}{\partial t} = & \frac{1}{2} \sum_{j=1}^{i-1} K_a(j, i-j)n(j, t)n(i-j, t) \\ & - n(i, t) \sum_{j=1}^{\infty} K_a(j, i)n(j, t) \end{aligned} \quad (6.2)$$

Here, $n(i, t)$ is the number density of aggregates composed of i monomers at a time t and K_a the collision kernel for ballistic collisions between aggregates composed of i and j monomers, respectively. In this equation, the first term on the right-hand side accounts for the creation of aggregates composed of i monomers by differently-sized aggregates, while the second term accounts for the depletion of aggregates composed of i monomers to form bigger clusters. The collisions taking place in the SPACE experiment cells during growth phases were mainly between monomer aggregates and clusters growing on the cell walls thus depleting the inner cell volume of free-flying aggregates. This implies that the first term on the right-hand side of equation 6.2 is non-existent (no aggregates composed of i monomers are created inside the cell).

In the second term on the right-hand side, the collision kernel is defined as

$$K_a(j, i) = \beta(j, i; v)v(j, i)\sigma(j, i) \quad (6.3)$$

In this kernel, $v(j, i)$ is the relative velocity between the aggregates composed of j and i monomers, respectively, $\sigma(j, i)$ the collision cross section between such two aggregates and $\beta(j, i; v)$ the sticking probability of their collision. For the collisions considered here, the sticking probability and relative velocity are considered to be the same for all aggregates at each moment. Hence, equation 6.2 becomes

$$\frac{dn(i, t)}{dt} = -n(t)n'(t)\beta(t)\sigma_{\text{cross}}(t)v(t) \quad (6.4)$$

where $n(t)$ is the number density of free-flying aggregates in the cell volume at time t determined in Section 6.2.1, $dn(t)/dt$ is the number density of aggregates incorporated

in clusters on the cell walls determined in Section 6.2.2, $\beta(t)$ and $v(t)$ are the sticking probability and relative velocity of the collisions between the monomer aggregates and the clusters on the cell walls, respectively. $\sigma_{\text{cross}}(t)$ is the mean collision cross section between a free-flying aggregate and a cluster on the wall, and $n'(t)$ the number density of clusters on the cell walls in the experiment cell.

The relative velocity v between the free-flying monomer aggregates and the rotating clusters on the cell walls has been determined in Section 5.5.2. The collision mean cross section σ_{cross} was calculated at each moment t of the experiment run by summing up the collision cross sections of all clusters on the cell walls:

$$\begin{aligned}\sigma_{\text{cross}}(t) &= \frac{1}{N(t)} \sum_{k=0}^{N(t)} \sigma_{\text{cross},k} \\ &= \frac{1}{N(t)} \sum_{k=0}^{N(t)} 2R_k(t) \cdot 2r \\ &= \frac{4r}{N(t)} \sum_{k=0}^{N(t)} R_k(t)\end{aligned}\tag{6.5}$$

where $N(t) = n'(t)V$ is the total number of clusters on the cell walls (V being the cell volume) and R_k and r are the radii of the wall cluster k and a monomer aggregate, respectively. This assumes that the clusters on the cell walls have a thickness of about one monomer aggregate and that the monomer aggregates approach them perpendicular to the camera field of view, due to their motion induced by wall collisions. To support this assumption, a typical wall cluster was chosen in the cell containing the larger size distribution of aggregates composed of monodisperse dust. In this cluster, the constituting monomer aggregates can still be distinguished. This indicates the cluster is very thin (possibly only one layer thick) and its packing filling factor ϕ_p can be determined as the ratio between the area covered by aggregates to the total area of the cluster (see Figure 6.7). For this cluster, the packing filling factor is $\phi_p = 0.9123$. As the densest packing of circles on a surface is reached for hexagonal packing, where $\phi_p = 0.9069$, it seems an appropriate approximation to assume that the clusters growing on the wall during the SPACE experiment had a thickness of about one monomer. Thus, the quantity

$$\sigma_{\text{cross}}(t)n'(t) = \frac{4r}{V} \cdot \sum_{k=0}^{N(t)} R_k(t)\tag{6.6}$$

can be measured from the analysis of clusters growing on the wall during the SPACE experiment (see Section 6.2.2). Finally, the sticking probability can be calculated as

$$\beta(t) = -\frac{1}{n(t)} \cdot \frac{dn(t)}{dt} \cdot \frac{1}{\sigma_{\text{cross}}(t)n'(t)v(t)}\tag{6.7}$$

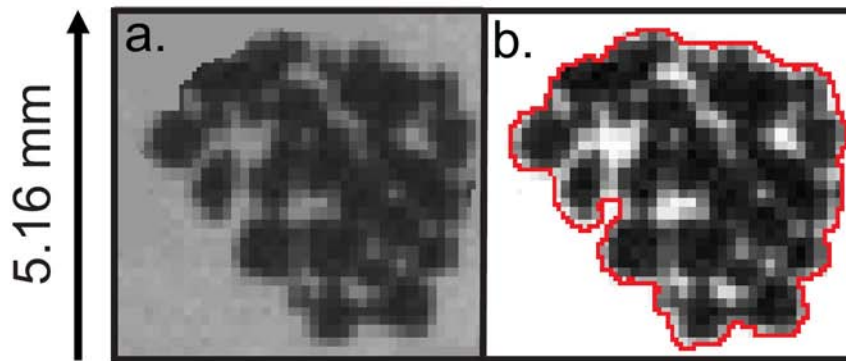


Figure 6.7: Typical wall cluster during the REXUS flight experiment from the large size distribution of aggregates composed of monodisperse dust. a: Original grayscale image b: Contrast enhanced image. The red line indicates the delimitation of the total cluster area. The packing filling factor $\phi_p = 0.9123$ is determined by dividing the dark area by the area enclosed by the red line.

The resulting sticking probability between the monomer aggregates and the clusters on the cell walls calculated with equation 6.7 is plotted according to the collision velocity and for all three aggregate types in Figure 6.8. During the growth phases of cycles 1 and 3, the sticking probability was very close to 0. Accordingly, only the sticking probability during the growth phase of cycle 2 is shown. The curves that can be distinguished growing in sticking probability with decreasing impact velocity are for the three different dust types during the growth phase of cycle 2. For a certain velocity, the sticking probability of the dust aggregates rised very steeply and approached unity. At this point, no free-flying aggregates were left in the cell volume. This velocity was determined from the data as the maximum velocity at which all aggregates were incorporated in clusters, leaving none free-flying in the cell volume. Table 6.2 lists the determined values for all three types of aggregates investigated. Both the larger distributions of aggregates composed of mono and polydisperse SiO_2 showed perfect sticking for similar velocities of 11.1 and 11.3 cm s^{-1} , respectively, while the smaller distribution of aggregates composed of monodisperse SiO_2 stuck perfectly for 12.3 cm s^{-1} . The minimum velocity for which $\beta < 0.05$ was also determined: the smaller aggregates composed of monodisperse dust reached $\beta = 0.05$ at a mean collision velocity of 13.0 cm s^{-1} and the larger aggregates composed of mono- and polydisperse dust reached $\beta = 0.05$ at 11.8 and 12.2 cm s^{-1} , respectively.

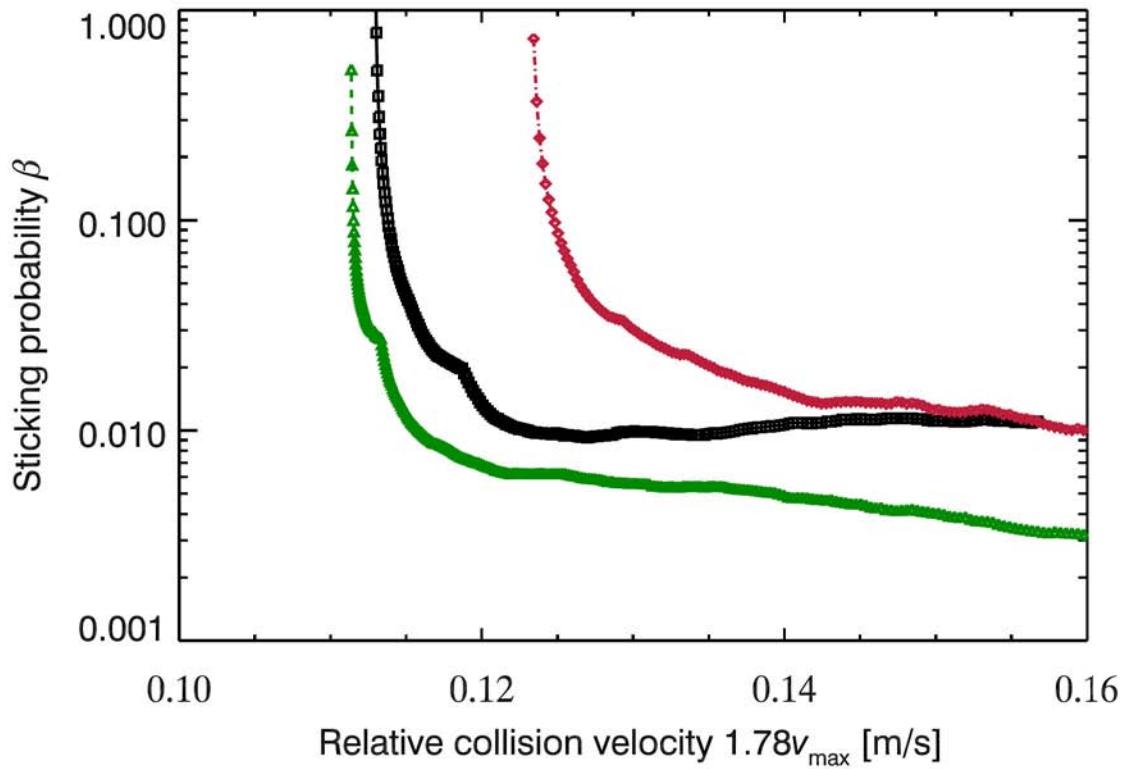


Figure 6.8: Sticking probability of the three types of dust aggregates investigated in the SPACE experiment plotted according to the statistical relative collision velocity computed in Section 5.5.2 ($1.78v_{\max}$): the large size distribution of aggregates composed of poly- and monodisperse dust (black solid line with squares and green dashed line with triangles, respectively) and the small size distribution of aggregates composed of monodisperse dust (red dash-dotted line with diamonds).

Table 6.2: Perfect sticking velocities for all three aggregate types during the SPACE suborbital flight experiment. The velocities for which $\beta > 0.05$ are also listed.

Aggregate type	Velocity for perfect sticking [cm s^{-1}]	Velocity above which $\beta < 0.05$ [cm s^{-1}]
Small aggregates of monodisperse dust	12.3	13.0
Large aggregates of monodisperse dust	11.1	11.8
Large aggregates of polydisperse dust	11.3	12.2

6.2.4 Aggregate pull-off forces

By analyzing the evolution of the clusters on the experiment cell walls during the fragmentation phases (17 to 32 s, 62 to 76 s and 112 to 132 s, see Figure 3.5 and Table 3.3), it was possible to determine the reduced cluster fragmentation rate

$$f_r = -\frac{1}{n(t)} \cdot \frac{dn}{dt} \quad (6.8)$$

where $n(t)$ is the number density of aggregates incorporated in clusters on the cell walls determined in Section 6.2.2.

Figure 6.9 shows this reduced fragmentation rate in dependency of the centrifugal acceleration induced by the cell wall rotation during the second shaking cycle. The curves are terminated at the acceleration where they reach the saturation of free-flying aggregates in the cell volume. This saturation was reached when the number density of free-flying aggregates in the cell did not increase anymore with increasing centrifugal acceleration. The reduced fragmentation rate increased with increasing centrifugal acceleration indicating that more and more aggregates were pulled off clusters on the wall. The maxima of these reduced fragmentation rates indicate the acceleration at which most of the aggregates composing the clusters on the cell walls were pulled off their parent cluster and allow for a determination of a pull-off force for each investigated aggregate size and type. For the smaller aggregates composed of monodisperse dust, the linear wall acceleration at maximum fragmentation was $a_c = 16.62 \text{ m s}^{-2}$. The corresponding pull-off force

$$F_{po} = ma_c \quad (6.9)$$

where m is the mass of the aggregate pulled off the cluster, was $1.43 \times 10^{-8} \text{ N}$ (Table 6.3). For the larger aggregates composed of mono- and polydisperse dust, the accelerations at maximum fragmentation were $a_c = 9.78 \text{ m s}^{-2}$ and 9.07 m s^{-2} , which corresponds to pull-off forces of $F_{po} = 1.87 \times 10^{-7} \text{ N}$ and $1.26 \times 10^{-7} \text{ N}$, respectively.

To verify whether the calculated pull-off forces are valid, the number of monomer aggregates each cluster lost per frame during the fragmentation phase was determined. The result of this investigation is shown in Figure 6.10. During the fragmentation phase, the shaking frequency of the experiment cells was increased with time, implying an increasing centrifugal acceleration on the external aggregate layer of clusters on the wall. At centrifugal accelerations around the values for which the fragmentation rate of clusters reached its maximum ($\sim 63 \text{ s}$ after start of data recording, see Figure 6.10b.), the larger size distribution of aggregates composed of monodisperse dust displayed a clear peak of single monomer losses. This peak was also visible, although less marked, for the other investigated dust types. The aggregates composed of polydisperse dust lost up to 0.4 monomers per cluster and per frame at $\sim 65 \text{ s}$ (Figure 6.10c.), meaning that not all clusters lost monomers at the same time. The small aggregates composed of monodisperse SiO_2 , however, lost up to about 4 monomers per cluster per frame at $\sim 62 \text{ s}$ (Figure 6.10a.). This lead to the conclusion that the small aggregates were pulled off the clusters on the cell walls in groups of 4 instead of individually. The corrected aggregate radius and pull-off forces are listed in the last row of Table 6.3. As for the same wall acceleration, the aggregates pulled off the clusters were four times larger in surface, the force required to pull them off was about one order of magnitude higher than for single aggregates.

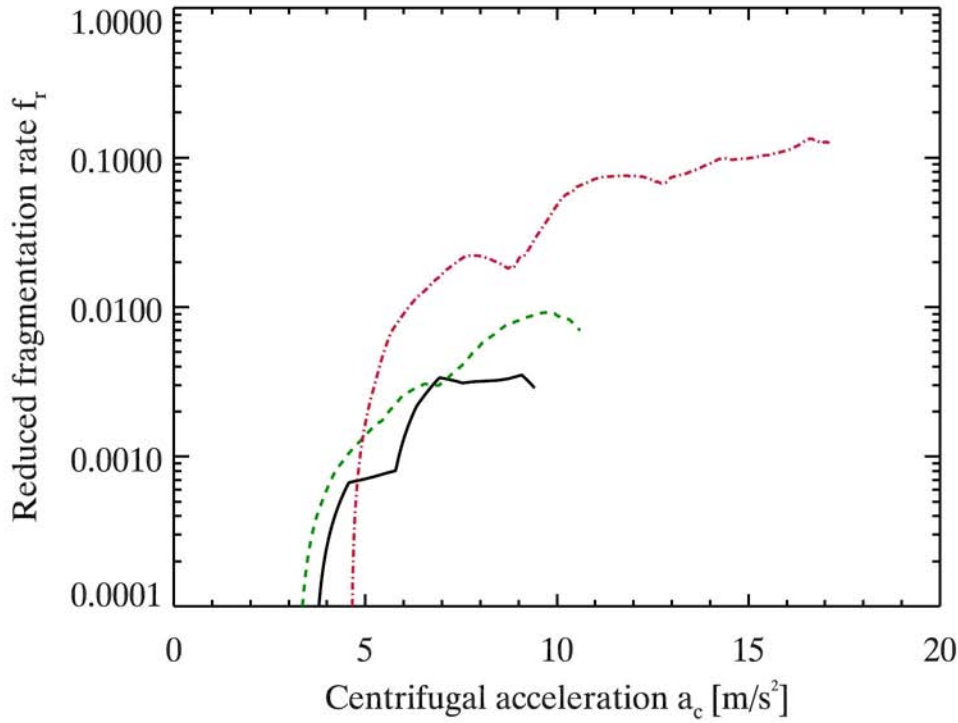


Figure 6.9: Reduced fragmentation rate of the clusters on the cell walls during the fragmentation phase of the second shaking cycle for the smaller and larger size distributions of aggregates composed of monodisperse SiO₂ (red dash-dotted and green dashed line, respectively) and the larger size distribution of aggregates composed of polydisperse SiO₂ (black solid line), plotted according to the centrifugal acceleration induced on the aggregates by the cell wall rotation. The curves are terminated at the acceleration where they reach the saturation of free-flying aggregates in the cell volume.

Table 6.3: Accelerations at maximum fragmentation rate and pull-off forces F_{po} for the three investigated types of dust. The corresponding tensile strengths $T_s = F_{po}/(\pi r_{agg})^2$ are listed in the last column (see Section 7.2.2).

Aggregate type	Monomer aggregate radius r_{agg} [m]	Acceleration at maximum fragmentation rate [m s ⁻²]	Pull-off force F_{po} [N]	Tensile strength T_s [Pa]
Small aggregates of monodisperse dust	6.00×10^{-5}	16.62	1.43×10^{-8}	1.27
Large aggregates of monodisperse dust	1.67×10^{-4}	9.78	1.87×10^{-7}	2.09
Large aggregates of polydisperse dust	1.65×10^{-4}	9.07	1.26×10^{-7}	1.48
Agglomerates of 4 aggregates of monodisperse dust	1.20×10^{-4}	16.62	1.15×10^{-7}	2.55

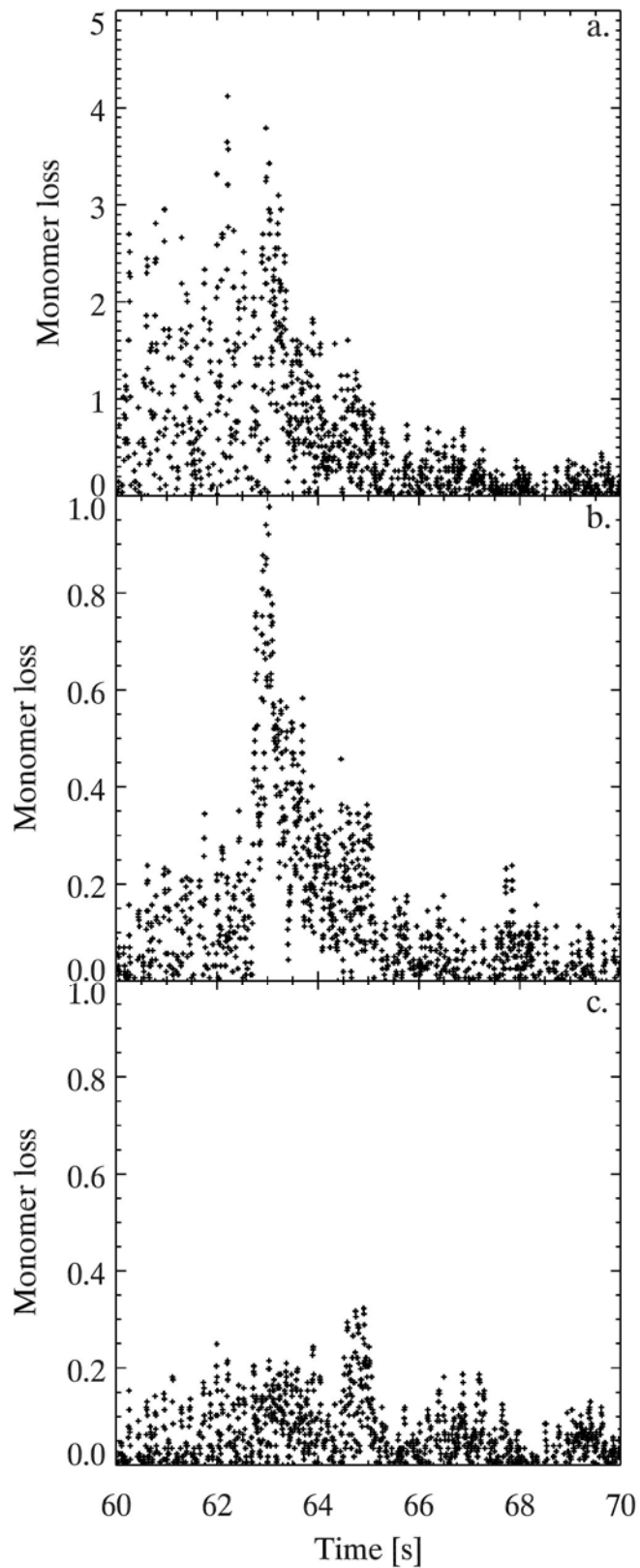


Figure 6.10: Monomer aggregate loss per cluster per frame for clusters on the cell walls during the fragmentation phase of the second shaking cycle for the three dust types investigated: a. the small size distribution of aggregates composed of monodisperse SiO_2 , b. the large size distribution of aggregates composed of monodisperse SiO_2 and c. the large size distribution of aggregates composed of polydisperse SiO_2 .

7 Sub-millimeter sized dust aggregates: collision behavior and cluster properties

The results from the different SPACE experiment runs can be used to draw conclusions on the collision behavior of sub-mm-sized SiO₂ aggregates and on properties of the clusters formed by these collisions. When compared with current disk models, some predictions on aggregate and cluster behavior in the protoplanetary nebula can be inferred.

7.1 Inputs to the dust collision model

The results for collisions between aggregates obtained in the different SPACE experiments are summarized in Figure 7.1. Drop tower collisions are plotted as single points (the symbols for each dust type are listed in Table 6.1). For each collision, the mass of the smaller collision partner is plotted. The REXUS flight results are represented by boxes as the collision probability between aggregates with a certain size distribution (box height) could continuously be measured while reducing the mean relative collision velocity (box width). The height of the boxes was chosen such as to represent the initial size distributions of aggregates inserted into the experiment cells ($\sim 8 \times 10^{-7}$ g for the small size distribution and $\sim 1.5 \times 10^{-5}$ g for the larger size distributions) at 50 % of the respective distribution maximum (see Figure 4.2). The width of the boxes corresponds to the relative velocity range over which the sticking probability was measured. The velocities for start of sticking (sticking probability $\beta > 0.05$) and for perfect sticking ($\beta \simeq 1$) listed in Table 6.2 are added to the boxes (intermediate dotted lines). As the larger aggregates composed of mono- and polydisperse dust had very similar sticking velocities, only the results for the monodisperse collisions were plotted (upper box). The dust collision model developed by Güttler et al. (2010) and Kothe et al. (2013) is displayed in the background, delimiting the regions of the parameter field where sticking (green), bouncing (yellow) and fragmentation (red) are expected for same-sized dust aggregate collisions.

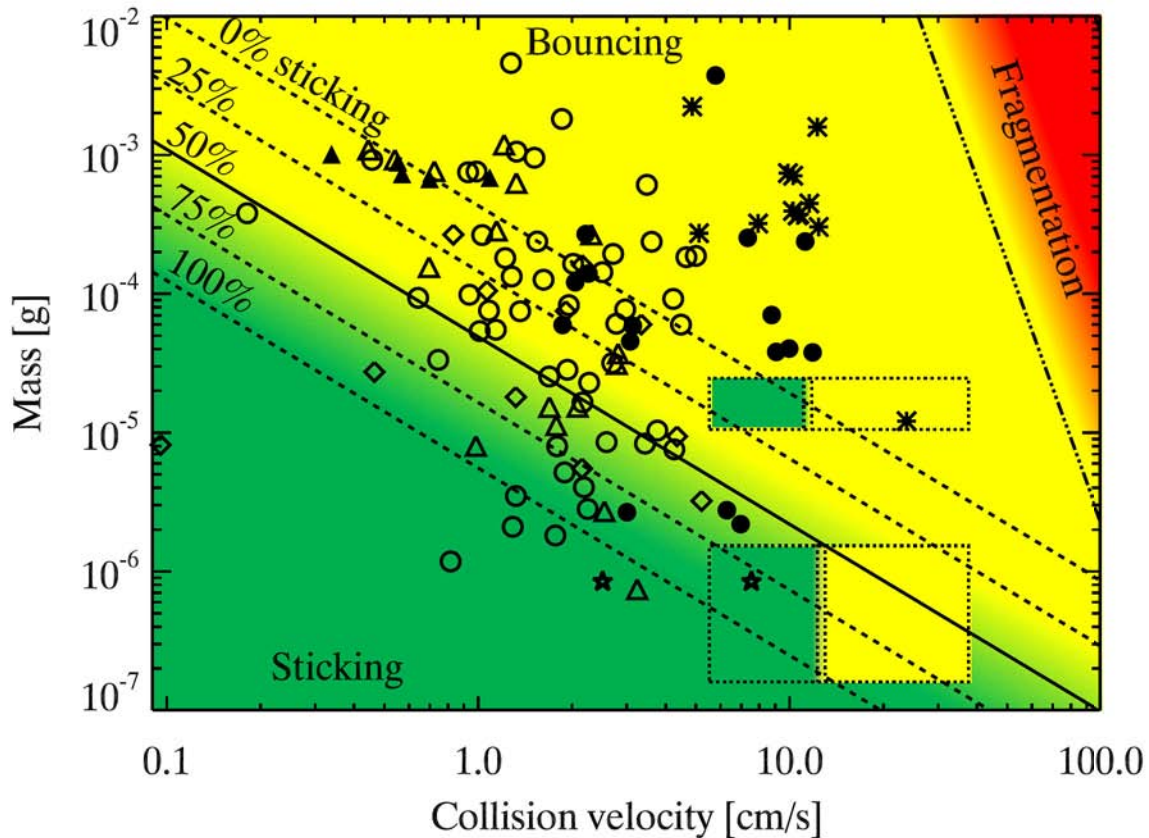


Figure 7.1: Compiled results of the different SPACE experiments with the drop tower collisions (individual points) and the REXUS flight results (dotted boxes). As the larger aggregates composed of mono- and polydisperse SiO_2 had very similar sticking velocities, only the results for the aggregates composed of monodisperse SiO_2 are plotted (upper box). The symbols corresponding to the types of dust investigated are explained in Table 6.1. Open symbols represent sticking collisions and filled symbols bouncing. The asterisks represent fragmentation of aggregates composed of monodisperse SiO_2 . The data points deduced from non-agglomerating aggregates composed of irregular polydisperse SiO_2 (Sigma-Aldrich) are represented by stars. The background colors correspond to the dust collision model developed by Güttler et al. (2010): green for sticking collisions, yellow for bouncing and red for fragmentation. The lines represent the limits between sticking and bouncing (solid line for a 50% sticking probability, dashed lines for 0, 25, 75 and 100 % probabilities) and bouncing and fragmentation (dash-dotted line for the onset of fragmentation), computed by Kothe et al. (2014).

7.1.1 The sticking to bouncing transition

The overall tendency for collisions between aggregates to be less likely to lead to aggregate sticking, the bigger and the faster these aggregates are, can be recognized in the gathered data. The mean relative velocity and reduced aggregate mass for sticking collisions during drop tower experiments are 1.97 cm s^{-1} and $2.8 \times 10^{-4} \text{ g}$, respectively, in contrast to 3.66 cm s^{-1} and $4.14 \times 10^{-4} \text{ g}$ for the bouncing collisions (see Table 7.1). The suborbital flight experiment run data was in general concurrence with this tendency as well (see Table 6.2). The smaller size distribution started sticking at higher velocities than the bigger ones (13.6 cm s^{-1} instead of 12.4 cm s^{-1}).

Table 7.1: Mean relative velocity and reduced mass for all collisions observed during the drop tower experiment run according to their collision outcomes.

Collision outcome	Relative velocity (cm s ⁻¹)	Reduced mass (g)
sticking	1.97	2.8×10^{-4}
bouncing	3.66	4.14×10^{-4}
fragmentation	10.8	4.5×10^{-4}

However, it is obvious that many sticking collisions were taking place in parameter ranges where bouncing would be expected in the current model. One explanation for this collision behavior is the fact that most of the observed events were not aggregate-aggregate collisions, for which the model was developed, but aggregate-cluster or cluster-cluster collisions. To illustrate this, Figure 7.2 plots both aggregate/cluster masses for each collision observed, for sticking collisions (a) and bouncing and fragmenting collisions (b). During the suborbital flight experiment the collision properties of the free-flying aggregates with clusters on the cell wall were measured in a continuous manner. They are represented by striped boxes. These boxes span the initial size distributions of aggregates inserted into the experiment cells (same values as in Figure 6.1) and their length reaches from monomer aggregate to cluster sizes. The represented cluster sizes of 1.0×10^{-2} g and 5.0×10^{-2} g for the smaller and larger aggregate size distributions, respectively, were the mean measured sizes of clusters on the experiment cell walls during the slow shaking phases of the suborbital flight. Most of the sticking collisions observed during the drop tower experiments did not involve monomer aggregates ($\sim 8 \times 10^{-7}$ g), but clusters of $> 10^{-4}$ g in mass, composed of more than 100 monomer aggregates. The enhanced sticking probability of clusters composed of a high number of aggregates was also observed by Kothe et al. (2014), compared with the results of Weidling et al. (2012) who analyzed aggregates of 10^{-4} g to 10^{-3} g in mass that resulted in bouncing for more than 90 % of the collisions at velocities between about 0.2 and 50 cm s⁻¹.

In Figure 7.2 it can also be seen that the mass ratio between colliding aggregates in the different SPACE experiment runs covers up to 4 orders of magnitude. At the highest mass ratio of $\sim 10^4$, only sticking collisions were observed. The highest mass ratio between aggregates involved in a bouncing or fragmenting collision is about 10^2 .

The coexistence of sticking and bouncing collisions in a region of the parameter field along the transition line has also been observed by Weidling et al. (2012) and Kothe et al. (2013). However, the rocket flight data displayed a very sharp transition from one regime to another. This could be attributed to the statistical nature of the measurement: as the collision outcomes were averaged over a high number of collisions, the transition appeared sharper than for the individual collisions observed in the drop tower experiments.

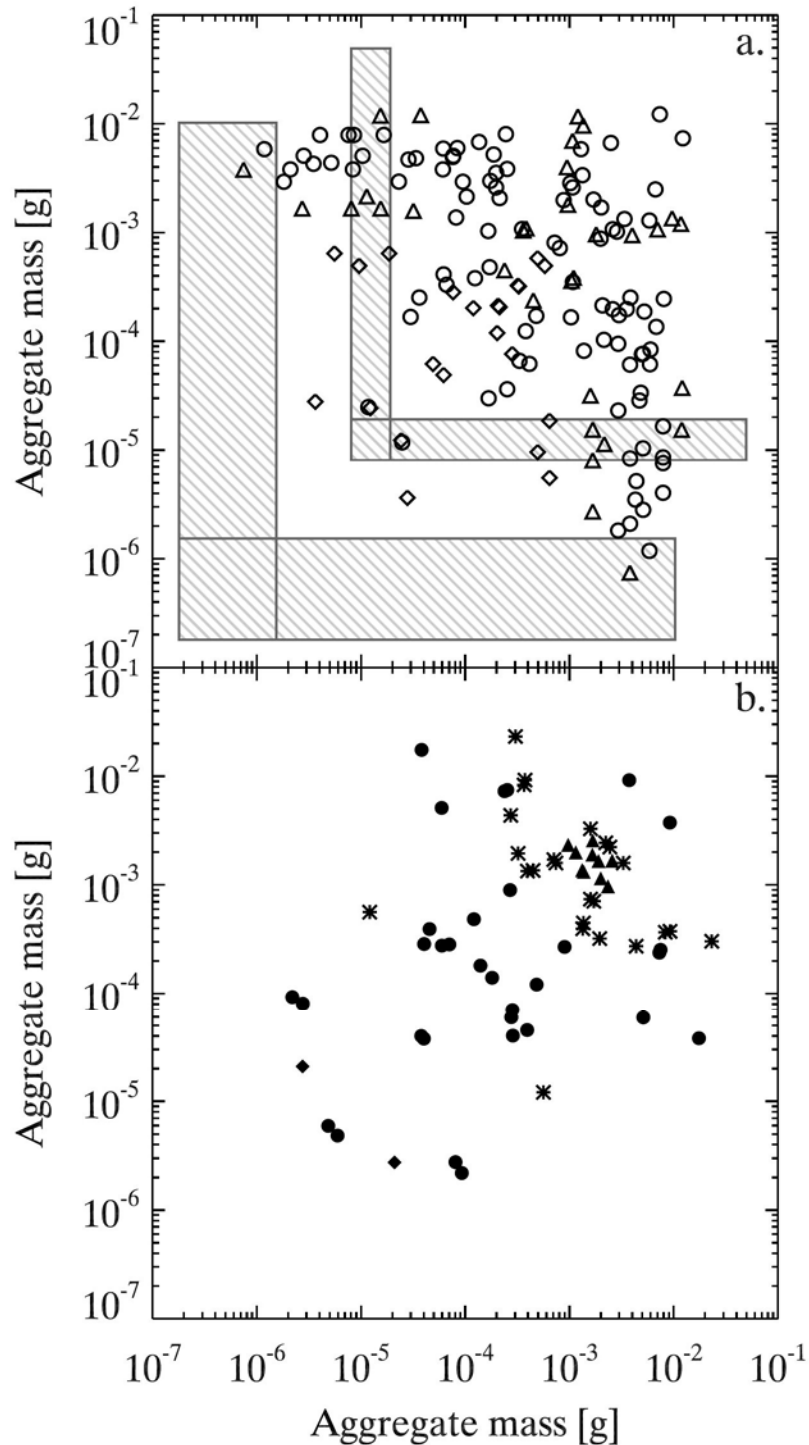


Figure 7.2: Masses of aggregates involved in collisions observed in the SPACE experiment: a. drop tower and REXUS flight sticking collisions. Drop tower collisions are plotted with the symbols of Table 6.1. The REXUS flight size distributions are plotted as striped boxes. These boxes span the initial size distributions of aggregates inserted into the experiment cells (same values as in Figure 6.1) and their length reaches from monomer aggregate sizes to the mean size of clusters during slow shaking phases. b. drop tower bouncing (filled symbols) and fragmentating (asterisks) collisions. In both plots, each collision is represented twice (symmetrically with respect to the diagonal). The sticking collisions were separated from the others for better legibility.

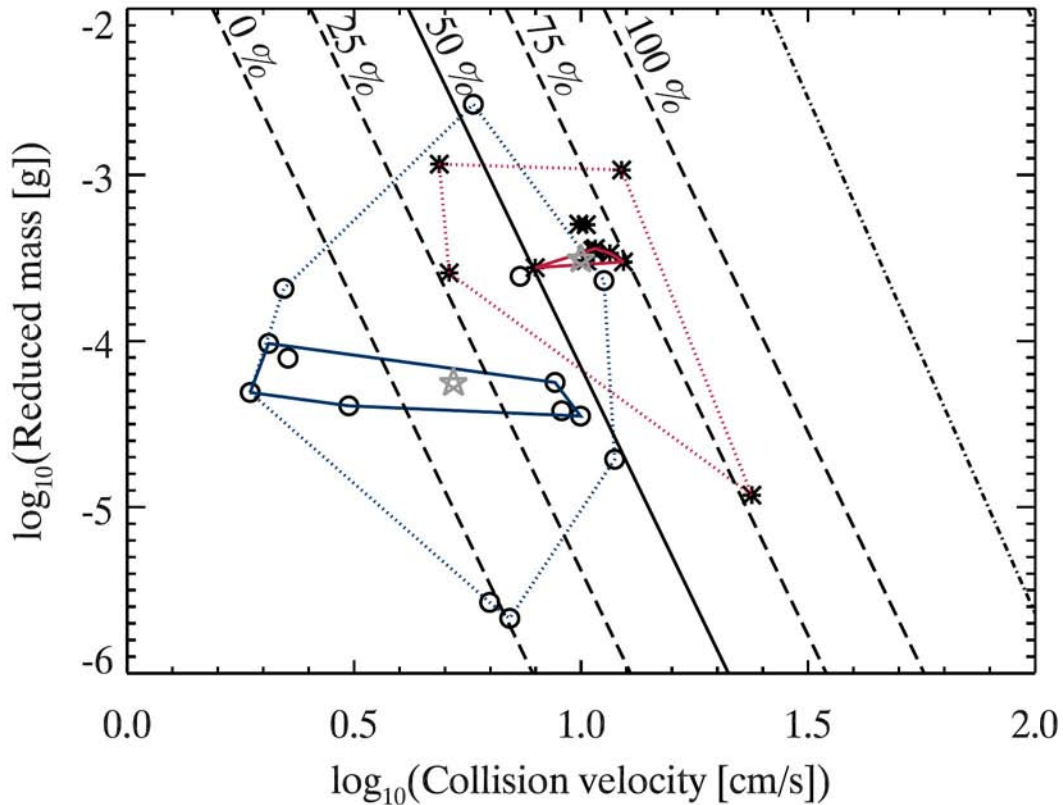


Figure 7.3: Transition between bouncing (circles, blue) and fragmentation (asterisks, red) for $\sim 120 \mu\text{m}$ sized aggregates composed of monodisperse SiO_2 . As this was the only aggregate type that displayed fragmentation upon collision, no other aggregate types are plotted here. The mean of each set of data points are marked by the grey stars. The solid contours enclose 50 % of the respective data points around their mean value and the dotted contours, 100 %. The solid black line marks the computed 50 % transition between bouncing and fragmentation, and the dashed lines the corresponding 0, 25, 75 and 100 % probability for fragmentation. The dash-dotted line on the right side of the plot represents the fragmentation onset in the collision model of Kothe et al. (2014).

7.1.2 The bouncing to fragmentation transition

As can be seen in Figure 6.1 (asterisks), the fragmenting collisions (observed only between non-compacted aggregates composed of monodisperse SiO_2) happened at masses and velocities where bouncing would be expected in the dust collision model (Güttler et al. 2010, Kothe et al. 2013). For non-compacted aggregates composed of monodisperse dust, collisions leading to bouncing had a mean collision velocity of 3.14 cm s^{-1} and a reduced mass of $4.35 \times 10^{-4} \text{ g}$. Collisions leading to fragmentation of the cluster had a mean collision velocity and reduced mass of 10.8 cm s^{-1} and $4.5 \times 10^{-4} \text{ g}$, respectively (Table 7.3). These values confirm the general trend of aggregate collisions to transit from bouncing to fragmentation with growing aggregate masses and relative velocities. Figure 7.3 plots the bouncing (circles) and fragmentation (asterisks) collisions for aggregates composed of monodisperse SiO_2 according to the collision velocity and reduced mass, together with the respective mean values (grey stars). Also shown are the contours of 50 and 100 %

occurrence of bouncing and fragmentation (solid and dotted contours around the mean values, respectively, blue for bouncing and red for fragmentation).

A transition between bouncing and fragmentation was computed with the method presented in Kothe et al. (2013). For this transition, a power law relation was assumed, of the form

$$\frac{m}{1 \text{ g}} = 10^a \left(\frac{v}{1 \text{ cm s}^{-1}} \right)^b \quad (7.1)$$

with m being the mass of the smaller aggregate, v the relative collision velocity and a , b the fit parameters. Three fitting methods were applied to the available set of bouncing and fragmentation data points: least squares, least linear and least number of data points deviation, with both asymmetric and symmetric false data point discrimination. This resulted in six fits optimized by different criteria. The method of conditional value at risk (CoVar, Hull 2012) was used to choose the best fit out of these six sets of values (see Kothe et al. 2013, for details). The best fit was reached for the least squares deviation method with an asymmetric false data point discrimination, and the parameters $a = 1.51$ and $b = -5.67$. This fit is also represented in Figure 7.3 (solid black line). The difference between the measured collision velocities and this computed transition allow for the determination of a fragmentation probability centered around the transition line (method used in Kothe et al. 2013). The 0, 25, 75 and 100 % fragmentation probability limits are also plotted in Figure 7.3 (dashed lines).

The computed transition has an offset of a factor of 6 in velocity compared with the transition line computed by Kothe et al. (2014) (dash-dotted line on the right side of Figure 7.3). This difference can be attributed to the nature of the aggregates observed. To compute the transition between bouncing and fragmentation, Kothe et al. (2014) used collision data gathered by Blum & Münch (1993), Beitz et al. (2011), Deckers & Teiser (2013) and Schräpler et al. (2013). All of these experiments were performed with aggregates prepared in the laboratory that had a 2D fractal dimension of 2. The aggregates that were seen to be fragmenting during the drop tower experiments, however, were clusters built during the microgravity phase of the experiment, that had a mean fractal dimension of 1.70. This lower fractal dimension made them much more fragile.

7.2 Properties of clusters composed of sub-mm-sized aggregates

In this section, the clusters built during the growth phases of the different SPACE experiment runs are investigated and some of their properties derived. First, their fractal dimensions are discussed (Section 7.2.1). Then, their inner cohesion is studied by investigating the tensile strength (Section 7.2.2) and surface energy of their sub-mm-sized constituents (Section 7.2.3). Finally, the adaptation of a collision recipe (Dominik & Tielens 1997) to the aggregates investigated with the SPACE experiment yielded the derivation of contact rolling and breaking threshold energies (Section 7.2.4).

7.2.1 Cluster fractal dimensions

The fractal dimensions of the clusters that formed in the drop tower experiments were determined in Section 6.1.3. The obtained values ranged from 1.53 to 1.94 with a mean value of 1.70 and were in good agreement with the values determined by Kothe et al. (2013) for similar aggregates (they determined a mean fractal dimension of 1.63). As mentioned by them, the method applied to the type of data analyzed here (512×512 px frames) seems to underestimate the real 2D fractal dimension by up to 0.1. Furthermore, the determination of the aggregate 3D fractal dimension based on 2D frames is subjected to a systematic error (see Hunt & Kolushin 1997, Falconer 2003, Sanchez et al. 2005). This implies that a more exact value for the fractal dimensions of the aggregates investigated here would be around 1.90 instead of 1.70 (see Figure 6 in Sanchez et al. 2005).

For non-compacted aggregates composed of monodisperse SiO₂, there is a clear trend of a decrease of the highest fractal dimensions (from 1.94 to 1.71) with increasing aggregate size (0.30 to 1.57 mm, see Figure 6.4-1,2), independent from the absolute values. This indicates that clusters became more fractal as they grew.

The minimum fractal dimension reached for bigger clusters was 1.65, which is compatible with hit-and-stick cluster-cluster growth (Blum et al. 1999, Krause & Blum 2004, Paszun & Dominik 2006). On the other hand, the lowest computed fractal dimensions seem to increase slightly with increasing cluster size (see Figure 6.4-3,4). This could be attributed to the frequent collisions of such clusters with the cell walls, that were usually energetic enough to trigger local restructuring. These wall collisions tended to increase the cluster fractal dimension.

7.2.2 Tensile strength of aggregates at the surface of clusters

The pull-off forces needed to detach a monomer aggregate (~100 μm in size) from a wall cluster built during the slow shaking phase of the suborbital flight experiment are listed in Table 6.3. From these pull-off forces, the corresponding tensile strength of clusters composed of monomer aggregates could be determined by $T = F_{po}/\sigma_{agg}$, with F_{po} being the pull-off force needed to detach an aggregate from the cluster and σ_{agg} the cross section of this detaching aggregate. The values obtained were 2.09 Pa and 1.48 Pa for the larger size distributions of aggregates composed of mono- and polydisperse dust, respectively. The tensile strength of agglomerates of four monomer aggregates composed of monodisperse dust was 2.55 (see Section 6.2.4 for details).

Figure 7.4 plots these three values of the tensile strength according to the size of the detaching aggregates (diamonds and triangle for aggregates composed of mono- and polydisperse SiO₂, respectively). As the experiment flew only one size distribution of aggregates composed of polydisperse dust, only one data point (triangle) could be measured. The lines show the predicted values of the tensile strength of aggregates at the surface of the clusters they compose, by the model presented in Skorov & Blum (2012). This model results in a tensile strength for clusters composed of dust aggregates of radius r of

$$T = T_1 \phi \left(\frac{r}{1 \text{ mm}} \right)^{-\frac{2}{3}}, \quad (7.2)$$

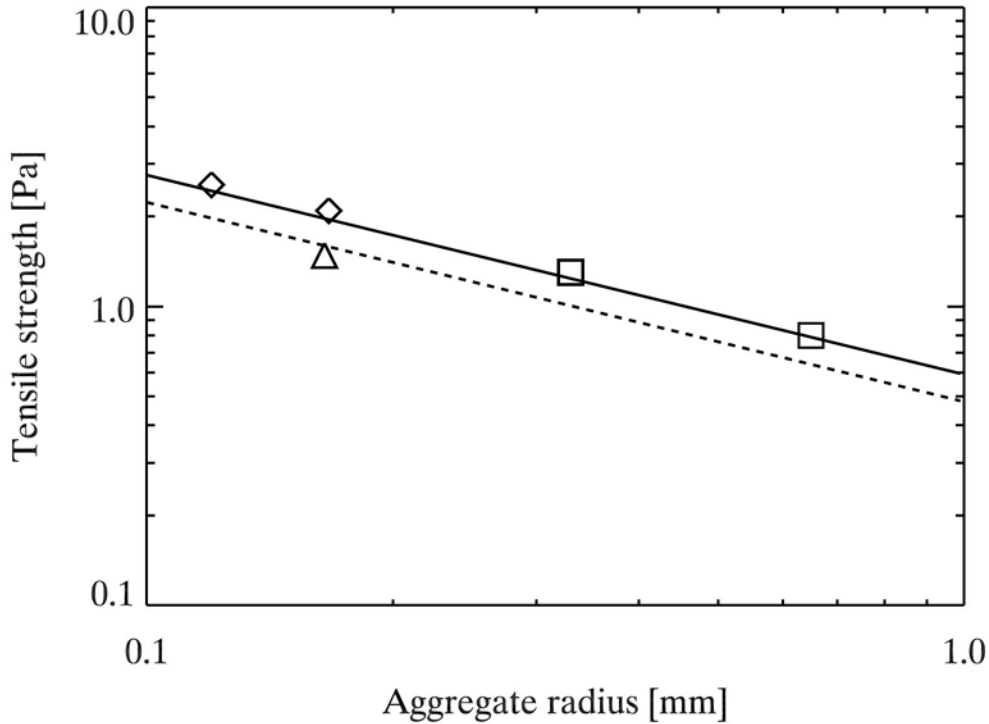


Figure 7.4: Tensile strength of the aggregates investigated in the SPACE suborbital flight experiment for aggregates composed of mono- and polydisperse dust (diamonds and triangle, respectively), compared with data from Blum et al. (2014) (squares) and the model prediction by Skorov & Blum (2012). This model is applied for an aggregate porosity of 0.3 (dashed line) and 0.37 (solid line).

where $T_1 = 1.6$ Pa and ϕ is the porosity of the aggregate. In Figure 7.4, the dashed line is the tensile strength computed for an aggregate porosity of 0.3, as used by Skorov & Blum (2012) and the solid line for a porosity of 0.37 for the aggregates used in the SPACE experiment (see Section 4.3). The data from the SPACE experiment is in very good agreement with the prediction of Skorov & Blum (2012). Furthermore, the experiment presented in Blum et al. (2014) also measured the tensile strength of SiO_2 aggregates on the surface layer of the clusters they compose, for aggregate sizes of 0.6 and 1.2 mm in diameter. Their results are plotted in Figure 7.4 (squares) and are in agreement with both the model by Skorov & Blum (2012) and the SPACE experiment data. The concurrence of the theoretical model by Skorov & Blum (2012) with the results of two independent experimental methods, as well as observed sizes of released aggregates for cometary nuclei (e.g. Moreno et al. 2012, 2013) suggests that the surface of these nuclei are loosely bound conglomerates of dust and ice aggregates, most probably formed by gravitational instability in the early stages of the Solar System formation (Blum et al. 2014).

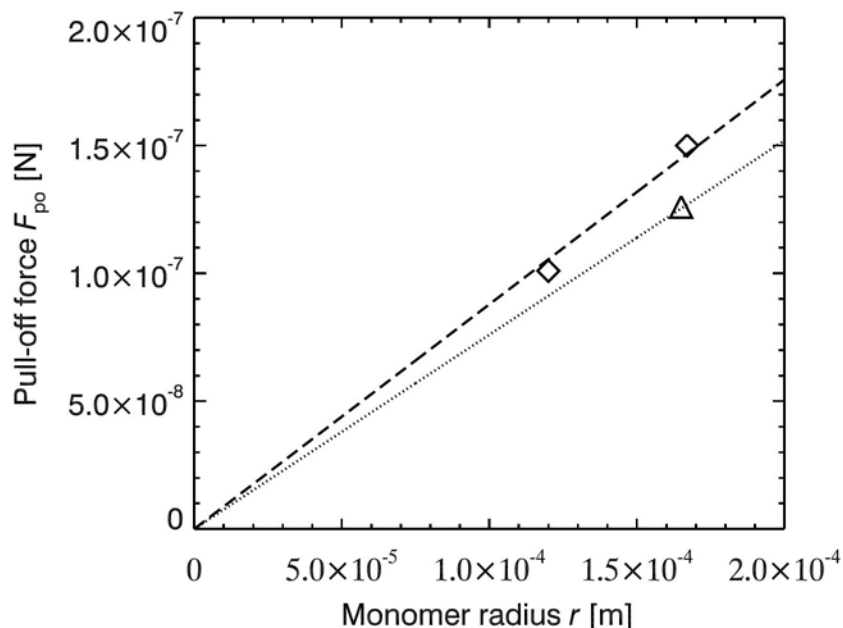


Figure 7.5: Aggregate pull-off forces according to their sizes, for the types of dust investigated in the SPACE suborbital flight experiment: monodisperse (diamonds) and polydisperse SiO_2 (triangle). The corresponding linear fits passing through the origin are shown too, with slopes of $8.79 \times 10^{-5} \text{ N m}^{-1}$ (dashed line) and $7.6 \times 10^{-5} \text{ N m}^{-1}$ (dotted line) for both dust types, respectively. The smaller aggregates composed of monodisperse dust were assumed to detach in clumps of four aggregates.

7.2.3 Estimation of the surface energy of sub-mm-sized aggregates

The pull-off forces listed in Table 6.3 are plotted in Figure 7.5 according to the monomer aggregate size. For the smaller size distribution of aggregates composed of monodisperse dust, the detaching of agglomerates of four aggregates was assumed, as described in Section 6.2.4. The Johnson-Kendall-Roberts theory (Johnson et al. 1971) for the contact between soft spheres predicts the relationship

$$F_{\text{po}} = 3\pi\gamma r \quad (7.3)$$

between the pull-off force F_{po} of one sphere from another and their radius r . γ is the surface energy of the contact between the two spheres. Although this applies to perfect, soft spheres, it has been observed to be valid for μm -sized SiO_2 particles (Heim et al. 1999). If this relationship is assumed to be also valid for the monomer aggregates investigated by the SPACE experiment (mean sizes of ~ 120 and $\sim 330 \mu\text{m}$ in diameter), an effective surface energy γ_{eff} , for which $F_{\text{po}} = 3\pi\gamma_{\text{eff}}r$ can be introduced, as done in Weidling et al. (2012). Following their method, the effective surface energy can be scaled to the surface energy γ of the constituent monomer particles ($\sim 1 \mu\text{m}$ in size) via the aggregate porosity ϕ and the Hertz factor a^2/a_0^2 , where a_0 is the radius of such a monomer particle ($\sim 0.5 \mu\text{m}$) and a is the radius of the contact surface between two such monomer particles. This scaled effective surface energy can be written as:

$$\gamma_{\text{eff}} = 2N\gamma\phi\frac{a^2}{a_0^2} \quad (7.4)$$

Table 7.2: Effective surface energies for the dust investigated in the SPACE rocket flight experiment.

Aggregate type	Measured effective surface energy [J m ⁻²]	Measured effective surface energy for one contact [J m ⁻²]	Measured surface energy scaled down to a monomer particle [J m ⁻²]
Aggregates composed of monodisperse dust	9.3×10 ⁻⁵	1.9×10 ⁻⁵	2.2×10 ⁻²
Aggregates composed of polydisperse dust	8.1×10 ⁻⁵	1.6×10 ⁻⁵	1.8×10 ⁻²

where N is the number of connecting surfaces from the aggregate to the cluster. The factor 2 comes from the fact that two sticking aggregates each have a surface energy of γ . As derived from Johnson et al. (1971) (Weidling et al. 2012),

$$\frac{a^2}{a_0^2} = \left(\frac{9\pi\gamma(1-\nu^2)}{a_0 E_0} \right)^{\frac{2}{3}}, \quad (7.5)$$

where E_0 and ν are the monomer particles Young's modulus and Poisson number, respectively. Therefore,

$$\gamma = \left(\frac{\gamma_{\text{eff}}}{2 N \phi \left(\frac{9\pi(1-\nu^2)}{a_0 E_0} \right)^{\frac{2}{3}}} \right)^{\frac{3}{2}}. \quad (7.6)$$

For the SiO₂ dust used in the SPACE experiment, $\nu = 0.17$, $E_0 = 5.4 \times 10^{10}$ Pa, $a_0 = 7.6 \times 10^{-7}$ m and $\phi = 0.37$ (see Table 4.1). The number of connecting surfaces was determined from a typical cluster (Figure 6.7) to be 2.5. In this cluster, each border aggregate had between 2 and 3 neighbors.

The effective surface energy γ_{eff} was measured from the SPACE suborbital flight data, to be 9.3×10^{-5} J m⁻² and 8.1×10^{-5} J m⁻² for aggregates composed of mono- and polydisperse dust, respectively (Figure 7.5 and Table 7.2). For these values, the surface energy of a monomer particle ($\sim 1 \mu\text{m}$) was calculated to be $\gamma = 21.8$ mJ m⁻² for the monodisperse and 18.0 mJ m⁻² for the polydisperse SiO₂ particles.

These values are in very good agreement with 25 mJ m⁻² measured for silica powder by Kendall et al. (1987) and 18.6 mJ m⁻² measured for $\sim 1 \mu\text{m}$ SiO₂ particles by Heim et al. (1999). This confirms the validity of the scaling model developed in Weidling et al. (2012). It also indicates that the collision behavior of macroscopic ($\sim 100 \mu\text{m}$) aggregates is comparable to the behavior of μm -sized particles. This possible scaling from particles to aggregates could be used in molecular dynamics simulations to investigate clusters composed of 100 μm -sized aggregates. Furthermore, it seems reasonable to try to adapt a collision recipe developed for clusters composed of μm -sized particles (Dominik & Tielens 1997) to clusters composed of $\sim 100 \mu\text{m}$ -sized aggregates.

7.2.4 Collision recipe for clusters composed of sub-mm-sized aggregates

The collisions between clusters and the cell walls during the drop tower experiment runs led to bouncing, with or without visible restructuring, or to fragmentation of the clusters. These clusters were composed of aggregates of about $120 \mu\text{m}$ in diameter, but displayed a collision behavior very similar to those in molecular dynamics simulations where the clusters composed of sub- μm -sized monomer particles (e.g. Dominik & Tielens 1997, Wada et al. 2009). As mentioned in Section 7.2.3, the possibility to scale the surface energy of μm -sized particles to macroscopic ($\sim 100 \mu\text{m}$) aggregates indicates that these simulated collision behaviors could be extended to clusters composed of macroscopic aggregates.

The outcome of simulated collisions between clusters composed of μm particles follows a collision "recipe" introduced by Dominik & Tielens (1997). This recipe defines three threshold energies E_{stick} , E_{roll} and E_{break} and can be summarized in terms of collision energy as follows (see Table 3 of Dominik & Tielens 1997):

- up until a certain collision energy E_{stick} , monomer aggregates always stick to the target cluster they collide with,
- for a collision energy of $5E_{\text{roll}}$, cluster restructuring becomes visible,
- for a collision energy of $3N_c E_{\text{break}}$, clusters start to lose monomer aggregates, where N_c is the number of contacts each monomer particle has to its neighbours inside the cluster,
- for a collision energy of $10N_c E_{\text{break}}$, clusters are disrupted completely.

E_{roll} is the critical rolling energy defined as the energy required to start irreversible rolling of one monomer particle over another. E_{break} is the critical breaking energy and is defined as the energy required to break a contact between two monomer particles. The number of contacts N_c is determined by the coordination number of the aggregates inside a cluster. The clusters in the cell volume grew either through cluster-cluster or through aggregate-cluster collisions, which would both have led to very low coordination numbers of less than 2. However, as they experienced frequent collisions with the cell walls leading to compaction, the choice of a higher coordination number is necessary (random closed packing has a coordination number of 8.4). Aggregates generated by ballistic agglomeration with migration (BAM2, see Shen et al. 2008) have a volume filling factor of ~ 0.4 for a coordination number of 6, which seems appropriate for the clusters studied here. The fractal dimension is chosen to be $D_f = 1.70$ (measured for the aggregates observed in the SPACE experiment in Section 6.1.3). Accordingly, the total number of contacts between aggregates of radius r_0 in a cluster of radius r is

$$N_c = 6 \left(\frac{r}{r_0} \right)^{1.70} \quad (7.7)$$

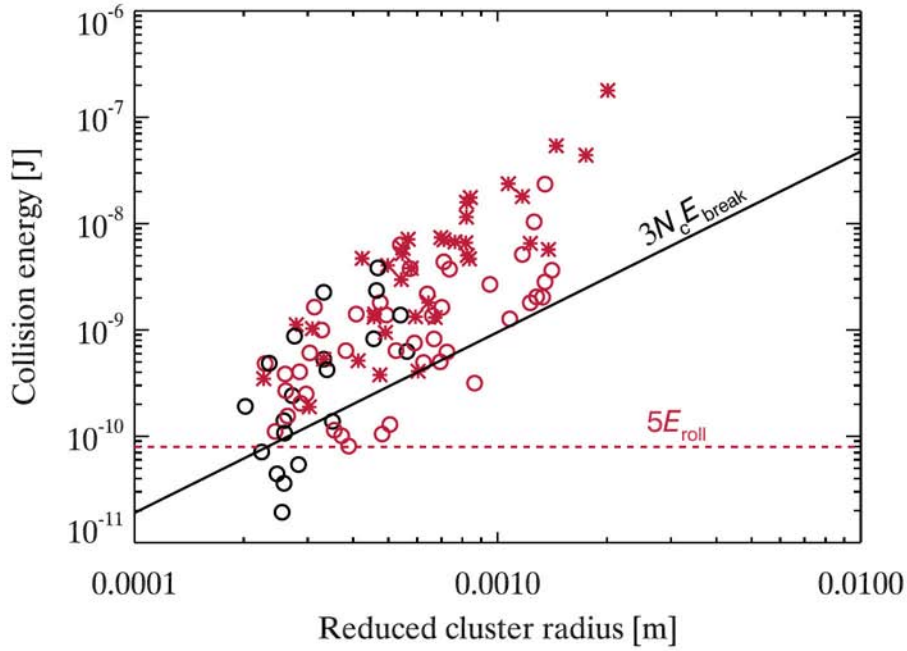


Figure 7.6: Aggregate collisions with the cell walls during the SPACE drop tower experiments, for non-compacted aggregates composed of monodisperse SiO_2 . Circles represent bouncing collisions and asterisks fragmenting of the cluster. Red points show the collisions that displayed visible restructuring. The threshold energies $5E_{\text{roll}}$ for onset of visible restructuring (red dashed line) and $3N_c E_{\text{break}}$ for the loss of the first monomers (solid) are represented.

In the data gathered by the SPACE experiments, aggregate restructuring and fragmentation could be observed directly. Figure 7.6 shows the collisions of clusters with the cell walls during the drop tower experiments according to the collision energy and reduced mass, for non-compacted aggregates composed of monodisperse SiO_2 . The collision energy E_{coll} was approximated to be composed of the translational kinetic energy of the colliding particle system only:

$$E_{\text{coll}} = \frac{1}{2} m_{\text{red}} v_{\text{rel}}^2, \quad (7.8)$$

with m_{red} being the reduced mass of the collision (i.e., the mass of the cluster, as the mass of the wall is considered infinitely larger) and v_{rel} the relative velocity between the cluster and the cell wall. The reduced radius was derived from the reduced mass of the collision (mass of the cluster) as being the radius of a sphere with the same mass. Bouncing collisions are marked as circles and fragmenting collisions as asterisks. Red data points indicate that restructuring of the cluster was visible. Bouncing collisions with the cell walls were observed at collision energies between 10^{-11} and 10^{-8} J for radii between 0.1 and 1 mm, while fragmenting collisions and energies between 10^{-10} and 10^{-7} J for radii between 0.1 and 2 mm. The horizontal red dashed line represents the minimum energy at which visible restructuring of the clusters was observed: 7×10^{-11} J. From this value a macroscopic E_{roll} was calculated: $E_{\text{roll}} = 1.28 \times 10^{-11}$ J.

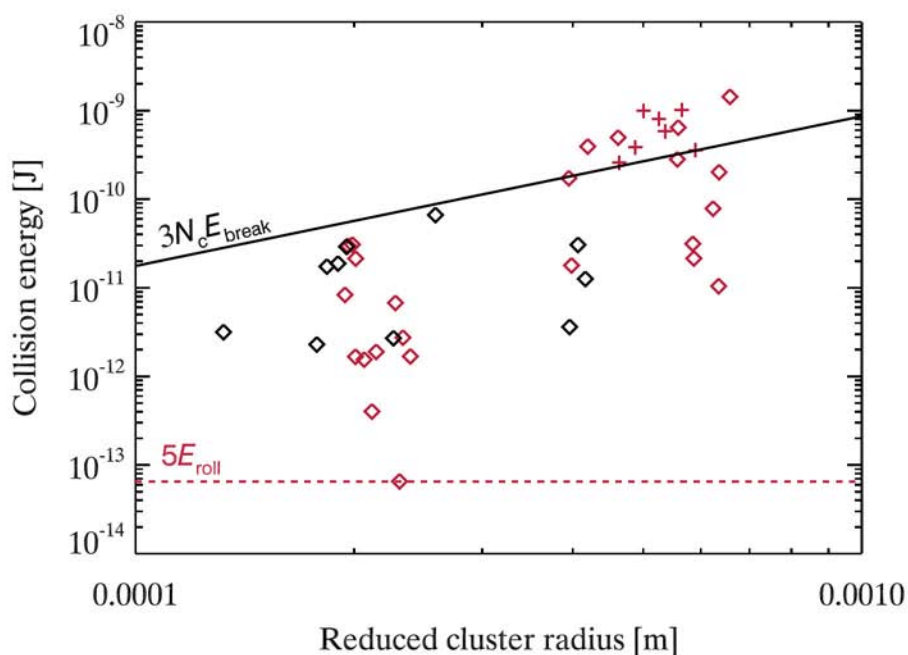


Figure 7.7: Aggregate collisions with the cell walls during the fast shaking phases of the third drop tower experiment run, for compacted aggregates composed of monodisperse SiO_2 . Diamonds represent bouncing collisions and plus signs fragmenting of the cluster. Red points show the collisions that displayed visible restructuring. The threshold energies $5E_{\text{roll}}$ for onset of visible restructuring (red dashed line) and $3N_c E_{\text{break}}$ for the loss of the first monomers (solid) are represented.

Table 7.3: Microscopic and macroscopic threshold energies for aggregate restructuring and fragmentation.

Threshold energy	Microscopic value [J]	Macroscopic value for non-compacted aggregates [J]	Macroscopic value for compacted aggregates [J]
E_{roll}	1.7×10^{-15} (Heim et al. 1999)	1.3×10^{-11}	1.3×10^{-14}
E_{break}	1.3×10^{-15} (Poppe et al. 1999)	3.0×10^{-13}	4.1×10^{-13}

In the same manner a value for the energy required to break a contact between two macroscopic aggregates was derived: the solid line in Figure 7.6 marks the onset energy of fragmentation, $3N_c E_{\text{break}}$. The measured value was $E_{\text{break}} = 3.0 \times 10^{-13}$ J.

The same analysis was performed for the compacted aggregates composed of monodisperse SiO_2 (Figure 7.7). Table 7.3 compares the rolling and breaking energies for the compacted and non-compacted aggregates. The aggregate compaction seems to have no influence on the energy required to break a contact between two aggregates ($E_{\text{break}} = 4.1 \times 10^{-13}$ J and 3.0×10^{-13} J for compacted and non-compacted aggregates, respectively). The rolling energy, however, is 3 orders of magnitude lower for the compacted (1.3×10^{-14} J) than for the non-compacted aggregates (1.3×10^{-11} J), indicating that irreversible rolling is much easier to trigger between aggregates with a compacted shell than between uniformly porous aggregates.

7.3 Application to protoplanetary disks

The collision results from the SPACE experiments can be compared with current nebula models and some remarks on the sub-mm-sized dust aggregate behavior in protoplanetary disks can be made.

7.3.1 The disk models

Three common nebula models are derived from Weidenschilling (1977b), Andrews & Williams (2007) and Desch (2007). These models are based on surface density and temperature profiles of the form

$$\Sigma(\hat{r}) = \Sigma_0 \left(\frac{\hat{r}}{1 \text{ AU}} \right)^{-\delta} \quad (7.9)$$

and

$$T(\hat{r}) = T_0 \left(\frac{\hat{r}}{1 \text{ AU}} \right)^{-\epsilon} \quad (7.10)$$

with \hat{r} being the distance to the central star, Σ_0 and T_0 , the values of the surface density and temperature at 1 AU, and δ and ϵ their respective exponents. $T_0 = 280 \text{ K}$ and $\epsilon = 0.5$ are assumed identical for all three models. Table 7.4 lists the surface density parameters. The Minimum Mass Solar Nebula developed by Weidenschilling (1977b) is based on the minimum mass required in an original protoplanetary disk to build the Solar System as it exists today ($\Sigma_0 = 1700 \text{ g/cm}^2$). Andrews & Williams (2007) derived a low-density nebula model from the astronomical observations of circumstellar dust disks in Taurus-Auriga ($\Sigma_0 = 20 \text{ g/cm}^2$) and Desch (2007) a high density model by considering planetesimal migration subsequent to their formation in a compact configuration around the newly formed star ($\Sigma_0 = 50500 \text{ g/cm}^2$).

Turbulence in the disk is commonly assumed to have a Richardson scale cascade and to follow a so-called α -prescription (Shakura & Sunyaev 1973), where

$$\alpha = \frac{\tilde{\nu}}{c_s H} \quad (7.11)$$

Table 7.4: Model parameters for surface density of three common protoplanetary nebula models.

Nebula model	Σ_0 [g/cm^2]	δ
Weidenschilling (1977b)	1700	1.5
Andrews & Williams (2007)	20	0.8
Desch (2007)	50500	2.168

with α being a dimensionless parameter characterizing the strength of the turbulence, c_s being the sound speed in the disk, and $\tilde{\nu}$ and H the disk viscosity and height, respectively. Typical values for α are 10^{-5} in quiet regions of the disk, like e.g. in a "dead-zone" that could develop around 1 AU (Turner et al. 2007, Brauer et al. 2008b), and up to 10^{-2} in more turbulent regions.

To compute the dust aggregate relative velocities for different aggregate sizes in the nebula midplane, an adaptation of a code developed by Brauer et al. (2008a) was used. The effects considered to induce relative velocities were Brownian motion (Einstein 1905), radial drift (Whipple 1972, Weidenschilling 1977a) and turbulence (Ormel & Cuzzi 2007) (see Section 1.2).

7.3.2 Aggregate sticking and growth

The computed relative velocity profiles for a low turbulence region ($\alpha=10^{-5}$) at 1 AU can be seen in Figures 7.8 to 7.10 for all three models. The collisions observed during the different SPACE experiments are plotted as well (see the explanation of the symbols in Table 6.1). The striped boxes represent the collisions observed during the SPACE experiment on the REXUS suborbital flight. Similar to Figure 7.2, these boxes span the initial size distributions of aggregates inserted into the experiment cells (same values as in Figure 6.1) and their length reaches from monomer aggregate to cluster sizes (see Section 7.1.1 for more details). From this figure, the relative velocities between the colliding aggregates that would be induced by a PPD environment can be derived.

In order to compare these relative velocities to the ones induced by the SPACE set-up, the minimum velocity for perfect aggregate sticking determined for both rocket flight aggregate size distributions, 11.1 cm s^{-1} (see Table 6.2, dotted contour in Figures 7.8 to 7.10) and the maximum velocity at which sticking was observed during drop tower experiments, 5.2 cm s^{-1} (see Section 6.1.1, dashed contour in Figures 7.8 to 7.10) were added.

For the minimum mass (Figure 7.8) and the compact (Figure 7.10) nebula models, the expected relative velocities for aggregate-aggregate and aggregate-cluster collisions of these sizes are lower than both the velocity for perfect aggregate sticking measured during the suborbital flight and the highest observed velocity for sticking measured during the drop tower experiments. This indicates that at 1 AU and in a low turbulence environment like an MRI dead-zone, the investigated collisions would lead to cluster growth. In fact, collisions would lead to cluster growth up to sizes of a few mm for the Minimum Mass Solar Nebula and for the compact model. In the low density model (Figure 7.9), however, monomer aggregates would coagulate amongst each other up to a size of $\sim 500 \mu\text{m}$, but not to bigger agglomerates as the expected collision velocities then become higher than the velocity for perfect aggregate sticking determined in the suborbital flight experiment. Above this maximum size, bouncing would be expected.

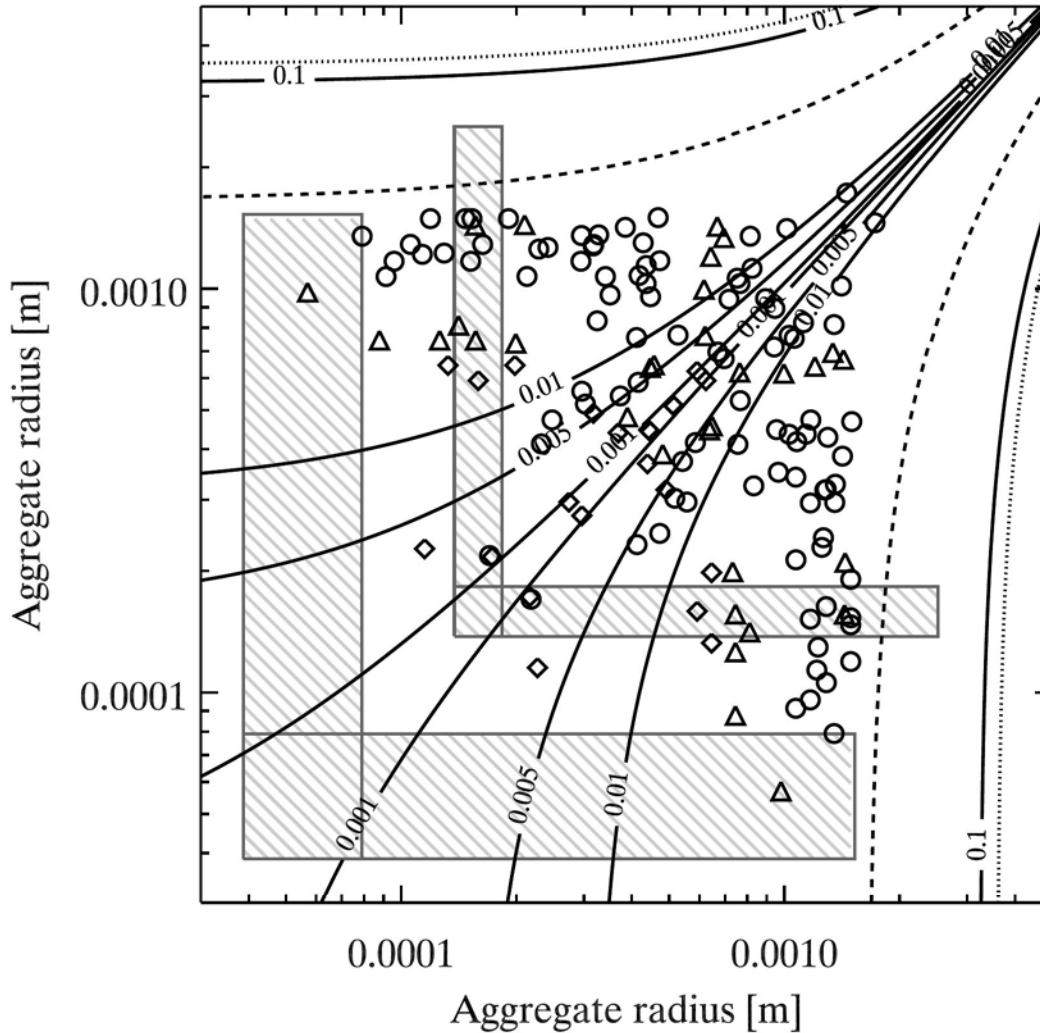


Figure 7.8: Relative velocity between dust aggregates in a protoplanetary nebula computed according to Weidenschilling (1977b) at 1 AU with a turbulence parameter of $\alpha=10^{-5}$. The velocity profiles are labelled in m s^{-1} . The sticking collisions observed in the drop tower experiment are plotted as single points (see Table 6.1 for a legend of the symbols). The striped boxes represent the collisions observed during the SPACE experiment on the REXUS suborbital flight. The respective height of the horizontal boxes represent the initial size distributions of aggregates inserted into the experiment cells and the width of the horizontal boxes spans from the monomer aggregate to cluster sizes (see Section 7.1.1 for more details). The dotted contours display the minimum sticking velocity determined for both rocket flight aggregate size distributions (11.1 m s^{-1}), and the dashed contour, the maximum velocity at which sticking was observed during drop tower experiments (5.2 m s^{-1}).

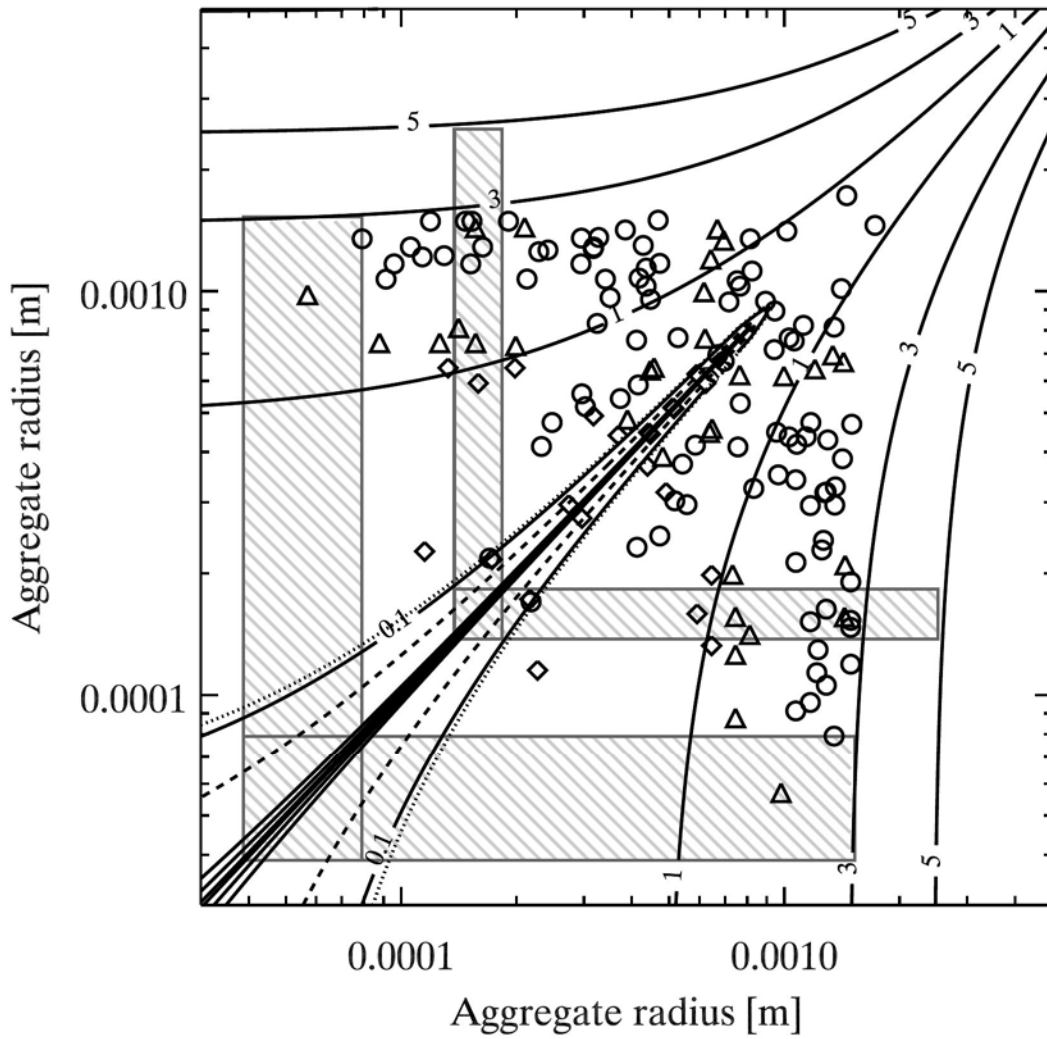


Figure 7.9: Same as in 7.8 but for the protoplanetary disk model of Andrews & Williams (2007).

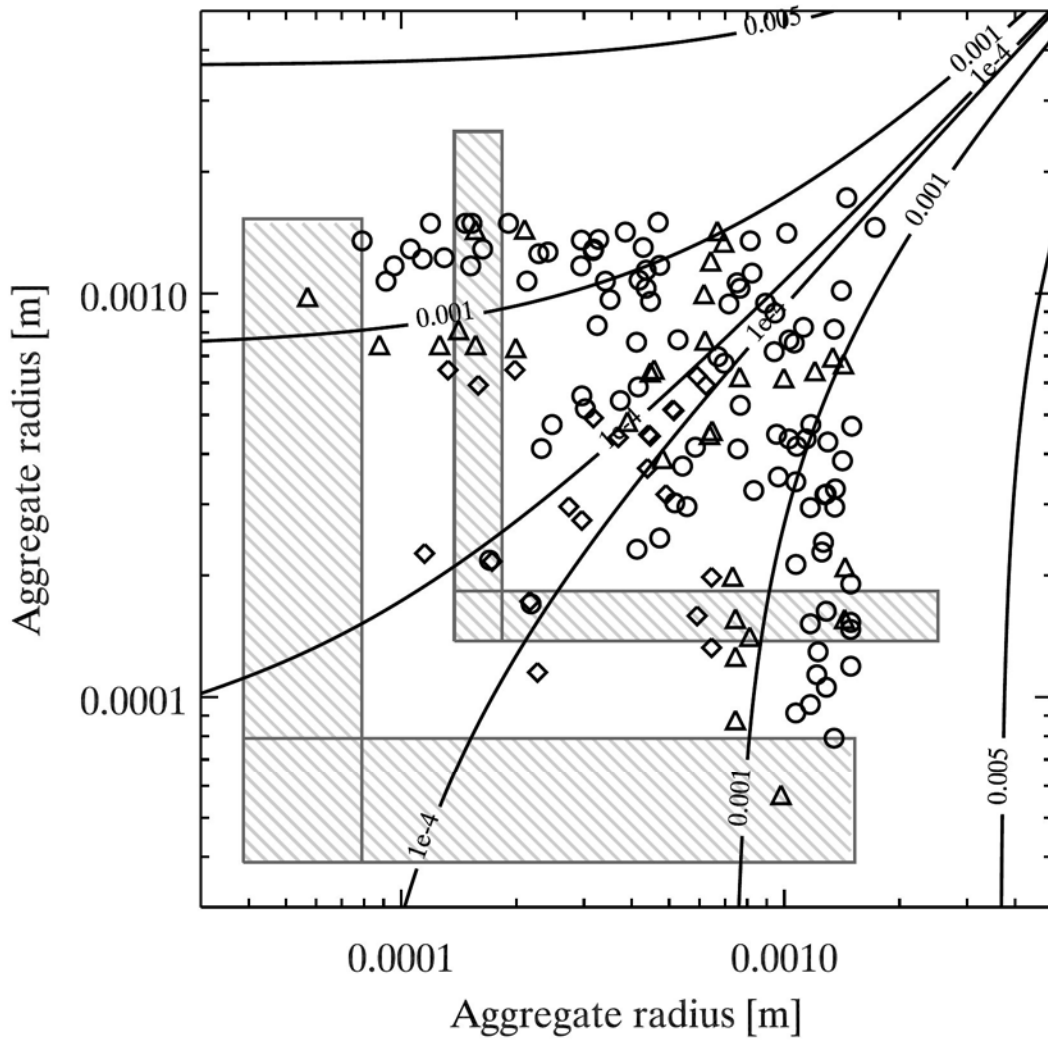


Figure 7.10: Same as in 7.8 but for the protoplanetary disk model of Desch (2007). In this model, the dotted and dashed contours (see Figure 7.8) are outside of the depicted parameter field.

7.3.3 Cluster restructuring and fragmentation

As the relative velocities between clusters composed of $\sim 100 \mu\text{m}$ aggregates can be predicted in the protoplanetary disk, their collision energy can be determined as well. If the collision energy E_{coll} is approximated to be only composed of the translational kinetic energy of the colliding aggregate system, then

$$E_{\text{coll}} = \frac{1}{2} \frac{m_1 m_2}{m_1 + m_2} v_{\text{rel}}^2 \quad (7.12)$$

with m_1 and m_2 being the masses of the colliding clusters and v_{rel} the relative collision velocity. This collision energy can be compared to the threshold energies for the onset of restructuring ($5E_{\text{roll}}$) and fragmentation ($3N_c E_{\text{break}}$) determined in Section 7.2.4.

The minimum energy required for the onset of restructuring was measured to be $E_{\text{restr}} = 5E_{\text{roll}} = 7 \times 10^{-11}$ J. Figure 7.11 shows the expected collision energy for dust aggregates in a Minimum Mass Solar Nebula (Weidenschilling 1977b). The dotted contour marks the threshold energy for the onset of cluster restructuring measured for non-compacted aggregates composed of monodisperse SiO_2 during the drop tower experiments (see Section 7.2.4 for details). It can be seen that for the chosen disk conditions (at 1 AU with $\alpha = 10^{-5}$), clusters composed of $\sim 100 \mu\text{m}$ aggregates would start restructuring at sizes of about 1 mm in radius, marking the onset of compaction. In addition, for each cluster size, the approximate total number of contacts between the constituting aggregates can be estimated as

$$N_c = 6 \left(\frac{r}{r_0} \right)^3 \quad (7.13)$$

with r being the radius of the cluster, r_0 the radius of a monomer aggregate ($\sim 50 \mu\text{m}$) and a mean coordination number of 6, chosen as in Section 7.2.4. With the energy required to break one contact between the constituting aggregates of the cluster, which was derived in Section 7.2.4, and the sum of the inter-aggregate contacts inside of both clusters, the threshold fragmentation energy $E_{\text{frag}} = 3N_c E_{\text{break}}$ can be computed for each pair of cluster sizes, and compared to the collision energy predicted by the protoplanetary disk model. The result of this investigation is presented in Figure 7.12. The values of the difference between the predicted collision energy of two clusters and the fragmentation threshold energy of this collision are given by contours. Positive values indicate that the collision energy is high enough to lead to the loss of the first monomers and aggregate disruption. In the Minimum Mass Solar Nebula model by Weidenschilling (1977b) (at 1 AU with $\alpha = 10^{-5}$), this happens for clusters of sizes ~ 1 cm.

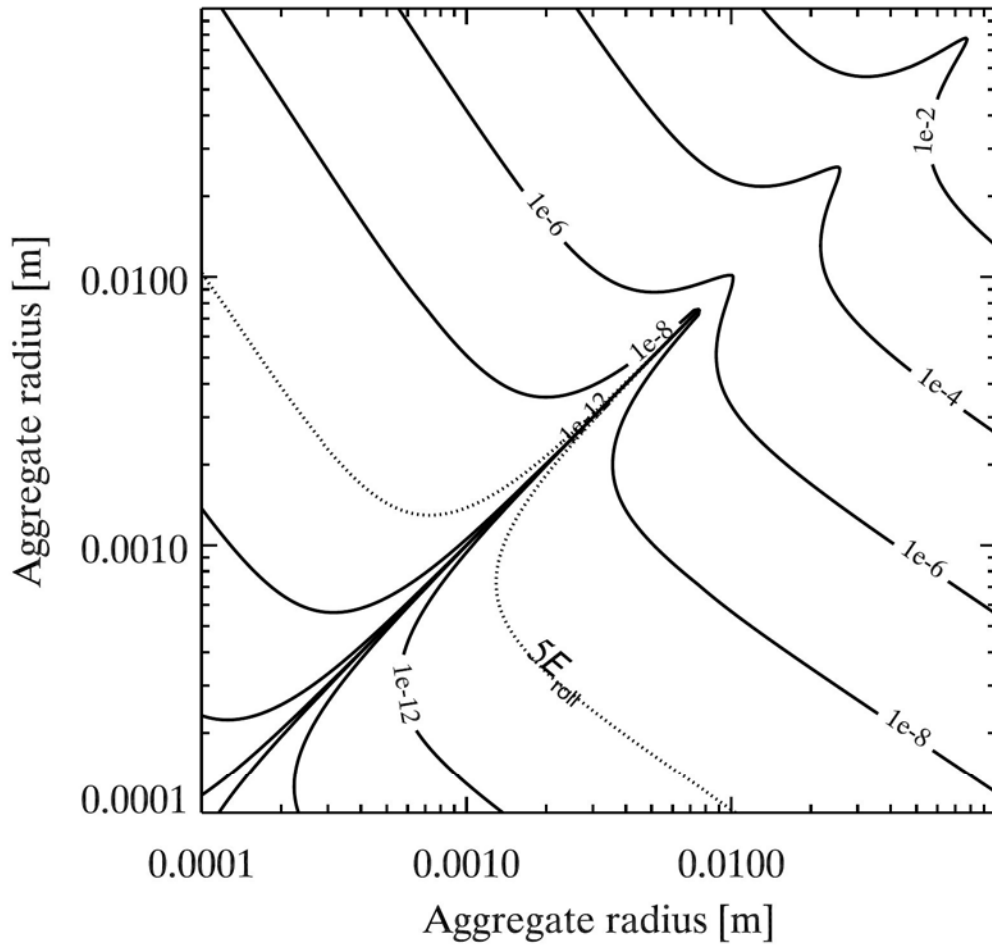


Figure 7.11: Collision energy profiles (J) for clusters composed of $\sim 100 \mu\text{m}$ aggregates in a Minimum Mass Solar Nebula at 1 AU with $\alpha = 10^{-5}$. The dotted contour represents the minimal energy for onset of cluster restructuring $5E_{\text{roll}} = 6.5 \times 10^{-11}$ measured in Section 7.2.4.

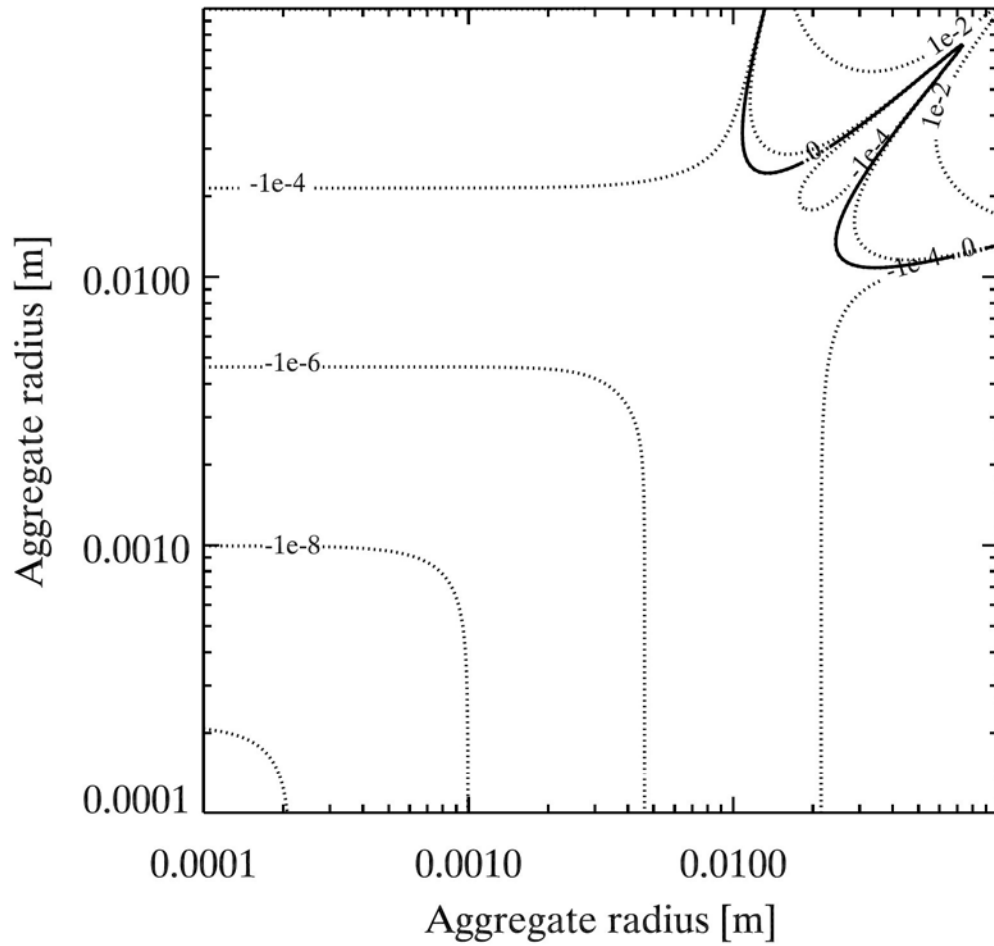


Figure 7.12: Contours of the difference between the predicted collision energy between two clusters and the fragmentation threshold energy $3N_c E_{\text{break}}$ in a Minimum Mass Solar Nebula at 1 AU with $\alpha = 10^{-5}$. The values are given in J. At the 0 contour line and for positive values, the clusters start fragmenting.

8 Conclusion

This work presented the set-up, experiment runs and scientific data results of the Suborbital Particle Aggregation and Collision Experiment (SPACE), a multi-particle collision experiment conducted under microgravity conditions. The particles investigated were sub-mm-sized aggregates of protoplanetary dust analog material (mono- and polydisperse SiO_2 , see Section 4). The SPACE experiment set-up was flown at the drop tower in Bremen in five drops with 9 s of microgravity time each, and on the REXUS 12 suborbital rocket with 170 s of microgravity time (see Section 3).

In the different experiments performed, sub-mm-sized aggregates grew to clusters of sizes up to a few millimeters (see Section 6). The aggregate collisions leading to this growth were analyzed either directly or statistically, gathering data input to the collision model of Güttler et al. (2010) and Kothe et al. (2013). In particular, the SPACE experiments delivered data in the size and velocity ranges of the transitions between sticking and bouncing and between bouncing and fragmentation (see Section 6). While the observed collisions were individually analyzed in the case of the drop tower experiments, the statistical approach on the suborbital flight data allowed for a first time continuous measurement of the sticking probability between aggregates along a velocity range covering the sticking to bouncing transition (see Figure 6.8).

The collision outcomes observed were in agreement with the model and displayed transitions from sticking to bouncing and from bouncing to fragmentation with increasing aggregate mass and collision velocity (see Table 7.1). However, compared to the collision outcomes expected (Weidling et al. 2012, Kothe et al. 2013), sticking in the SPACE experiments occurred "later" (for bigger and faster aggregates) and fragmentation "earlier" (for smaller and slower aggregates). This behavior could be traced back to the type of collisions observed, occurring between aggregates and bigger clusters and not between same-sized aggregates. The model by Güttler et al. (2010) looked into the influence of the mass ratio of colliding aggregates (their Figure 11, upper right panel). However, the experimental results used to compile this panel of the model mostly involved collisions at velocities around or higher than 1 m s^{-1} (Blum & Wurm 2000, Wurm et al. 2005, Paraskov et al. 2007, Langkowski et al. 2008, Schräpler & Blum 2011). It would be interesting to update the model for collisions between differently-sized aggregates at the low velocities observed here and include the data gathered by the SPACE experiments.

The fractality of the growing clusters also seems to play a role in the enhanced sticking as well as fragmentation probabilities, as the complex shapes of the clusters ease the capture of aggregates, but also the loss of loosely bound constituents. It would be interesting to

confirm and quantify these observations with additional long-term (several minutes) microgravity experiments, where aggregates would have time to grow into fractal structures. In addition to the data input to the collision model, structural properties of clusters composed of sub-mm-sized dust aggregates could be determined. The cluster fractal dimensions, inner cohesion (effective surface energy of the constituting aggregates, tensile strength of the outer layer) and restructuring and fragmentation energies were measured (see Section 7.2). This investigation showed that clusters composed of sub-mm-sized aggregates display a behavior comparable to simulated clusters composed of μm -sized particles. Therefore, the results of molecular dynamics simulations of cluster collisions could be applied to macroscopic aggregates, when using adapted parameter values. Usually, direct dust aggregate growth simulations working with μm -sized or smaller monomer particles are limited to final aggregate sizes of $\sim 100 \mu\text{m}$ (see e.g. Wada et al. 2008). The aggregate and cluster properties measured in the SPACE experiments could be used to simulate aggregates and clusters of up to 10 cm in size, by using monomer constituents of $\sim 100 \mu\text{m}$. It would also be interesting to perform further long-term microgravity experiments with smaller or bigger aggregates. The systematic formation of clusters and maybe a scaling of their properties depending on the aggregate size could be derived and used in numerical simulations.

Finally, the application to current protoplanetary disk environments of the cluster properties determined in this work lead to a few conclusions on cluster behavior (see Section 7.3). In the minimum mass Solar Nebula (Weidenschilling 1977b), for example, clusters composed of sub-mm-sized dust aggregates would still be sticking upon collision at sizes of 1 mm. Restructuring would start for clusters of about 1 cm and fragmentation at about 5 cm. The values of critical rolling and breaking energy determined for the investigated aggregates (see Section 7.2.4) could be used in numerical simulations to investigate the long-term behavior of aggregate clusters in a protoplanetary disk, e.g. in dust concentration regions as streaming instabilities, turbulent eddies or pressure bumps. Indeed, such dust accumulations might lead to the formation of planetesimals by gravitational and aerodynamic group effects (or cometesimals, Johansen et al. 2014) and thus overcome the growth barriers mentioned in Section 1.3. Research in this field is on-going in an attempt to close the gap between cm- to meter-sized bodies. The properties of macroscopic aggregates inside of clusters are an essential input to such modelling (as seen in Skorov & Blum 2012, for example) and the measurements performed in the SPACE experiments could be valuable input.

To conclude this work, a final remark on the use of suborbital rockets for the investigation of protoplanetary dust should be made. The evident advantage of microgravity phases lasting several minutes is mitigated by the lower quality of this microgravity compared to other microgravity platforms (e.g. drop tower, see Table 1.1). Although it was shown that residual accelerations during the flight could be neglected compared to the intentionally induced ones (cell shaking), their effect clearly influenced the obtained collision data by growing clusters on the experiment cell walls instead of free-flying inside the cell volume. However, with the right analysis methods, valuable and unique measurements of dust aggregate properties could be performed, benefitting from the continuous long-duration microgravity phase of the flight. Further suborbital flight experiments would definitely consolidate and extend the experience gained by the present work to the profit of future scientific outcomes.

A SPACE components list

Item	Supplier	Costs	Size	Weight	Details
Camera	Allied Vision Technologies	€ 1800	39 x 51 x 80	169 g	Prosilica GE680
Objective	Schneider Kreuznach	Loan from IGEP	∅30 x 37	100 g	
Camera Control		€ 367	72 x 100 x 25	191 g	
Single-board computer (SBC)	Toradex	€ 261	55 x 84 x 5	40 g	Robin Module Z530 L V2.0
SBC Baseboard	Toradex	€ 90	72 x 100 x 10	71 g	Daisy V1.1 COM Express baseboard
SBC Heatsink Plate	Toradex	€ 16	55 x 84 x 12	80 g	Robin Z5xx Heatsink
Data Storage		€ 59	50 x 97 x 5	26 g	
Compact Flash Card	Amazon	€ 44	43 x 36 x 3.3	10 g	Transcent Compact Flashcard, 16GB, 600x
Compact Flash to S-ATA Adapter	Amazon	€ 15	51 x 73 x 6	16 g	Adapter from Adaptare
Mirror	Edmund Optics	€ 50	75 x 75 x 5		
Electronics box		€ 11	100 x 150 x 30	150 g	This weight includes the electronics box mounting structure
Micro-controller	Reichelt	€ 6	15 x 52 x 5	7 g	ATMega32 (Atmel)
Continued on next page					

A SPACE components list

Item	Supplier	Costs	Size	Weight	Details
Servo-controller	Reichelt	€ 4	7 x 25 x 5	2 g	L6202 (SGS-Thomson)
Level converter	Reichelt	€ 3	7 x 11 x 5	1 g	MAX488 (Maxim)
Solid-State Relay	Laboratory Supply	/	30 x 42 x 5	10 g	DMP6301A (Crydom) Two required
Capacitors	Laboratory Supply	/	1 x 1 x 1 to 10 x 10 x 15	1 g to 5 g	Ceramic: 13 (2x10n, 2x22n, 8x100n, 1x220n) Elko: 6 (4x1 μ , 2x220 μ)
Resistors	Laboratory Supply	/	1 x 6 x 1	0.5 g	22 (4x0,1, 1x10, 8x1k, 3x3k, 6x10k)
Quartz	Laboratory Supply	/	1 x 10 x 2	1 g	16 MHz Quartz
Voltage Converter	Laboratory Supply	/	9 x 15 x 4	5 g	5 V: 1 12 V: 1
Operational Amplifier	Laboratory Supply	/	6 x 19 x 3	1 g	LM324M and OP13
Connectors	Reichelt	< € 1	8 x 15 x 10 to 12 x 38 x 15	2 g to 5 g	6-pin: 1 D-SUB 15 M: 1
Vacuum chamber		€ 1126	∅130 x 180	6863 g	This weight includes the main chamber cylinder, the top and bottom flanges, the viewport, the double claw clamps and the electrical feed-through.
Vacuum Chamber Core	Hositrad	€ 850	∅130 x 150	4605 g	
Top/Bottom flange	Hositrad	€ 28 each	∅130 x 20	716 g each	2 aluminum ISO-K blank flanges

Continued on next page

Item	Supplier	Costs	Size	Weight	Details
Double-wall clamp	Hositrad	€ 2 each	∅16 x 62.5	46 g each	4 aluminum clamps per ISO-K flange are required (8 in total)
Centering ring	Hositrad	€ 15 each	∅125 (ring) x 5	125 g each	2 sealing rings for the ISO-K flanges.
Viewport	Hositrad	€ 108.8	∅113.5 x 17.5	152 g each	CF63 viewport with zero-length glass
Electrical feed-through	Hositrad	€ 173.4	∅34 x 7.6	56 g each	CF16 8-pin feed-through with copper pins.
Pressure sensor	Thyracont	€ 277	∅32 x 74	131 g	VSMP62MVCF
Vacuum Valve	Balzers	Loan from IGEP	38 x 52 x 102	464 g	EVC 110M
LED array	Built at IGEP	€ 80	11.7 x 50 x 50	200 g	
Motor	Faulhaber	€ 60	∅22 x 30	50 g	2230 U (Faulhaber)
Shaking mechanism		€ 25	55 x 54 x 100	96 g	
Conical cog wheel	rs-online	€ 7 for both	∅10 x 3 and ∅20 x 3	10 g for both	1 Z20, M0.5, 45 deg, Delrin 1 Z40, M0.5, 45 deg, Delrin
Cog wheel	rs-online	€ 3 to € 5	∅6 x 9 and ∅26 x 4	2 g to 16.7 g	2 10Z, M0.5, steel and 4 50Z, M0.5, steel
Axis	Built at IGEP	/	∅3 x 54 and ∅4 x 36	5 g	1 rotor axis between motor and shaker frame and 2 rotation axes for the shaker frame.
Shaker Frame	Built at IGEP	/	30 x 40 x 20	8 g	
Particle containers	Built at IGEP	€ 50	two 10 x 15 x 10 and one 24 x 15 x 10	10 g	3 particle containers
Structural Components		/	/	386 g	
Mirror frame	Built at IGEP	/	75 x 140 x 75	22 g	
Camera frame	Built at IGEP	/	64 x 120 x 34	37 g	

Continued on next page

A SPACE components list

Item	Supplier	Costs	Size	Weight	Details
SBC plate	Built at IGEP	/	72 x 125 x 7	56 g	
Motor plate	Built at IGEP	/	30 x 30 x 27	7 g	
Shaking mechanism structure	Built at IGEP	/	39 x 32 x 45	6 g	
Bolts	Laboratory Supply	/	/	250 g	16 M2, 52 M3 and 16 M8

B SPACE electronics board

Figure B.1: SPACE electronics board print. Red lines are on the top of the board, blue lines on the bottom.

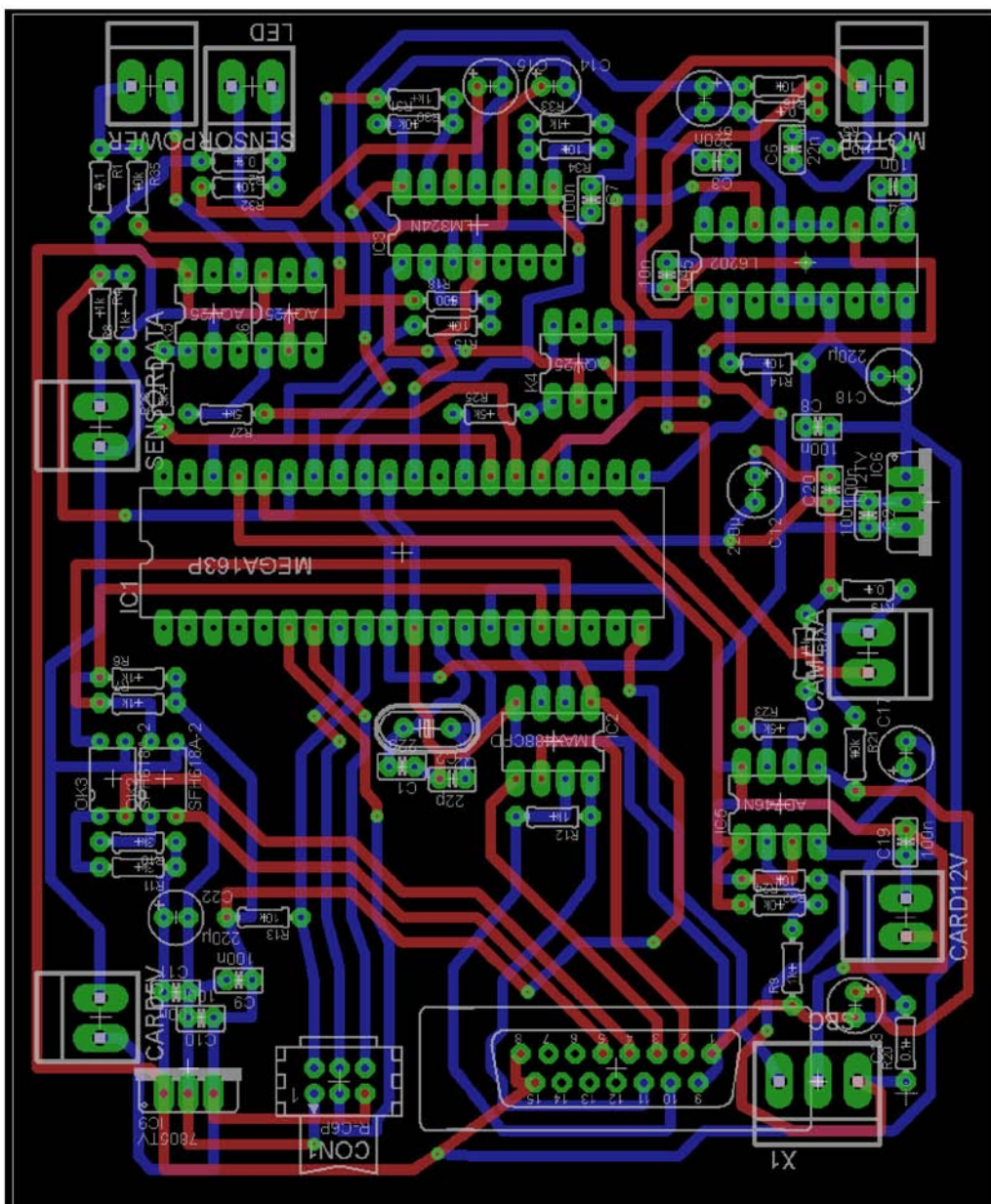
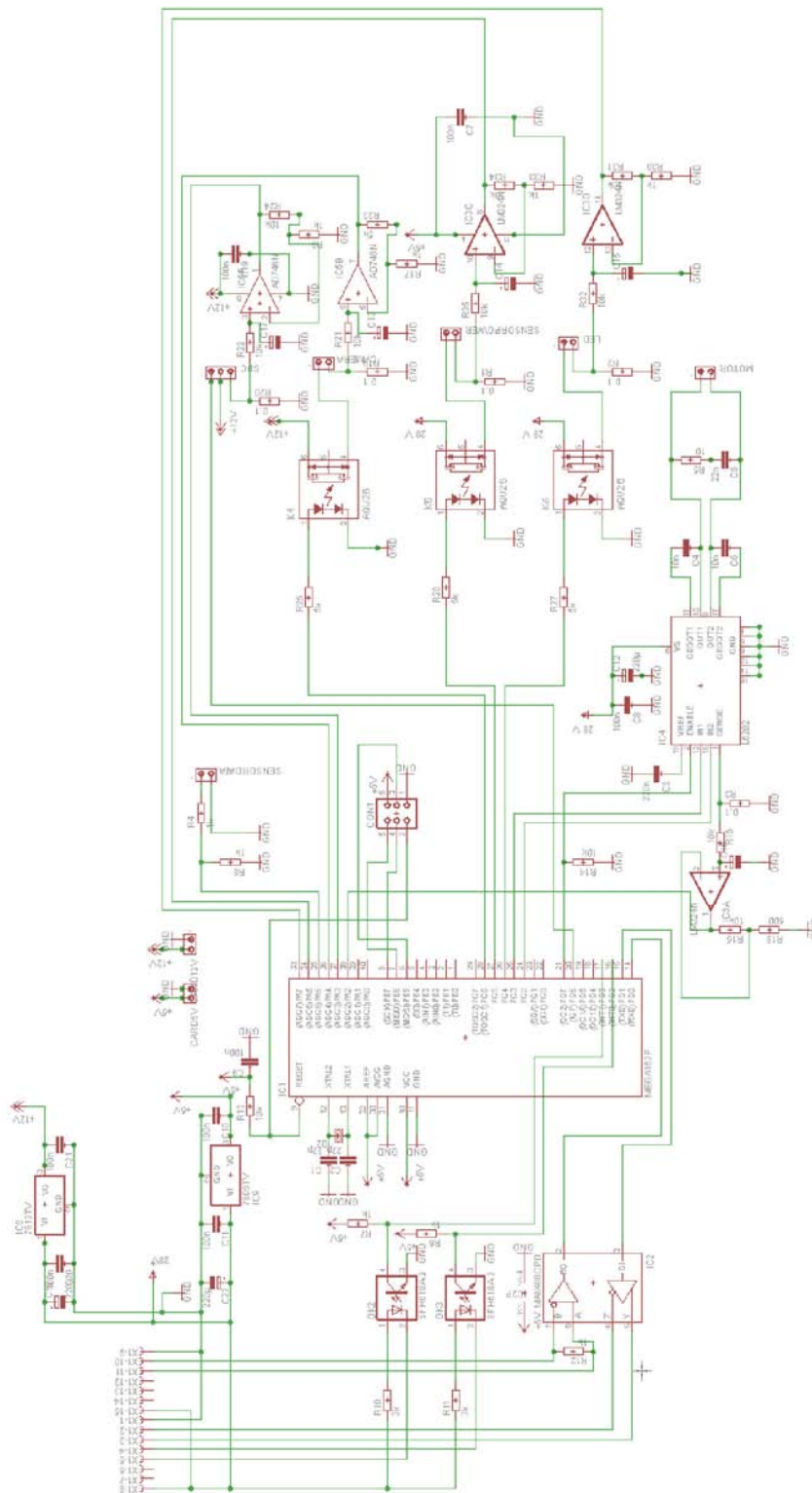


Figure B.2: SPACE electronics board circuit.



C SPACE hardware test protocols

C.1 Vacuum tests

Title: Tightness and camera vacuum test

Date: 20.09.2011

Participants: René Weidling, Daniel Heißelmann

Components tested: Camera.

Pre-test configuration: Camera in vacuum chamber at ambient pressure.

Procedure:

Time	Action	Comments
10:30	Cleaned all vacuum connections	Hair on glass O-ring Scratch on aluminum top flange
11:10	Evacuation of the vacuum chamber	
13:15	End of chamber evacuation (0.7 mbar) Start the leak finder	
14:00	Flooded chamber with Helium Checked leakage from outside	Top flange and pressure gauge seem to be leaking
Continued on next page		

C SPACE hardware test protocols

Time	Action	Comments
14:35	Replaced the aluminum top flange with a stainless steel one	Pressure = 1.3×10^{-2} mbar Leak rate= 6×10^{-6} mbarL s ⁻¹
15:45	Camera switched on for 5 min 11.9 V, 0.19 A	Nominal behavior
16:00	Replaced the stainless steel top flange with the aluminum top flange	Leak rate= 0.4×10^{-6} mbarL s ⁻¹

Conclusion:

Camera: nominal behavior during the test

Vacuum chamber: the aluminum top flange should be polished again.

Title: Vacuum hose tightness test**Date:** 06.12.2011**Participants:** René Weidling, Daniel Heißelmann**Components tested:** Vacuum hose, vacuum umbilical.

Pre-test configuration: Hose connected to umbilical.
 Umbilical connected to TMP and pre-vacuum pump.
 Pressure sensor connected to hose.

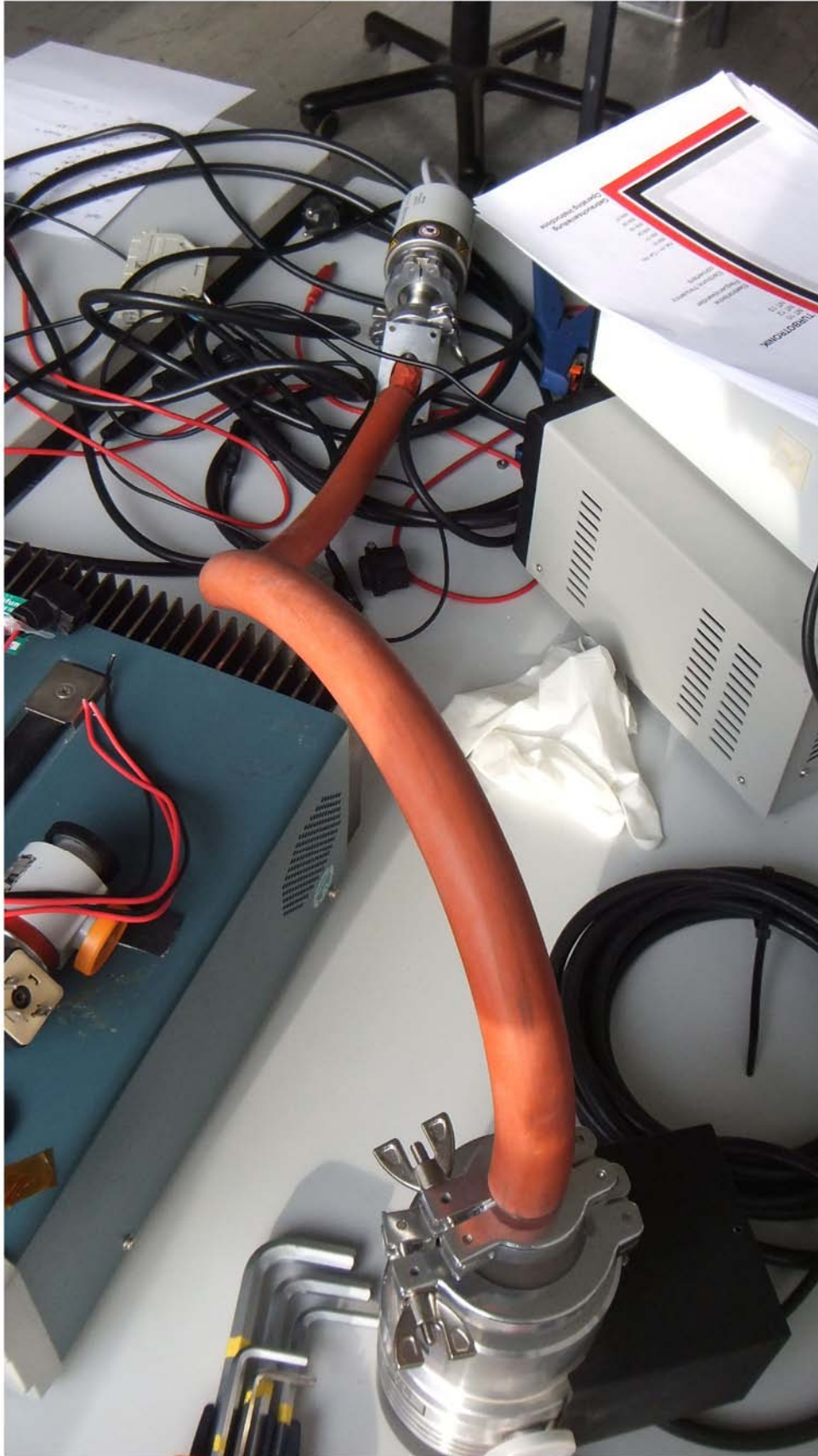
Procedure:

Time	Action	Comments
14:00	Start of hose evacuation	
07.12.2011 14:21	Switch off TMP	2.86×10^{-3} mbar
15:09	Switch off pre-vacuum pump	4.6×10^{-2} mbar
15:10		5.6×10^{-2} mbar
15:11		5.85×10^{-2} mbar
15:12		6.25×10^{-2} mbar
15:13		6.59×10^{-2} mbar
15:34	Switch on pre-vacuum pump	1.5×10^{-1} mbar
15:43	Switch on TMP	4.11×10^{-2} mbar
15:59		4.14×10^{-3} mbar
08.12.2011 09:40	End of test	2.57×10^{-3} mbar

Conclusion:

The vacuum hose can be used to evacuate the experiment on the launcher. The values recorded during this test can give an indication on how long the pumps can be switched on and off during the pre-launch phase.

Figure C.1: Vacuum hose tightness test setup.



C.2 Thermal tests

Title: Temperature test

Date: 15.11.2011

Participants: Julie Brisset, Stefan Kothe

Components tested: Camera with objective, motor, shaking mechanism, particle container, LED array, pressure sensor, mirror in frame.

Pre-test configuration: All components at room temperature (19 °C) placed in temperature chamber.
All components off.
Optical calibration target placed in front of the camera.

Procedure:

Time	Action	Comments
12:17	Switch on camera	Camera switches on Centre line sharp
12:21	Switch off camera	Camera off
12:22	Switch on motor at 12 V	Motor switches on Shaking mechanism ok
12:24	Switch off motor	Motor off
12:25	Switch on LED array and pressure sensor	LED array on, all LEDs ok Pressure sensor on, nominal reading of ambient pressure (8 to 9 V)
12:26	Switch off LED array and pressure sensor	LED array and pressure sensor off
12:27	Ramp temperature down to -40 °C at -0.9 °C/min	
12:54	Reached -40 °C	
13:00	Door opened for 2 s at -41 °C	Ramp resumes at -38 °C
Continued on next page		

C SPACE hardware test protocols

Time	Action	Comments
14:07	Temperature: -40.2 °C Switch on camera Switch on LED array Switch on motor at 12 V Switch on pressure sensor	Camera on, center line sharp LED array on, 7 LEDs failed Motor on, shaking mechanism working fine Pressure sensor on, reading nominal
14:15	Switch off LED array Switch off motor Switch off pressure sensor	LED array off Motor off Pressure sensor off
14:16	Door opened for 2 s at -40 °C	Ramp resumes at -35 °C
14:25	Door opened for 2 s at -40.2 °C	Ramp resumes at -30 °C
14:26	Ramp temperature up to -5 °C at 0.9 °C/min	
14:35	Reached -5 °C	
14:37	Switch off camera	Camera off
15:23	Temperature: -5 °C Switch camera on	Camera on Center line sharp
15:24	Switch on LED array Switch on motor at 12 V Switch on pressure sensor	LED array on, 7 LEDs failed (the same as before) Motor on, shaking mechanism working fine Pressure sensor on, reading nominal
15:26	Switch off camera Switch off LED array Switch off motor Switch off pressure sensor	Camera off LED array off Motor off Pressure sensor off
15:30	Ramp temperature up to 70 °C at 0.9 °C/min	
15:48	Reached 70 °C	
16:30	Temperature: 70 °C Switch on camera Switch on LED array Switch on motor at 12 V	Camera on, center line sharp LED array on, 7 LEDs failed (the same as before) Motor on, shaking mechanism working fine Pressure sensor on, reading nominal

Continued on next page

Time	Action	Comments
	Switch on pressure sensor	
16:34	Switch off LED array Switch off motor Switch off pressure sensor	LED array off Motor off Pressure sensor off
16:37	Switch camera off	Camera off
16:38	Ramp temperature down to 25 °C at -0.9 °C/min	
16:54	Reached 25 °C	
17:40	Temperature: 25 °C Switch on camera Switch on LED array Switch on motor at 12 V Switch on pressure sensor	Camera on, center line sharp LED array on, 2 LEDs fully recovered, 5 switch on/off Motor on, shaking mechanism working fine Pressure sensor on, reading nominal
17:43	Switch off camera Switch off LED array Switch off motor Switch off pressure sensor	Camera off LED array off Motor off Pressure sensor off
17:45	End of test	Mirror intact

Conclusion:

Camera: nominal behavior during the test

Objective: no focus changes due to temperature

LED array: the 7 LEDs that failed are on the same circuit line, which therefore has to be checked, fixed and re-tested
Pressure sensor: nominal behavior during the test

Motor: nominal behavior during the test

Shaking mechanism: nominal behavior during the test

Mirror: intact

Title: Temperature test 2

Date: 22.11.2011

Participants: Julie Brisset, Stefan Kothe

Components tested: Single-board computer with baseboard and heatsink, camera, electronics board, motor with shaking mechanism and LED array.

Note: The motor and shaking mechanism behaved nominally during the first temperature test, but as they are now mounted on the chamber plate together with the LED array, which has to be retested, they also participate into this re-test.

The camera behaved nominally during the first temperature test, but as it is now connected to the camera control computer which has to be tested, it also participates into this test.

In the previous test, the components were switched on and off directly at the power supplies. This time, the electronics board is the controlling the power distribution. Switching components is performed via sending signals to the microcontroller.

Pre-test configuration: All components at room temperature (20.5 °C) placed in temperature chamber.
All components off.

Procedure:

Time	Action	Comments
11:20	Temperature: 20.5 °C Switch on camera Switch on LED array Switch on motor at 12 V Switch on computer	Camera on LED array on Motor on, shaking mechanism working fine Computer on
11:25	Switch off camera Switch off LED array Switch off motor	Camera off LED array off Motor off
11:30	Ramp temperature down to -40 °C at -0.9 °C/min	
Continued on next page		

Time	Action	Comments
13:00	The hardware in the temperature chamber completely frosted, as one of the chamber windows was not closed during ramping down of temperature.	It is decided to not test the hardware while covered in frost. The computer however is still on and behaves nominally
13:05	Switch computer off	Computer off
13:10	Ramp temperature up to 50 ° C at 0.9 °C/min	This aims at evaporating the frost as fast as possible without having water damaging the hardware
13:50	Reached 50 °C	
14:05	Temperature regulation is switched off	Check if the hardware survived the frost
14:09	Temperature: 40 °C Switch on camera Switch on LED array Switch on motor at 12 V Switch on computer	Camera on LED array on Motor on, shaking mechanism working fine Computer on, nominal behavior ...everything survived
14:13	Switch off camera Switch off LED array Switch off motor	Camera off LED array off Motor off
14:14	Ramp temperature up to 70 ° C at 0.9 °C/min	Computer still on
14:42	Temperature: 70 °C Switch on camera Switch on LED array Switch on motor at 12 V	Computer switched off, over temperature Camera on LED array not switching on, looks like a PCB issue Motor on, shaking mechanism working fine
14:46	Switch off camera Switch off LED array Switch off motor Switch off computer	Camera off LED array off Motor off Computer off
14:48	Ramp temperature down to 50 ° C at -0.9 °C/min	
15:10	Temperature: 50 °C Switch on camera	Camera on
Continued on next page		

Time	Action	Comments
	Switch on LED array Switch on motor at 12 V Switch on computer	LED array on Motor on, shaking mechanism working fine Computer on, nominal behavior
15:16	Switch off camera Switch off LED array Switch off motor Switch off computer	Camera off LED array off Motor off Computer off
15:17	Ramp temperature down to -40 °C at -0.9 °C/min	
16:14	Temperature: -40 °C Several components power cycles: 1. Cycle 2. Cycle 3. Cycle 4. Cycle 5. Cycle	Camera on LED array on Motor on, shaking mechanism working fine Computer on, nominal behavior The power draw is lower than at room temperature Minor μ C bugs wrt signals Same behavior Nothing switches on, the μ C doesn't seem to receive signals Everything nominal, no μ C bugs anymore Everything nominal
16:38	Ramp temperature up to -5 °C at 0.9 °C/min	
17:23	Temperature: -5 °C Switch on camera Switch on LED array Switch on motor at 12 V Switch on computer	Camera on LED array on Motor on, shaking mechanism working fine Computer on, nominal behavior
17:25	Switch off camera Switch off LED array Switch off motor	Camera off LED array off Motor off
Continued on next page		

Time	Action	Comments
	Switch off computer	Computer off
17:30	Ramp temperature up to 20 ° C at 0.9 °C/min	
17:56	Temperature: 20 °C Switch on camera Switch on LED array Switch on motor at 12 V Switch on computer	Camera on LED array on Motor on, shaking mechanism working fine Computer on, nominal behavior
18:00	Switch off camera Switch off LED array Switch off motor Switch off computer	Camera off LED array off Motor off Computer off
18:05	End of test	

Conclusion:

Camera: nominal behavior during the test

LED array: nominal behavior during the test, the defect circuit line was successfully fixed

Motor: nominal behavior during the test

Shaking mechanism: nominal behavior during the test

Computer: nominal behavior except for an over-temperature switch-off at 70 °C. The computer was placed right in front of the hot air inlet in the temperature chamber and the 70 °C were kept for about 30 min. As this situation is not expected to happen during the REXUS campaign, the computer is considered fit for flight.

Electronics board: the μC had a couple of bugs at lower temperatures which completely disappeared after a few experiment cycles (inner components probably heat up again to a nominal functioning temperature). During the REXUS campaign, the μC will be switched on at latest 10 min before launch leaving plenty of time to the inner components to heat themselves up to a nominal functioning temperature. All other functionalities of the board worked fine throughout the test. Therefore the board is considered fit for flight.

Figure C.2: Second thermal test setup: hardware in the temperature chamber. The electronics board (left bottom), the on-board computer covered with its cold plate (top), LED array and the shaking mechanism supporting the experiment cells (right bottom) can be seen.

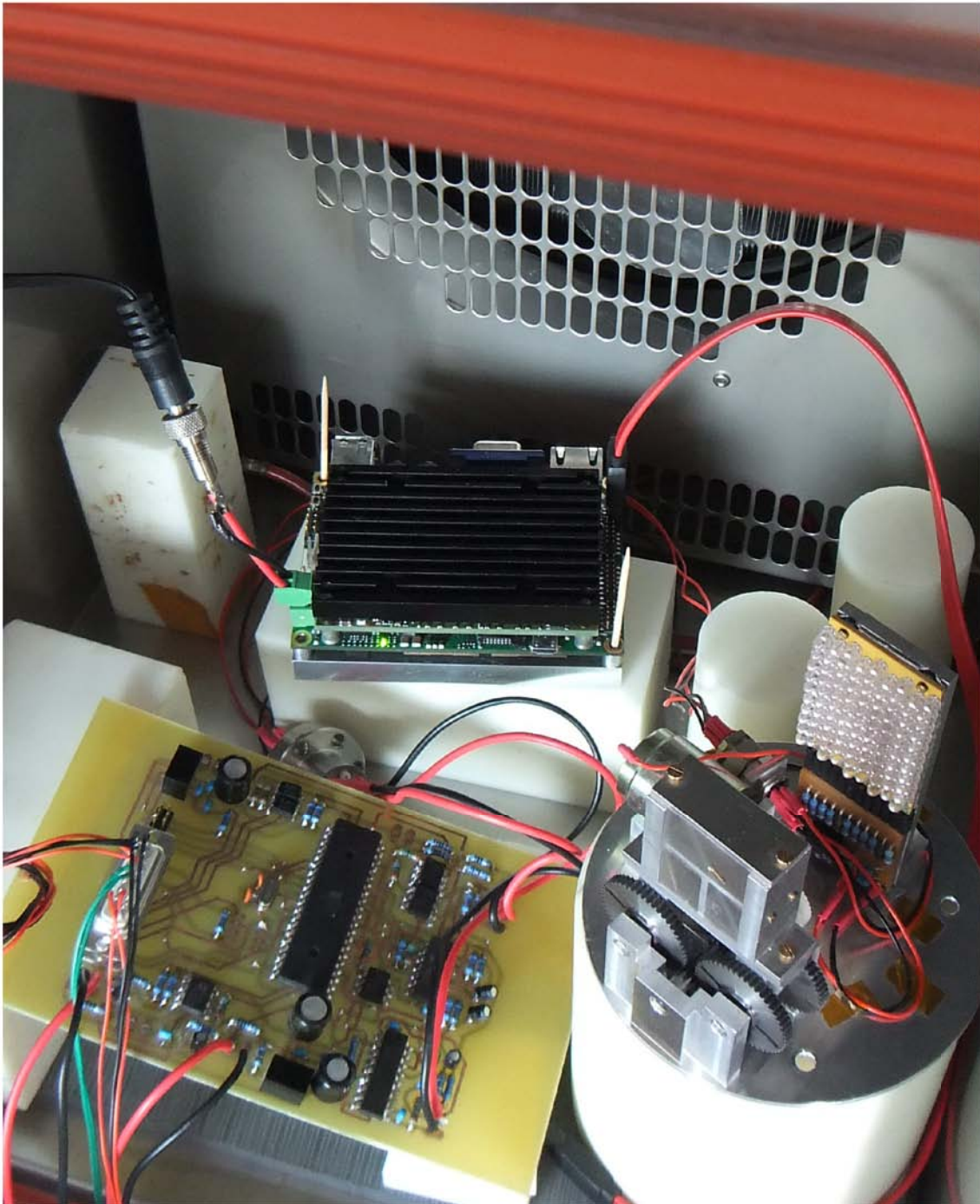


Figure C.3: Second thermal test: frost on the on-board computer and electronics board power cables.



C.3 Camera settings and optics tests

Title: Optics adjustment test

Date: 07.12.2011

Participants: René Weidling, Stefan Kothe

Components tested: Particle container, camera, objective, LED array.

Pre-test configuration: Particle containers and LED array are mounted inside the vacuum chamber.
No optical ring before objective.
One screw inside each particle container.
Camera exposure time is 25 μ s.

Procedure:

Time	Action	Comments
10:00	Camera position is adjusted for a focus on the screws inside the particle containers	Backlit by the LED array
10:15	Diffusion paper and plate are adjusted to the LED array and the particle container	
10:30	The objective aperture is fixed to 5-6	Gray scale maxima at 20, 148 and 177

Conclusion:

The exact required position of the camera could be determined.

Title: Optics vacuum test**Date:** 08.12.2011**Participants:** René Weidling, Stefan Kothe**Components tested:** Particle container, camera, objective, LED array.**Pre-test configuration:** Particle containers and LED array are mounted inside the vacuum chamber.

No optical ring before objective.

One screw inside each particle container.

Camera exposure time is 25 μ s.

Camera is positioned as per optical test of 07.12.2011.

Procedure:

Time	Action	Comments
09:45	Gray scale measurements at ambient pressure	Peak black: 18 Peak white: 179 Max white: 210
10:00	Evacuation of the vacuum chamber	
13.00	Gray scale measurements under vacuum	Peak black: 20 Peak white: 195 Max white: 220
13:45	Vent and open chamber	LED array warm, but touch temperature

Conclusion:

The influence of vacuum on the optical settings can be neglected.

Figure C.4: Optics vacuum test setup.

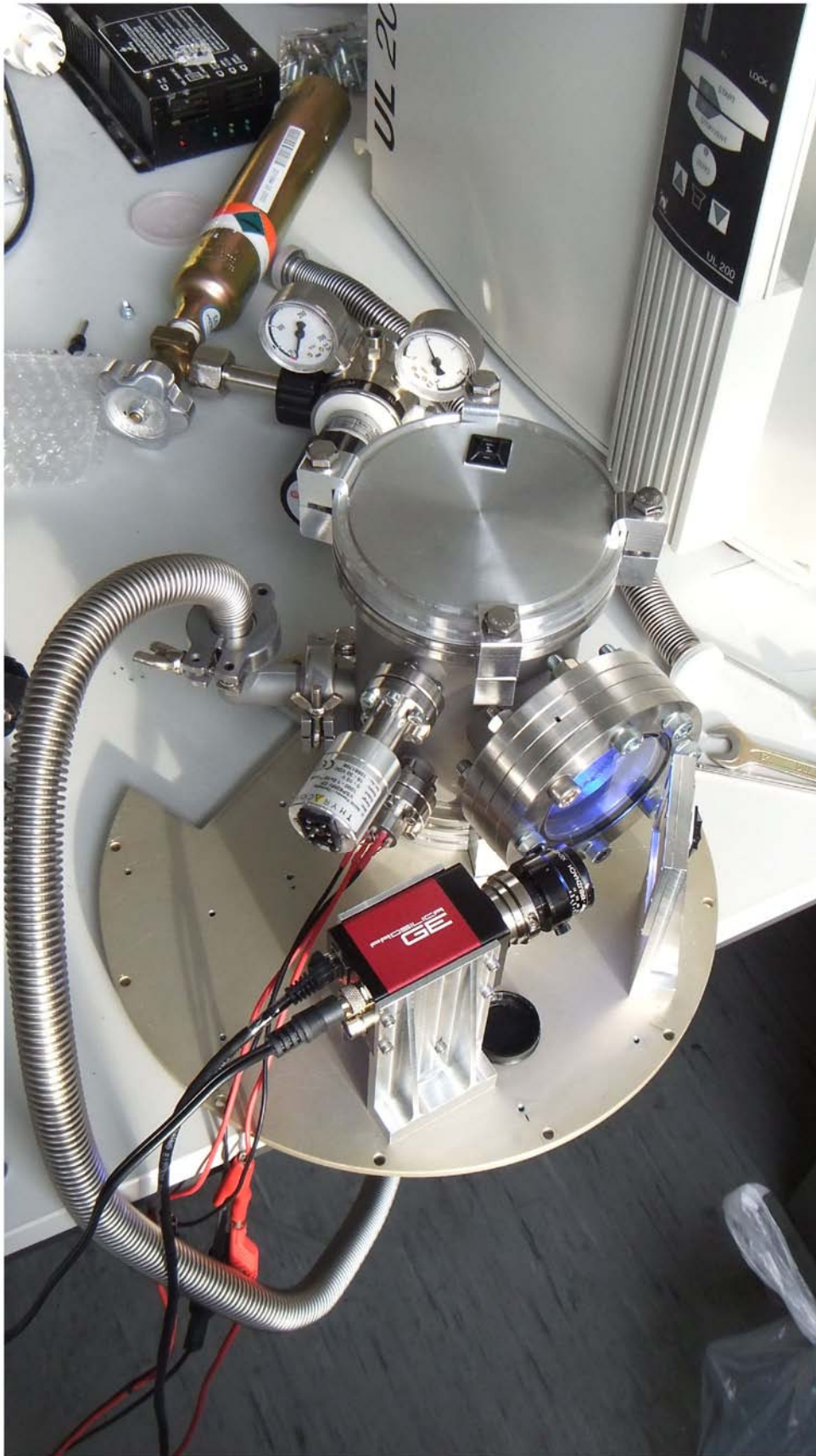
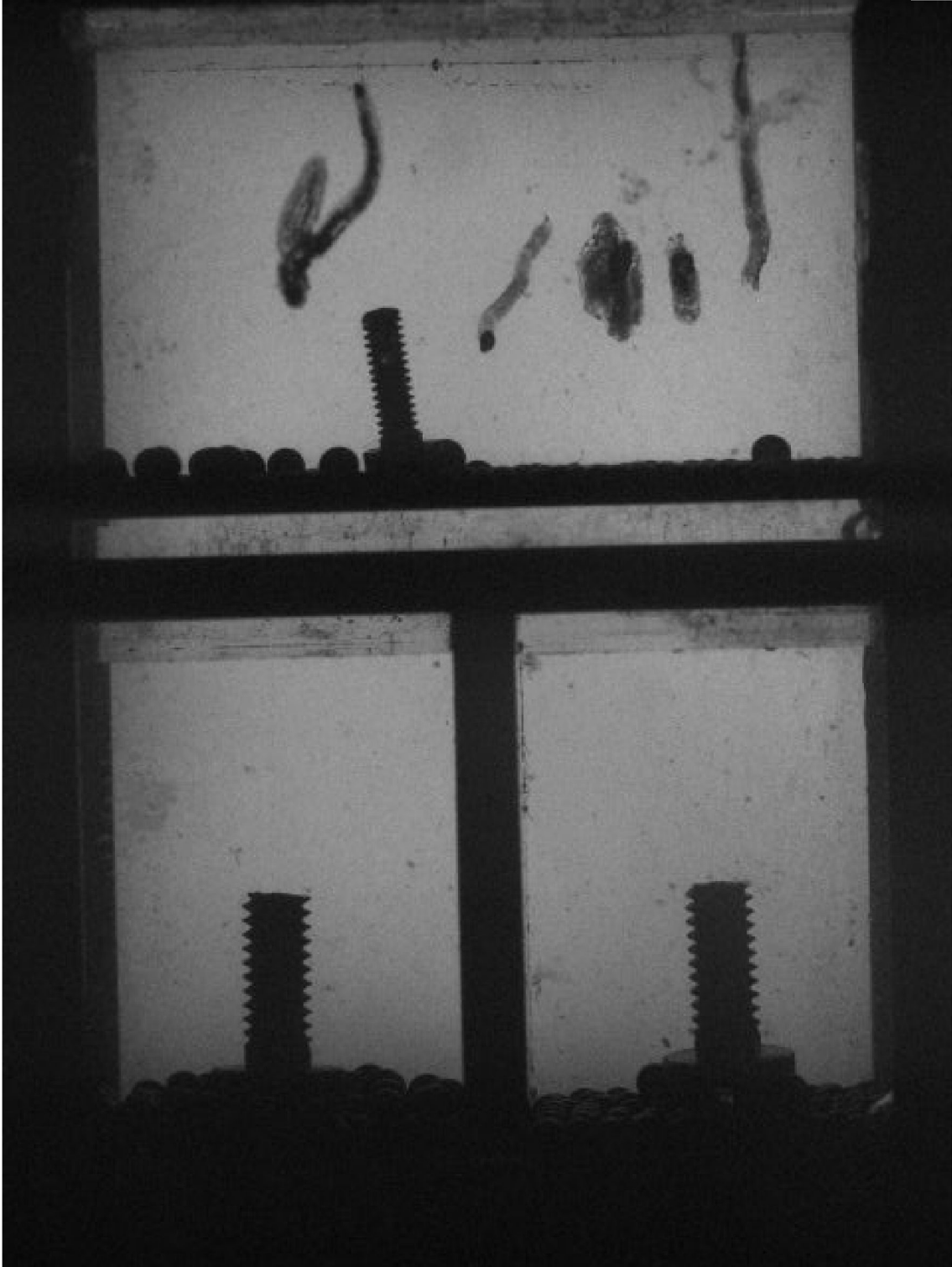


Figure C.5: Adjusted optics after the optics test. The pen marks on the cell glass are irrelevant.



C.4 Electronics test

Title: Electronics test

Date: 01.12.2011

Participants: Julie Brisset

Components tested: Electronics Board, LED array, camera, motor, flash card with adapter, SBC, pressure sensor.

Pre-test configuration: All components are connected to the electronics board.

Procedure:

Time	Action	Comments
10:00	Power on electronics board	Flash card with adapter and SBC are powered
10:05	Switch on camera Switch on motor Switch on LED array Switch on pressure sensor	All components are on Consumption: 0.75 A
10:10	Check reception of LO and SOE signals	Good signal reception
10:15	End of test	

Conclusion:

The electronics board fulfills all required functions.

C.5 Software tests

Title: Electronics Software Test

Date: 01.12.2011

Participants: Julie Brisset

Components tested: Microcontroller software with LED array, motor, camera and pressure sensor.

Pre-test configuration: All components are connected to the electronics board.

Procedure:

Time	Action	Comments
14:00	Power on PCB	The microcontroller software starts automatically at power on of the board
14:05	Lift-off signal	
14:06	SOE signal	
14:10	End of test	Nominal run of the software

Conclusion:

The microcontroller software is fit for flight.

Title: Camera control software test

Date: 11.03.2012

Participants: Julie Brisset

Components tested: SBC software with camera and flash card with adapter.

Pre-test configuration: Flash card and camera are connected to the SBC.

Procedure:

Time	Action	Comments
16:00	Power SBC and flash card	The computer automatically boots when it sees power, and runs a bash script waiting for the camera
16:10	Power camera	When the camera is powered, the bash script performs some setting definition and starts streaming for 180 s
16:13	End of stream	Nominal stream at 170 fps
16:15	Check presence and quality of stream	
16:30	End of test	

Conclusion:

The frame stream loses a few frames at a time randomly after the first 5 s of streaming. This behavior stops after 15 s after which the stream is lossless and is reproducible. It seems to be related to the warming up of the processor. The further streaming is not influenced.

Successful stream at 170 fps for 180 s.

C.6 Mechanical tests

Title: Acceleration test

Date: 15 - 19.08.2011

Participants: Julie Brisset, René Weidling, Stefan Kothe, Daniel Heißelmann

Components tested: Experiment cells, shaking mechanism, motor, LED array.

Pre-test configuration: Experiment cells, shaking mechanism, motor and LED array built in an evacuated vacuum chamber in the drop tower capsule.

Procedure:

Time	Action	Comments
15.08	Drop 1	Left bottom screw between cell frame and shaking mechanism broke Motor, shaking mechanism and LED array are functioning nominally Upper right cell glass is dirty due to coating damages
16.08	Drop 2	All components functioning nominally Big crack on the bottom left cell glass
17.08	Drop 3	All components functioning nominally
18.08	Drop 4	LED array functioning nominally In addition to the crack on the bottom left cell, a big glass chip separated from the upper left cell No cell rotation due to jamming of the shaking mechanism by a glass chip
19.08	Drop 5	All components functioning nominally New experiment cells Crack on the upper left cell glass

Conclusion:

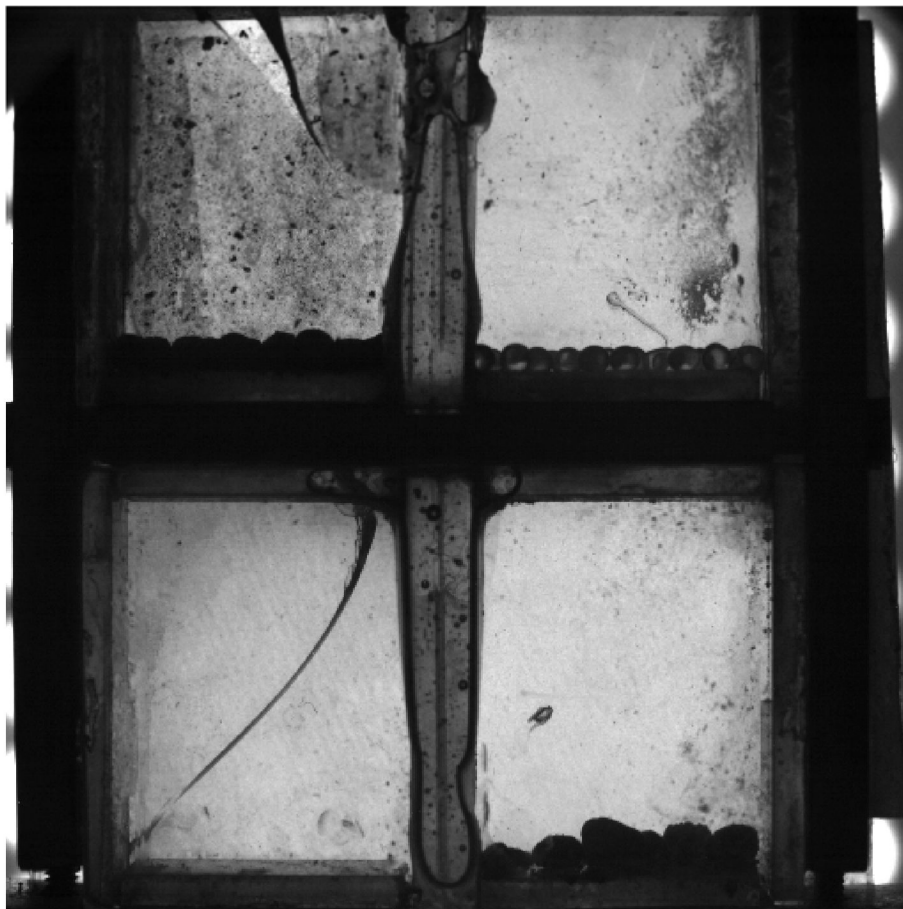
Maximum acceleration the hardware was subjected to: ~30g

LED array: nominal behavior during the test

Motor and shaking mechanism: nominal behavior during the test

Experiment cells: common glass is not adequate for the stresses and loads of the experiment preparation and run. A more robust solution needs to be implemented (technical glass). The anti-adhesive nano-coating should be handled with more care

Figure C.6: Experiment cells before drop 4. The glass of the bottom left cell cracked and a big chip separated from the upper left cell. The dirt on the upper right cell glass is due to coating damages.



Title: Vibration test**Date:** 22.11.2011**Participants:** Julie Brisset, Daniel Heißelmann, Stefan Kothe, René Weidling,**Components tested:** Entire experiment inside of the REXUS module.**Pre-test configuration:** All components off except for the on-board computer and the electronics board.**Procedure:**

Time	Action	Comments
	Run of an experiment sequence	Nominal run
	X-axis 1 st resonance search	frequency: 5 to 2000 Hz level: 0.25g sweep rate: 2 oct/min
	X-axis random vibration	frequency: 20 and 2000 Hz level: 5.97g power spectral density: 0.018 g ² /Hz duration: 60 s
	X-axis 2 nd resonance search	frequency: 5 to 2000 Hz level: 0.25g sweep rate: 2 oct/min
	Run of an experiment sequence	Nominal run
	Y-axis 1 st resonance search	frequency: 5 to 2000 Hz level: 0.25g sweep rate: 2 oct/min
	Y-axis random vibration	frequency: 20 and 2000 Hz level: 5.97g power spectral density: 0.018 g ² /Hz duration: 60 s
	Y-axis 2 nd resonance search	frequency: 5 to 2000 Hz level: 0.25g sweep rate: 2 oct/min
	Run of an experiment sequence	Nominal run
Continued on next page		

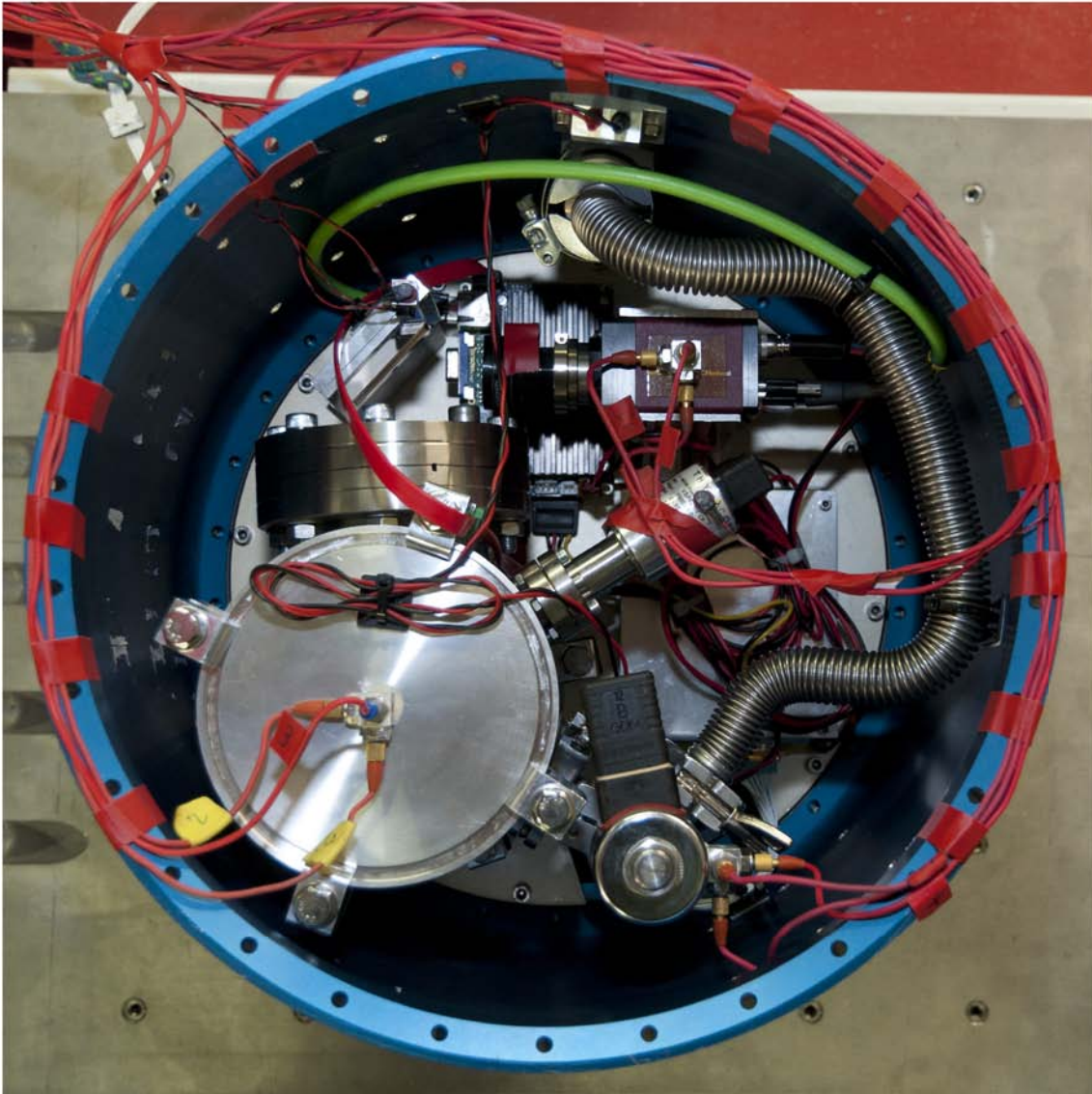
Time	Action	Comments
	Z-axis 1 st resonance search	frequency: 5 to 2000 Hz level: 0.25g sweep rate: 2 oct/min
	Z-axis random vibration	frequency: 20 and 2000 Hz level: 5.97g power spectral density: 0.018 g ² /Hz duration: 60 s
	Z-axis 2 nd resonance search	frequency: 5 to 2000 Hz level: 0.25g sweep rate: 2 oct/min

Conclusion:

The experiment hardware withstands REXUS launch vibration levels.

Detailed results can be found in the ZARM document FAB-ATR-301055.

Figure C.7: Complete SPACE experiment hardware outfitted with accelerometers and prepared for the vibration test. Image credit: D. Heißelmann.



C.7 REXUS interface tests

Title: Integration test

Date: 13 - 15.12.2011

Participants: Julie Brisset, René Weidling, Stefan Kothe, Daniel Heißelmann

Components tested: Entire experiment inside of the REXUS module.

Pre-test configuration: The experiment is switched off.

Procedure:

Time	Action	Comments
13.12	Connection to the REXUS Service Module simulator Experiment sequence run through and TM/TC check	All components functioning nominally on a functioning simulator channel Telemetry and telecommand nominal
14.12	Integrated connection to the REXUS Service Module simulator Experiment sequence run through and TM/TC check	All components functioning nominally Telemetry and telecommand nominal for the correct baud rate
15.12	Flight timeline run through in the integrated configuration	All components functioning nominally Telemetry and telecommand nominal

Conclusion:

Nominal functioning of the experiment.

Title: Bench test**Date:** 18 - 20.01.2012**Participants:** Julie Brisset, René Weidling, Daniel Heißelmann**Components tested:** Entire experiment inside of the REXUS module.**Pre-test configuration:** The experiment is switched off.**Procedure:**

Time	Action	Comments
18.01	Connection to the REXUS Service Module simulator Experiment sequence run through and TM/TC check	All components functioning nominally on a functioning simulator channel Telemetry and telecommand nominal
19.01	Connection to the REXUS Service Module Experiment sequence run through and TM/TC check	All components functioning nominally Telemetry and telecommand nominal for the correct baud rate
20.01	Flight timeline run through in the integrated configuration	All components functioning nominally The experiment picks up the SOE signal of the neighbor experiment

Conclusion:

Nominal functioning of the experiment.

A debounce was implemented into the microcontroller software to avoid triggering by other experiments' signals.

Title: REXUS campaign bench test

Date: 15.03.2012

Participants: Julie Brisset, Daniel Heißelmann, Stefan Kothe, René Weidling

Components tested: Entire experiment inside of the REXUS module.

Pre-test configuration: The experiment is switched off.

Procedure:

Time	Action	Comments
	Connection to the REXUS Service Module simulator Experiment sequence run through and TM/TC check	All components functioning nominally Telemetry and telecommand nominal
	Connection to the REXUS Service Module Experiment sequence run through and TM/TC check	All components functioning nominally Telemetry and telecommand nominal for the correct baud rate
20.01	Flight timeline run through in the integrated configuration	All components functioning nominally The experiment picks up the SOE signal of the neighbor experiment

Conclusion:

Nominal functioning of the experiment.

Title: REXUS campaign countdown simulation**Date:** 17.03.2012**Participants:** Julie Brisset, Daniel Heißelmann, Stefan Kothe, René Weidling**Components tested:** Entire experiment inside of the REXUS module.

Pre-test configuration: The experiment is switched off.
The experiment is integrated into the payload stage of the REXUS 12 rocket.
The experiment ground station is in the Esrange control center.

Procedure:

Time	Action	Comments
	Experiment power on	Telemetry and telecommand nominal
	Countdown and flight timeline run through	All components functioning nominally Telemetry and telecommand nominal

Conclusion:

Nominal functioning of the experiment.

Bibliography

- Amelin, Y., Krot, A. N., Hutcheon, I. D., & Ulyanov, A. A. 2002, *Science*, 297, 1678
- Anderson, M., Orsan, H., Koivusalo, R., Laukkanen, M., & Rigaldo, A. 2009, Reverse Engineering the REXUS Rocket, http://perso.centrale-marseille.fr/~arigaldo/visible/KTH_projects/SPACE_REXUS_Rocket.pdf
- Andrews, S. M. & Williams, J. P. 2007, *The Astrophysical Journal*, 659, 705
- Armitage, P. J. 2010, *Astrophysics of Planet Formation*
- Augereau, J. C., Lagrange, A. M., Mouillet, D., Papaloizou, J. C. B., & Grorod, P. A. 1999, *Astronomy and Astrophysics*, 348, 557
- Balbus, S. A. & Hawley, J. F. 1991, *The Astrophysical Journal*, 376, 214
- Beitz, E., Güttler, C., Blum, J., et al. 2011, *The Astrophysical Journal*, 736, 34
- Blum, J. 2006, *Advances in Physics*, 55, 881
- Blum, J., Bruns, S., Rademacher, D., et al. 2006a, *Physical Review Letters*, 97, 230601
- Blum, J., Gundlach, B., Mühle, S., & Trigo-Rodríguez, J. M. 2014, *Icarus*
- Blum, J. & Münch, M. 1993, *Icarus*, 106, 151
- Blum, J. & Schräpler, R. 2004, *Physical Review Letters*, 93, 115503
- Blum, J., Schräpler, R., Davidsson, B. J. R., & Trigo-Rodríguez, J. M. 2006b, *The Astrophysical Journal*, 652, 1768
- Blum, J. & Wurm, G. 2000, *Icarus*, 143, 138
- Blum, J. & Wurm, G. 2008, *Annual Review of Astronomy and Astrophysics*, 46, 21
- Blum, J., Wurm, G., Poppe, T., et al. 1999, *Measurement Science and Technology*, 10, 836
- Blum, J., Wurm, G., Poppe, T., Kempf, S., & Kosaka, T. 2002, *Advances in Space Research*, 29, 497

- Boley, A. C., Payne, M. J., Corder, S., et al. 2012, *The Astrophysical Journal Letters*, 750, L21
- Boss, A. P. 1998, *Annual Review of Earth and Planetary Sciences*, 26, 53
- Bouwman, J., Meeus, G., De Koter, A., et al. 2001, *Astronomy and Astrophysics*, 375, 950
- Brauer, F., Dullemond, C. P., & Henning, T. 2008a, *Astronomy and Astrophysics*, 480, 859
- Brauer, F., Henning, T., & Dullemond, C. P. 2008b, *Astronomy and Astrophysics*, 487, L1
- Cassan, A., Kubas, D., Beaulieu, J.-P., et al. 2012, *Nature*, 481, 167
- Chambers, J. E. 2004, *Earth and Planetary Science Letters*, 223, 241
- Chambers, J. E. & Wetherill, G. W. 1998, *Icarus*, 136, 304
- Chiang, E. & Youdin, A. N. 2010, *Annual Review of Earth and Planetary Sciences*, 38, 493
- Cuzzi, J. N., Hogan, R. C., & Shariff, K. 2008, *The Astrophysical Journal*, 687, 1432
- D'Alessio, P., Calvet, N., & Hartmann, L. 2001, *The Astrophysical Journal*, 553, 321
- Deckers, J. & Teiser, J. 2013, *The Astrophysical Journal*, 769, 151
- Derjaguin, B. V., Muller, V. M., & Toporov, Y. P. 1975, *Journal of Colloid and Interface Science*, 53, 314
- Desch, S. J. 2007, *The Astrophysical Journal*, 671, 878
- Dominik, C. & Nübold, H. 2002, *Icarus*, 157, 173
- Dominik, C. & Tielens, A. G. G. M. 1997, *The Astrophysical Journal*, 480, 647
- Einstein, A. 1905, *Annalen der Physik*, 322, 549
- Eurolaunch. 2010, REXUS User Manual, rX_REF_RX_user manual_v7-2_23Dec10
- Falconer, K. 2003, *Fractal Geometry: Mathematical Foundations and Applications*, John Wiley and Sons
- Güttler, C., Blum, J., Zsom, A., Ormel, C. W., & Dullemond, C. P. 2010, *Astronomy and Astrophysics*, 513, A56
- Güttler, C., Krause, M., Geretshauser, R. J., Speith, R., & Blum, J. 2009, *The Astrophysical Journal*, 701, 130
- Hayashi, C., Nakazawa, K., & Nakagawa, Y. 1985, in *Protostars and Planets II*, ed. D. C. Black & M. S. Matthews, 1100–1153

- Heim, L.-O., Blum, J., Preuss, M., & Butt, H.-J. 1999, *Physical Review Letters*, 83, 3328
- Henning, T. & Meeus, G. 2009, *Physical Processes in Circumstellar Disks around Young Stars*
- Hernández, J., Hartmann, L., Megeath, T., et al. 2007, *The Astrophysical Journal*, 662, 1067
- Hertz, H. 1896, *J. reine und angewandte Mathematik*, 92, <https://archive.org/details/cu31924012500306>
- Hewins, R. H. 1997, *Annual Review of Earth and Planetary Sciences*, 25, 61
- Howard, A. W., Johnson, J. A., Marcy, G. W., et al. 2010a, *The Astrophysical Journal*, 721, 1467
- Howard, A. W., Marcy, G. W., Bryson, S. T., et al. 2012, *The Astrophysical Journal Supplement*, 201, 15
- Howard, A. W., Marcy, G. W., Johnson, J. A., et al. 2010b, *Science*, 330, 653
- Hull, J. 2012, *Risk Management and Financial Institutions*, courier Westford
- Hunt, B. R. & Kolushin, V. Y. 1997, *Nonlinearity*, 10
- Johansen, A., Blum, J., Tanaka, H., et al. 2014, ArXiv e-prints
- Johansen, A., Oishi, J. S., Mac Low, M.-M., et al. 2007, *Nature*, 448, 1022
- Johnson, K. L., Kendall, K., & Roberts, A. D. 1971, *Proceedings of the Royal Society of London*, 324, 301
- Kendall, K., McN. Alford, N., & Birchall, J. 1987, *Nature*, 325, 794
- Kothe, S., Beitz, E., Brisset, J., et al. 2014, in preparation
- Kothe, S., Blum, J., Weidling, R., & Güttler, C. 2013, *Icarus*, 225, 75
- Kothe, S., Güttler, C., & Blum, J. 2010, *The Astrophysical Journal*, 725, 1242
- Krause, M. & Blum, J. 2004, *Physical Review Letters*, 93, 021103
- Langkowski, D., Teiser, J., & Blum, J. 2008, *The Astrophysical Journal*, 675, 764
- Li, A. & Greenberg, J. M. 1998, *Astronomy and Astrophysics*, 331, 291
- MacGregor, M. A., Wilner, D. J., Rosenfeld, K. A., et al. 2013, *The Astrophysical Journal Letters*, 762, L21
- Moreno, F., Cabrera-Lavers, A., Vaduvescu, O., Licandro, J., & Pozuelos, F. 2013, *The Astrophysical Journal Letters*, 770, L30
- Moreno, F., Pozuelos, F., Aceituno, F., et al. 2012, *The Astrophysical Journal*, 752, 136

- Morris, M. A. & Desch, S. J. 2010, *The Astrophysical Journal*, 722, 1474
- Nübold, H., Poppe, T., Rost, M., Dominik, C., & Glaßmeier, K. 2003, *Icarus*, 165, 195
- Okuzumi, S., Tanaka, H., & Sakagami, M. 2009, *The Astrophysical Journal*, 707, 1247
- Ormel, C. W. & Cuzzi, J. N. 2007, *Astronomy and Astrophysics*, 466, 413
- Ormel, C. W. & Spaans, M., T. A. G. G. M. 2007, *Astronomy and Astrophysics*, 461, 215
- Paraskov, G. B., Wurm, G., & Krauss, O. 2007, *Icarus*, 191, 779
- Paszun, D. & Dominik, C. 2006, *Icarus*, 182, 274
- Poppe, T., Blum, J., & Henning, T. 1999, *Advances in Space Research*, 23, 1197
- Poppe, T., Blum, J., & Henning, T. 2000, *The Astrophysical Journal*, 533, 454
- Poppe, T., Blum, J., & Henning, T. 2000, *The Astrophysical Journal*, 533, 472
- Sanchez, N., Alfaro, E. J., & Perez, E. 2005, *The Astrophysical Journal*, 625
- Sargent, B. A., Forrest, W., Tayrien, C., et al. 2009, *The Astrophysical Journal*, 182
- Schräpler, R. & Blum, J. 2011, *The Astrophysical Journal*, 734, 108
- Schräpler, R., Borstel, I. v., Güttler, C., & Blum, J. 2013, *European Planetary Science Congress 2013*
- Scott, E. R. D. 2007, *Annual Review of Earth and Planetary Sciences*, 35, 577
- Seizinger, A., Speith, R., & Kley, W. 2012, *Astronomy and Astrophysics*, 541, A59
- Shakura, N. I. & Sunyaev, R. A. 1973, *Astronomy and Astrophysics*, 24, 337
- Shen, Y., Draine, B. T., & Johnson, E. T. 2008, *The Astrophysical Journal*, 689, 260
- Sicilia-Aguilar, A., Hartmann, L. W., Watson, D., et al. 2007, *The Astrophysical Journal*, 659, 1637
- Skorov, Y. & Blum, J. 2012, *Icarus*, 221, 1
- Smoluchowski, M. V. 1916, *Physik. Zeit.*, 17, 557
- Teiser, J., Engelhardt, I., & Wurm, G. 2011, *The Astrophysical Journal*, 742, 5
- Testi, L., Birnstiel, T., Ricci, L., et al. 2014, *ArXiv e-prints*
- Turner, N. J., Sano, T., & Dziourkevitch, N. 2007, *The Astrophysical Journal*, 659, 729
- van Boekel, R., Min, M., Waters, L. B. F. M., et al. 2005, *Astronomy and Astrophysics*, 437, 189

- van Boekel, R., Waters, L. B. F. M., Dominik, C., et al. 2003, *Astronomy and Astrophysics*, 400, L21
- van der Marel, N., van Dishoeck, E. F., Bruderer, S., et al. 2013, *Science*, 340, 1199
- Wada, K., Tanaka, H., Suyama, T., Kimura, H., & Yamamoto, T. 2008, *The Astrophysical Journal*, 677, 1296
- Wada, K., Tanaka, H., Suyama, T., Kimura, H., & Yamamoto, T. 2009, *The Astrophysical Journal*, 702, 1490
- Wada, K., Tanaka, H., Suyama, T., Kimura, H., & Yamamoto, T. 2011, *The Astrophysical Journal*, 737, 36
- Weidenschilling, S. J. 1977a, *Mon. Not. R. Astron. Soc.*, 180, 57
- Weidenschilling, S. J. 1977b, *Astrophysics and Space Science*, 51, 153
- Weidling, R., Güttler, C., & Blum, J. 2012, *Icarus*, 218, 688
- Weidling, R., Güttler, C., Blum, J., & Brauer, F. 2009, *The Astrophysical Journal*, 696, 2036
- Wetherill, G. W. & Stewart, G. R. 1989, *Icarus*, 77, 330
- Whipple, F. L. 1972, in *From Plasma to Planet*, ed. A. Elvius, 211
- Windmark, F., Birnstiel, T., Güttler, C., et al. 2012, *Astronomy and Astrophysics*, 540
- Wittenmyer, R. A., O'Toole, S. J., Jones, H. R. A., et al. 2010, *The Astrophysical Journal*, 722, 1854
- Wurm, G., Paraskov, G., & Krauss, O. 2005, *Icarus*, 178, 253
- Yasui, C., Kobayashi, N., Tokunaga, A. T., & Saito, M. 2012, in *American Astronomical Society Meeting Abstracts*, Vol. 219, American Astronomical Society Meeting Abstracts 219, 439.06
- Zsom, A., Ormel, C. W., Dullemond, C. P., & Henning, T. 2011, *Astronomy and Astrophysics*, 534, A73
- Zsom, A., Ormel, C. W., Güttler, C., Blum, J., & Dullemond, C. P. 2010, *Astronomy and Astrophysics*, 513, A57

Publications

Brisset, J., Heißelmann, D. Kothe, S., Weidling, R., Blum, J., 2013, The Suborbital Particle Aggregation and Collision Experiment (SPACE): Studying the collision behavior of submillimeter-sized dust aggregates on the suborbital rocket flight REXUS 12, *Review of Scientific Instruments*, 84, 094501-10

Brisset, J., Heißelmann, D. Kothe, S., Weidling, R., Blum, J., 2014, Free Collisions in a Microgravity Many-Particle Experiment. IV. Sub-Millimeter-Sized Dust Aggregate Growth on a Long-Term Microgravity Experiment, *in preparation*

Conference Talks

Microgravity Experiments on the Formation of Planets, European Low-Gravity Research Association Symposium, 5 - 9 September, 2011, Antwerpen, Belgium

Suborbital Particle Aggregation and Collision Experiment (SPACE), European Low-Gravity Research Association Symposium, 5 - 9 September 2011, Antwerpen, Belgium

Suborbital Particle Aggregation and Collision Experiment (SPACE), European Planetary Science Congress (EPSC), 3 - 7 October 2011, Nantes, France

Studying Planet Formation on the REXUS Suborbital Rocket, Rocks'n'Stars Conference, 8 - 11 October 2012, Göttingen, Germany

The SPACE Experiment: Using the REXUS Suborbital Rocket to Study Planet Formation Processes, Next-Generation Suborbital Researchers Conference (NSRC), 3 - 6 June 2013, Broomfield, CO, USA

The SPACE Experiment: Studying Planet Formation Processes on a Suborbital Rocket, 21st ESA Symposium on European Rocket and Balloon Programmes and Related Research, 9 - 13 June 2013, Thun, Switzerland

Posters

Suborbital Particle Aggregation and Collision Experiment (SPACE), Dust and Grains in Low Gravity and Space Environment, 2 - 4 April 2012, ESA/ESTEC, Noordwijk, the Netherlands

SPACE on REXUS: a protoplanetary dust collision experiment on a sounding rocket, Planet Formation and Evolution, 3 - 9 September 2012, LMU, Munich, Germany

Acknowledgements

Foremost, I would like to thank my supervisor Prof. Jürgen Blum for giving me the opportunity to perform my graduate studies in his Planet Formation group at the Institute for Geophysics and Extraterrestrial Physics of the Technical University of Braunschweig. I am very grateful for the invaluable help and support throughout the project, making its success possible. Thanks for the scientific guidance and the reliable availability in the three years of my work. I also enjoyed the many opportunities to participate in different projects and international conferences.

My special thanks belong to Prof. Joshua Colwell of the University of Central Florida for accepting to review my thesis and attend my defense. I am also thankful to Prof. Karl-Heinz Glaßmeier for agreeing to chair my thesis defense.

I am very thankful to the International Max-Planck Research School (IMPRS) for Solar System Science at the University of Göttingen for funding this work. My deep gratitude goes to the late IMPRS coordinator Dieter Schmitt who first introduced me to my supervisor Jürgen Blum and helped me become a member of the IMPRS research school. I would also like to thank the IMPRS coordinator Sonja Schuh for her active support and Prof. Ulrich Christensen for his help in my Thesis Advisory Committee. It was a pleasure to enjoy the scientific and cultural diversity and vivid interaction amongst the students of the IMPRS.

I would like to thank the SPACE experiment team, Daniel Heißelmann, Stefan Kothe and René Weidling for their hard work, good advice and support throughout the project. Thanks for the fruitful discussions leading to the success of this project. In addition, I am grateful for the precious help with outreach and the thorough photographic documentation of the project.

My thanks also go to the ICAPS (Interaction in Cosmic and Atmospheric Particle Systems) project of the Deutsche Zentrum für Luft -und Raumfahrt (DLR) (grant 50WM0936) for supporting this work.

I am very grateful to the REXUS (Rocket Experiments for University Students) project of the DLR giving the SPACE experiment an opportunity to fly on the REXUS 12 sub-orbital rocket. The scientific results of this launch campaign have been essential to the completion of this thesis. I really appreciated the work of Mark Fittock, Mark Uitendaal and Martin Siegel in helping throughout the hardware design, building and testing and enjoyed the good atmosphere of the REXUS team. My thanks also belong to the REXUS operations team at the Esrange Space Center rocket range for their support during launch preparation, flight and post-flight activities. I am also grateful to Maria Roth from the DLR and Natacha Callens from the ESA education office for their support.

Acknowledgements

I would like to thank the Drop Tower workshop and operations team of the Center of Applied Space Technology and Microgravity (ZARM) in Bremen. Their help during the drop tower campaign favored the improvement of the hardware and made it possible to gather scientific data that was very valuable to this work.

I also would like to thank Dipl. Phys. Oliver Lenck from the Fraunhofer Institute for Surface Engineering and Thin Films of Braunschweig for the anti-adhesive glass coating of the particle containers. This coating proved to be very efficient and helped a lot the scientific outcome of this work.

I am much obliged to Dr. Eike Beitz, Ingo von Borstel, Shawn Frett, Dr. Bastian Gundlach, Daniel Heißelmann, Anna Krassnigg, Dr. Rainer Schröppler and René Weidling for proofreading and correcting my thesis.

I enjoyed working on my thesis at the Insitute for Geophysics and Extraterrestrial Physics in Braunschweig. The expertise, availability and helpful support of its colleagues greatly benefitted this work. In particular, my thanks go to Kai Okrafka and Paul Gerke Hofmeister for the essential support regarding the experiment electronics and data system as well as to Stefan Kothe, Bastian Gundlach and René Weidling for the fruitful discussions. Furthermore, it was a pleasure to share the office with Ingo von Borstel, who was always ready to answer my numerous questions. Additionally, I would like to thank Karl-Heinz Fornaçon for the opportunity to perform hardware temperature tests in the IGEP temperature chamber. I am also very grateful to the colleagues of the IGEP workshops Kathrin Gebauer, Bernd Stoll and Ernst Jelting for their crucial work and advice throughout this project.

Finally, I am thankful to the most important people in my life: my parents Margarete and Michel Brisset, my brother Grégory Brisset, my grandmother Margarete Scheidl and the Scheidl family, as well as my aunt Huguette Guillopé. Their support was essential to the completion of this work.

My thanks also go to my friends Renata Parente, Janine Thrams, Julia Lüdenbach, Raphael Bann and Nicolas Rapin for their support.

Curriculum Vitae

Personal data	<p>Julie Brisset 15.08.1981 Grünstraße 17, 38102 Braunschweig, Germany julie.brisset_04@laposte.net</p>
Education	<p>Since 02/2011 Technical University Braunschweig, Germany Graduate Studies: Astrophysics</p> <ul style="list-style-type: none"> • Subject: A Microgravity Sounding-Rocket Experiment on Proto-planetary Dust Aggregation • October-November 2012: Participation in the 99th and 101st Parabolic Flight Campaigns, Bordeaux, France • 08/ 2012-01/2013: Participation in the MEDEA Flight Campaign on Armadillo² STIG-B 2 Rocket, Spaceport America, USA • 03/2012: SPACE Flight Campaign on the REXUS 12 Rocket, Kiruna, Sweden • 08/2011: SPACE/MEDEA-III Drop Tower Campaign at the ZARM Drop Tower, Bremen, Germany <hr/> <p>10/2003-02/2005 Technical University Munich, Germany Double degree program</p> <ul style="list-style-type: none"> • Second year: Aeronautics and Space Engineering <hr/> <p>07-08/2004 International Space University Adelaide, Australia Summer Session program</p> <hr/> <p>09/2001-09/2003 ENSAE Toulouse, France Undergraduate Studies: Mechanical Engineering (Ecole Nationale Supérieure de l'Aéronautique et de l'Espace - SupAero)</p> <ul style="list-style-type: none"> • Second year: Space engineering • First year: Aeronautics and propulsion <hr/> <p>09/1999-08/2001 Lycée Louis-le-Grand Paris, France Classes préparatoires</p>

	<p>(Two years post-school preparatory training for competitive entry examinations for the French "grandes ecoles" including Mathematics, Physics, Engineering Science)</p> <ul style="list-style-type: none"> • Maths Sup :MPSI • Maths Spé :PSI* <hr/> <p>09/1997-08/1999 Lycée M.Daniélou Rueil Malmaison, France</p> <p>Lycée</p> <ul style="list-style-type: none"> • 1999 : Baccalauréat Général Série S mention TB • 1998-1999 : general scientific education
<p>Work experience</p>	<hr/> <p>01/2006-01/2011 Vega GmbH Cologne, Germany</p> <p>Senior Operations Engineer</p> <ul style="list-style-type: none"> • Operation of International Space Station payloads at the Microgravity User Support Centre, Deutsches Zentrum für Luft- und Raumfahrt • Collaboration with ESA and NASA ISS payload teams • Operations training responsible and participation into ISS crew training • Crew and ground procedures <hr/> <p>03/2005-10/2005 Galileo Industries Spa Rom, Italy</p> <p>Diploma Thesis</p> <ul style="list-style-type: none"> • Dissemination strategy of an external service (ERIS) of the Galileo System • Systems Engineering with Matlab and STK <hr/> <p>12/2004-02/2005 MTU Munich, Germany</p> <p>Student Help</p> <ul style="list-style-type: none"> • Testing of a new propulsion software